Gold Nanoparticle Chemiresistor Arrays for Micro-Gas Chromatography Applications

by

Elizabeth Laura Covington

A dissertation submitted in partial fulfillment
of the requirements for the degree of
Doctor of Philosophy
(Physics)
in The University of Michigan
2012

Doctoral Committee:

Associate Professor Çagliyan Kurdak, Chair
Professor Roy Clarke
Professor Luming Duan
Professor Bradford G. Orr
Professor Edward T. Zellers

© Elizabeth Laura Covington

2012

For Robert and Elliott

Acknowledgements

The work presented in this thesis would not have been possible without the unwavering support of my adviser, Çagliyan Kurdak. I can never thank you enough for your advice and encouragement over the last few years. I have learned so much from you about physics and countless other things. Thanks for reminding me to always try to maximize happiness and see the light at the end of the tunnel. You are an amazing adviser, and I am so grateful that I had the opportunity to work with you.

I would also like to thank Roy Clarke, Luming Duan, Brad Orr and Ted Zellers for serving on my committee. I would especially like to thank Ted for being a great leader of our collaborative research project that spanned two universities and multiple research groups. While I won't miss writing monthly reports, I will always appreciate the hard work you put into keeping all of us on track and focused. Thanks for always taking time to review my slides, posters and papers with great detail and provide such valuable feedback.

Thanks also the other members of the Kurdak group: Hailing, Steven, Richard and Yun. I would like to thank Hailing Cheng for training me in the clean room and on the e-beam. I'd also like to thank Rebekah Bartlett for continuing my research while I was on maternity leave and who contributed greatly to the nanoparticle stability study. Thanks also to the members of the Zellers group with whom I have worked closely with these past few years. Special thanks to Forest Bohrer and Lindsay Amos for their willingness to provide me a seemingly endless supply of nanoparticles for my research. Thanks also to our MSU collaborators, for their hard work and willingness to travel here for our project.

I would also like to thank the staff of The Lurie Nanofabrication Facility (LNF) and the Electron Microbeam Analysis Laboratory (EMAL). My research would not have been possible without these two facilities, and I am grateful for the hard working staff that keeps them in working order. I would also like to thank the other user of the e-beam lithography system, Wayne Fung, who was always willing to help me trouble shoot a problem in both the cleanroom and EMAL.

I would like to give special thanks to my mother, Dr. Veronica Covington, who moved here from Texas to take care of her grandchild so that I could complete my dissertation. I know that living in a one-bedroom apartment with two other adults, a baby, and a very noisy pug would scare most anyone, and I can never repay you for all the help you have given me. I would also like to thank my father, Dr. Billy Covington, who received his PhD in physics 34 years ago. Thank you for always encouraging me and reminding me that all of the hard work would pay off. It always helps hearing it from someone who has been there before. I would also like to thank my sisters, Jennifer and Christi, for keeping me entertained with our shared love of Twilight (ok, all vampires), Harry Potter, and countless other ridiculous things that we should be embarrassed about.

I would also like to thank my son, Elliott, who is currently eight months old. Thanks for giving me the motivation to graduate and make you proud. Thanks also for giving me an excuse to take breaks from writing. When I was feeling overwhelmed, seeing your smile always made me feel better. I hope that one day you will be able to read this and understand it. I'm keeping my fingers crossed for a third generation physicist!

And last, but not least, I would like to thank my husband, Dr. Robert Nidetz, who managed to successfully defend his PhD a week before our son was born. It's funny to think about how a couple of years ago, I was annoyed that I had to share my cleanroom box with this Rob Nidetz person. Now I know that I lucked out the day that the LNF assigned us as cleanroom box partners. Even though you were struggling to finish your own PhD, thanks for always making time for me. I could have never finished without your love, support, and mad e-beam and clean room skills. I'll never forget our late nights in the cleanroom and EMAL which made working late bearable. And who knows, maybe we'll be cleanroom box partners again one day. I love you more than VV secretly loves Hotel (in this comic I drew).

Table of Contents

Dedication ii
Acknowledgements iii
List of Figures ix
List of Tables xvi
List of Appendices xvii
Abstract xviii
Chapter 1 Introduction 1
1.1 Motivation 1
1.2 Monolayer Protected Nanoparticles 4
1.2.1 MPN Synthesis 5
1.3 Gas Chromatography 7
1.3.1 Micro-scale Gas Chromatography 7
1.4 Chemiresistor Fabrication 9
1.4.1 Electron Beam Lithography 9
1.4.2 MPN Film Coating 11
1.5 Transport in Nanoparticle Films 14
1.5.1 Modeling of Capacitance and Resistance in an MPN Film 15
1.5.2 Tunneling 18
1.5.3 Distinguishing Electron and Hole Tunneling 20
1.5.4 Coulomb Blockade 21
1.5.5 Charging Energy 24

1.5.6 Transport Regimes through Metal Islands 25
1.5.7 Engineering Transport Properties 26
1.6 Improving Limit of Detection 28
1.6.1 1/*f* noise 29
1.6.2 Optimizing Sensor Size 30
1.7 Chemiresistor Stability 31
1.8 References 32
Chapter 2 Electrical Noise in Gold Thiolate Nanoparticle Chemical Sensors 37
2.1 Introduction 37
2.2 Noise Power Spectral Density Function 39
2.2.1 Thermal Noise 40
2.2.2 1/*f* -type noise 40
2.3 Measuring Noise Amplitude 41
2.3.2 Scaling in Noise Amplitude 43
2.4 Fabrication of Chemiresistors 44
2.4.2 Micro-deposition of Nanoparticle Solutions 45
2.4.3 Monolayer Films Deposition 47
2.5 Noise Amplitude Versus Film Morphology 48
2.5.1 I-V Characteristics of Monolayer Films 48
2.5.2 Noise Amplitude Versus Chemiresistor Resistance 49
2.6 Nanoparticle Film Contamination 51
2.7 Electron Beam Induced Crosslinking for Noise Reduction 53
2.8 Conclusions 54
2.9 References 57
Chapter 3 Electron Beam Induced Crosslinking of Gold Thiolate Nanoparticles 59
3.1 Introduction 59
3.2 In-Situ measurements of Crosslinked films 60
3.2.1 Experimental Methods 60
3.2.2 Changes in Resistance 60
3.3 Effect of Crosslinking on Activation Energy 62

3.4 Electron-beam Induced Crosslinking for Array Patterning 65
3.4.1 Chemiresistor Fabrication 66
3.4.2 Film Deposition 67
3.4.3 Mono-MPN array Patterning 68
3.4.4 Multi-MPN Array 70
3.5 Vapor Testing of Crosslinked Films 72
3.6 Conclusions 76
3.7 References 77
Chapter 4 Stability of Gold Nanoparticle Films 78
4.1 Introduction 78
4.2 Experimental Methods 79
4.2.1 Sensor Fabrication 79
4.2.2 Vapor Testing System 80
4.3 Low Temperature Measurements 80
4.3.1 Change Activation Energy 81
4.3.2 Low temperature IV measurements 82
4.4 Baseline Resistance Drift 85
4.4.2 Decline in Drift Rate 87
4.4.3 Stability at Elevated Temperatures 88
4.5 Electron Beam Induced Crosslinking 94
4.5.1 Drift in Baseline Resistance 94
4.5.2 Changes in Vapor Sensitivity 97
4.6 Film Contamination 98
4.7 Conclusions 100
4.8 References 103
Chapter 5 Thermoelectricity in Arrays of Thiolate Coated Au Nanoparticles 104
5.1 Introduction 104
5.2 Thermoelectricity 104
5.3 Thermopower Measurements of MPN Films 108
5.3.1 Fabrication 108

5.3.2 Noise Thermometry ... 109
5.3.3 Thermoelectric Voltage ... 113
5.4 Conclusions ... 116
5.5 References ... 118
Chapter 6 Sensor System Integration ... 119
6.1 Introduction ... 119
6.2 Integrated Sensor System ... 120
6.3 Microfluidic Packaging ... 128
6.4 Conclusions ... 131
6.5 References ... 133
Chapter 7 Future Work for Sensor Optimization ... 134
7.1 Introduction ... 134
7.2 Optimizing Sensor Size ... 136
7.2.2 Fabrication of a Test Sensor Array ... 140
7.3 Conclusions ... 142
7.4 References ... 144
Appendix A.Electron Beam Lithography Sample Preparation ... 145
Appendix B Photolithography Sample Preparation for Chemiresistor Contact Pads ... 147
Appendix C Process for Etching Glass Lids ... 149
Appendix D Process for Etching Capillary Inlet/Outlet Grooves ... 152

List of Figures

Figure 1.1 Schematic of a chemiresistor comprised of interdigitated electrodes (in gold) covered with an MPN film (in gray). The resistance, *R*, is monitored over time, *t*, for the presence of a vapor. The response is reversible, and the chemiresistor's resistance will return to its previous value after the compound has left the film. 2

Figure 1.2 (a) A schematic of MPNs between two electrodes. (b) In the presence of an analyte (red shape), the spacing between the nanoparticles increases causing an increase in resistance...2

Figure 1.3 Graphic representation of a monolayer protected gold nanoparticle. The nanoparticle core consists of a cluster of gold (Au) atoms surrounded by a monolayer of ligand (R) bound to the surface via a sulfur bond (S). Commonly used ligands are 1-octanethiol (C8), 4-mercaptodiphenylacetylene (DPA), and 1-mercapto-6-phenoxyhexane (OPH). Reprinted from Rowe *et al.*[31]. 4

Figure 1.4 In-phase current through films of C12, normalized to the in-phase current value at 1 Hz ac frequency, as a function of the frequency of the applied voltage. In-phase current measurements were collected over a 1-kHz range where the parasitic effects of the out-of-phase current are negligible. Filled triangles: C12 prepared by the Brust method. Open circles: C12-Au prepared by the single-phase method. Reprinted from Rowe *et al.*[31]...6

Figure 1.5 TEM image of C8 nanoparticles synthesized using a single phase synthesis method and a histogram of their diameters. Reprinted from Rowe *et al.* [31]. 7

Figure 1.6 Basic schematic for a micro-gas chromatography system................................8

Figure 1.7 SEM image of an IDE with electrodes with 100 nm width and spacing and 10 μm in length. 10

Figure 1.8 An eight sensor array coated with four different MPN films. The coffee stain pattern, where the majority of MPNs settle on the outer edge of the film is clearly seen. 13

Figure 1.9 A 2×2 array has been patterned with an OPH MPN film via electron beam induced crosslinking. This technique has the resolution of a SEM; hence the spacing between the films (4 μm) can be easily seen. 14

Figure 1.10 Schematic for the potential, V, of interdigitated electrodes separated by distance t with covered with a nanoparticle of thickness d and dielectric constant κ_1. The region above is infinite with dielectric constant κ_2. 15

Figure 1.11 Electric field and potential lines for interdigitated electrodes (gold bars) with spacing t and a film thickness d (indicated by shaded region) with an arbitrary dielectric constant (κ=5) to represent the MPN film. 17

Figure 1.12 A particle with energy E encounters a potential barrier, V, of width a. Classically, the particle will rebound at $x = 0$, but quantum mechanics has proven that the particle has a probability of tunneling through the barrier. 19

Figure 1.13 Energy diagram of two gold electrodes separated by an alkanethiol molecule. Tunneling can occur through either the LUMO or the HOMO. 21

Figure 1.14 I-V characteristics of a 4 nm diameter C8 coated chemiresistor at different temperatures. Non-linear I-V curves are visible at lower temperatures indicative of Coulomb blockade. Reprinted from Kurdak *et al.*[2]. 23

Figure 1.15 The three transport regimes, at T=0, for tunneling through metallic islands. (a) No current flows when the bias voltage, V_b, is below the threshold voltage, V_{th}. (b) In between V_{th} and V_{off}, where all channels are open, current flows nonuniformly through select channels. (c) At large V_b, all channels are open and current flows uniformly. 25

Figure 1.16 Coulomb blockade is more pronounced for the smaller (2 nm) diameter C8 MPN film. Reprinted from Kurdak *et al.*[2]. 27

Figure 1.17 (a) I-V characteristics of C8, C12, and C18 MPNs at 9 K. MPNs with longer ligand are found to have an increase in resistance. (b) I-V characteristics of C12, NDPA, and DNDPA MPNs at 1.5 K. The tunnel coupling of MPNs can be changes by using ligands with different LUMO energies. Reprinted from Kurdak *et al* [2]. 28

Figure 1.18 The power spectral density function, S_V, of a typical sensor coated with C8 nanoparticles exhibits $1/f$-type noise...29

Figure 2.1 Experimental set-up for measuring noise of a chemiresistor using a variable bias voltage, current sensitive amplifier and spectrum analyzer. 42

Figure 2.2 The noise power spectral density function, $S_V(f)$, for a chemiresistor at bias voltages of 0.1 and 0.3 V. As shown in the inset, $S_V(f)$ scales quadratically with voltage.42

Figure 2.3 The noise amplitude, or prefactor, of a chemiresistor scales inversely with sensor area. Reprinted from Kruppa *et al.*[3]. 44

Figure 2.4 A 50x60 μm^2 device comprised of interdigitated electrodes with 0.3 µm width and spacing...45

Figure 2.5 Progression of a drop of toluene as it is ejected from the micro-dispensing system. Each division is 100 µm, therefore the droplet is approximately 75 µm in diameter..46

Figure 2.6 Nanoparticles dry in a "coffee ring" pattern where the majority of nanoparticles settle in a thick outer ring leaving a thinner interior film. The scale bar indicated 75 µm..47

Figure 2.7 Chemiresistors coated with a monolayer film exhibit Coulomb blockade behavior at room temperature. 49

Figure 2.8 Chemiresistors with monolayer films of octanethiol (C8) MPNs have the highest noise prefactor while films deposited with the micro-dispensing system can have 5 times lower noise depending on film thickness. The scatter in the data may be caused by differences in nanoparticles solutions. 51

Figure 2.9 Noise amplitude versus resistance for chemiresistors with either 0% or 20% naphthalene added to the C8 nanoparticle solution. The trend follows that of Figure 2.8 where chemiresistors of high resistance have larger noise amplitudes, but the large scatter in the data cannot be attributed to naphthalene contamination. 52

Figure 2.10 Change in noise prefactor as a function of the electron beam dosage of cross-linked sensors. 54

Figure 3.1 Decrease in resistance of a C8 coated sensor after repeated SEM exposure...62

Figure 3.2 A C8 coated chemiresistor's resistance decreases with increasing electron beam exposure leading to a nearly two order of magnitude decrease. 63

Figure 3.3 The activation energy before and after an electron beam exposure of 11 mC/cm^2. The large exposure dose leads to a decrease in activation energy consistent with a reduction in the average distance between nanoparticles. 64

Figure 3.4 SEM image of an array with four chemiresistors with 20 pairs of interdigitated electrodes with 100 nm width and spacing. Adjacent chemiresistors are spaced by 4 µm. The scale bar indicates 5 µm...66

Figure 3.5 Optical image of a four sensor array with a micro-dispensed nanoparticle film covering all IDEs. The thickest portion of the film, the coffee ring, is placed directly over the IDEs to ensure the thickest possible film coating. The scale bar indicated 50 µm......68

Figure 3.6 (a) Optical image of an array covered with an OPH nanoparticle film. Scale bar indicated 50 µm. (b) After electron beam exposure, the array was rinsed with toluene leaving only the active areas of the array patterned with the OPH nanoparticle film. 69

Figure 3.7 (left) Optical image of a crosslinked OPH nanoparticle array. (right) AFM image of the same array. The average film thickness if 244 nm. Scale bars in both images indicate 10 µm. 69

Figure 3.8 Optical images of a chemiresistor array at different stages in the crosslink patterning process. (a) The top left IDEs are exposed to 600 $\mu C/cm^2$ of electron-beam radiation. The array was rinsed with toluene leaving the irradiated sensor coated with a patterned C8 film. (b) The top right IDEs were patterned with an OPH film. (c) The bottom left IDEs were patterned with an HFA film. (d) The bottom right IDEs were patterned with a DPA film. Since the alignment marks at the periphery of the image are also repeatedly exposed during beam alignment, they are also coated. The scale bar indicates 10 μm. 71

Figure 3.9 The normalized change in resistance of the HFA coated chemiresistor while being exposed to 3100 ppm of toluene. 72

Figure 3.10 Calibration curves for *n*-propanol....73

Figure 3.11 Sensitivities ($R_{ppm}/mg \cdot m^{-3}$) of the array sensors for the four test vapors ($R_{ppm} = \Delta R/R_b \times 10^6$). 74

Figure 3.12 LDA plot from multiple-MPN array of data generated by Monte Carlo simulations (500 iterations per vapor) with the following relative errors superimposed on responses from experimental sensitivities: 7.4%, 5.8%, 5.8%, and 4.4% for C8, DPA, OPH, and HFA, respectively. The vapors are *n*-octane (OCT), *n*-propanol (OPH), toluene (TOL) and 2-butanone (MEK). 75

Figure 4.1 (top) Temperature dependent IV measurements taken on day three after coating the interdigitated electrodes. The insert shows the corresponding Arrhenius plot where the activation energy was found to be 20.8 meV. (bottom) Temperature dependent IV measurements taken on day 93. The insert shows the corresponding Arrhenius plot where the activation energy was found to be 18.8 meV. 83

Figure 4.2 Arrhenius plots for the sensor at day 3 and 93. While the resistance changed from 0.8 MΩ to 18.4 kΩ, the activation energy only changed from 20.8 meV to 18.8 meV indicating that change in resistance is not due to decay in the gold nanoparticle core......85

Figure 4.3 Change in resistance of a C8 coated sensor array after to exposures to 200 ppm of toluene vapor for 300 seconds. The exposure is repeated to determine reproducibility. 86

Figure 4.4 On standard C8 array, the change in resistance increases when the array is heated to 90°C (highlighted area). The drift rate slows once the array is cooled to room temperature. 89

Figure 4.5 Sensitivity versus resistance for a C8 array before and after heating to 50°C, 70°C, and 90°C for a cumulative 145 hours. Vapor tests were performed after the array had been cooled to room temperature. 90

Figure 4.6 The sensitivity values (($\Delta R/R_b)/C_{ppm}$) of C8 coated array to toluene vapor before and after heating to 70°C. 91

Figure 4.7 Sensitivity versus baseline resistance for a C8 coated array before after being heated to up to 80°C or 441 hours. Note that a large change in baseline resistance does not lead to a decrease in sensitivity..93

Figure 4.8 The daily percent change in resistance of an array coated with C8, OPH, and DPA films where half of the sensors are crosslinked. The sensors were monitored at 22 ºC, 50 ºC, 75 ºC, 90 ºC, 105 ºC, and 125 ºC. Crosslinked films generally experience less drift especially at elevated temperatures..96

Figure 4.9 Higher electron beam exposure leads to a decreased sensitivity to toluene vapor. This trend continues after heating the arrays to 50°C, 70°C, and 90°C. 98

Figure 4.10 The sensitivity ($(\Delta R/R_b)/C_{ppm}$) to toluene vapor decreases and the percentage of naphthalene in the C8 nanoparticle film increases....................................99

Figure 5.1 Plot of the transmission, $\mathcal{T}(E)$ as a function of energy. The slope of $\mathcal{T}(E)$ depends on the location relative to the HOMO or LUMO. The location of the Fermi energy, E_F, is closer to the HOMO, like E_{F1}, then holes tunnel through the HOMO. If the E_F is closer to the LUMO, like E_{F2}, then electrons tunneling through the LUMO.........107

Figure 5.2 (a) Optical image of two 400 mm long parallel gold wires with width and spacing of 500 nm. (b) A SEM image of the wires. 109

Figure 5.3 Schematic of the experimental set-up for noise thermometry measurements. A battery is used to apply a voltage across the outer contact pads. The inner contact pads are used to measure the noise power spectral density function with a spectrum analyzer. The resistor was 3 kΩ...111

Figure 5.4 $S_V(f)$ at 0, 3.5 and 4.5 mA. The slight frequency dependence of $S_V(f)$ is due to amplifier noise as is it present even at 0 mA. 111

Figure 5.5 Noise power spectral density function, $S_V(f)$, versus current squared for a 1 μm thick, 400 μm long gold wire. From the slope of this graph, the temperature can be calculated from a given current. At 4.5 mA, the increase in temperature is 40 K...........112

Figure 5.6 (a) Thermal probe scan of the approximately 2 μm area heated by applying a current across a 1 μm wide gold electrode. The white area is the heated region. (b) (inset) The change in resistance of the thermal probe as a function of distance from the center of the electrode (at 0 μm). From this, we can determine ΔT across the nanoparticle film. The second wire, located at 1.5 μm is outside of the heated region. The peak heat and current scales quadratically. 113

Figure 5.7 Schematic of the experimental set-up used to measure the induced voltage across a nanoparticle film. The dark bars represent the gold electrodes with four contact pads per side while the grey region represents the area coated with a nanoparticle film (not drawn to scale). The far left wire was excited with an AC current to create a temperature difference, and the induced voltage was measured between the wires........114

Figure 5.8 The second harmonic of the voltage, $V_{2\omega}$, as a function of applied current for three different nanoparticle films. All films were electron beam crosslinked. Positive $V_{2\omega}$ indicates electron tunneling in the C8 film and 100 mC/cm^2 crosslinked DPA film. The 40 mC/cm^2 has a negative sign indicating hole tunneling. 115

Figure 6.1 The 2.2×2.2 mm^2 read-out chip with an eight sensor array fabricated on the surface of the chip. The large circles are contact pads that connect the sensors to the embedded electronics. 121

Figure 6.2 (a) IDEs fabricated on read-out chip in an area with an uneven surface due to embedded metal lines. (b) SEM image of the discontinuities of the IDEs due to the metal lines under the chip's surface. 121

Figure 6.3 The 2.2×2.2 mm^2 read-out chip, designed by our collaborators at MSU, with a metal region plateau the sensor region (surrounded by red square). The chemiresistor (CR) readout electronics are located at the bottom right region of the chip to limit the embedded electronics exposure to high energy electrons during electron beam lithography. 123

Figure 6.4 Interdigitated electrodes with area of 75×75 μm^2 fabricated on the surface of the readout chip. Scale bar indicates 75 μm. 124

Figure 6.5 (a) Eight sensor array on the readout with ECcontact pads added by photolithography. Scale bar indicated 200 μm. (b) 4 sensor on another array with contact pads added by focused ion beam platinum deposition. Scale bar indicated 75 μm. 125

Figure 6.6 Sensor array coated with micro-dispensing system. Top row of sensor are coated with C8 while bottom row is coated with OPH. The scale bar indicates 75 μm. .126

Figure 6.7 Response curves of a C8 coated sensor to toluene at 380, 490, and 682 ppm after baseline resistance cancellation. 127

Figure 6.8 Concentrations curves of a C8 coated sensor to 2-butanone, nitromethane, and toluene. 127

Figure 6.9 Schematic view of total device assembly designed Dr. Wen Li's research group. 129

Figure 6.10 Assembled packaged sensor chip wirebonded to a 40-pin DIP header. The capillary tubing and glass lid are attached with a nonabsorbent epoxy. 130

Figure 6.11 Five chromatograms from a single chemiresistors on the packaged sensor chip. As shown in the inset, the components of the vapor mixture are distinguishable. .131

Figure 7.1 A schematic of a sensor array with width and length of L_1 and L_2 enclosed in a chamber of height h. The inlet capillary tube has radius r. 135

Figure 7.2 The normalized concentration, C_{sens}, for different GC columns of radius, r. As r is decreased, the need for smaller sensor arrays becomes more pronounced. This was calculated for a sensor chamber with a 600 μm width and 50 μm height........................139

Figure 7.3 Chip with glass lid with a 100 μm etched recess above the sensor array and inlet and outlet capillary tubes. The red box indicates the area of the sensor area show to the right. 141

List of Tables

Table 4.1 The resistance for sensors on a standard array B on Day 1, 4 and 20. The total percent change over the 20 days is also shown. Although their initial resistance values vary greatly, the rate of change between sensors is comparable. 87

Table 4.2 Comparison of baseline resistance and sensitivity values for a C8 array on day 1 and day 22 while at room temperature. Values are missing for sensors 2 and 4 due to a connection error. 92

List of Appendices

Appendix A Electron Beam Lithography Sample Preparation 145
Appendix B Photolithography Sample Preparation for Chemiresistor Contact Pads 147
Appendix C Process for Etching Glass Lids 149
Appendix D Process for Etching Capillary Inlet/Outlet Grooves 152

Abstract

Thiolate-monolayer-protected gold nanoparticle (MPN) chemiresistors were studied as the sensing devices for micro-gas chromatography (μGC) systems. Because transport through chemiresistors is dominated by tunneling, they are highly sensitive. In order to improve their limit of detection, their fundamental noise was studied. Chemiresistors exhibit $1/f$ type noise where noise scales inversely with frequency. Chemiresistor noise was found to scale inversely with MPN film thickness. We lowered the noise prefactor of a 50×60 μm^2 chemiresistor by coating a thick rather than monolayer MPN film. Electron beam induced crosslinking (EBIX) of the MPN film slightly reduced chemiresistor noise. A technique for patterning chemiresistor arrays with MPN films using EBIX was developed, and an array with four distinct MPNs was fabricated in an area ~600 μm^2. This is the smallest chemiresistor array reported to date. Chemiresistors were exposed to vapors and provided differential sensitivities comparable to those from larger uncrosslinked chemiresistors.

Chemiresistors were studied to assess their long term stability. Chemiresistors exhibited decreases in resistance over time that is likely caused by loss of MPN ligands. Temperature dependent current-voltage measurements verified the resistance change was not due to changes in the size of the MPN core. While resistance could change by orders of magnitude, vapor sensitivity did not show significant changes. Heating increased the

change in resistance, but chemiresistors remained responsive after being held at 80°C for a cumulative 400 hours.

It was unknown whether tunneling in the MPN film is through the highest unoccupied molecular orbital (HOMO) or lowest unoccupied molecular orbital (LUMO). A new technique was explored to distinguish tunneling through the HOMO and LUMO by measuring the induced thermoelectric voltage caused by a temperature difference across the MPN film.

For integration into a μGC system, we fabricated a chemiresistor array on the surface of a 2.2×2.2 mm^2 readout circuitry chip creating a monolithic sensor system. A model for determining the optimal sensor size for a μGC system is presented. While noise is inversely proportional to chemiresistor volume, the amount of analyte detectable is proportional to volume making smaller chemiresistors able to detect lesser amounts of analyte.

Chapter 1

Introduction

1.1 Motivation

Chemiresistors are sensors whose electrical properties (e.g. resistance) change in the presence of a chemical species. They are of great interest due to their simple design and function, as they only require the monitoring of resistance during operation. While there are many types of chemiresistors, this thesis will focus on those comprised of interdigitated electrodes covered with a thiolate monolayer-protected gold nanoparticle (MPN) film as the interfacial layer. A schematic of chemiresistor is shown in Figure 1.1. This type of chemiresistor was introduced as a colloidal "metal-insulator-metal ensemble" by Wohltjen and Snow[1]. These devices yielded parts per million (ppm) detection limits for toluene and tetrachloroethylene making them exciting prospects for the detection of other volatile organic compounds (VOCs).

MPN-coated chemiresistors are sensitive to VOCs because transport through the MPN film is dominated by tunneling[2-4]. When a vapor is absorbed into the MPN film, the distance between neighboring MPNs will increase as shown in Figure 1.2. Small changes in MPN spacing can cause a large change in resistance.

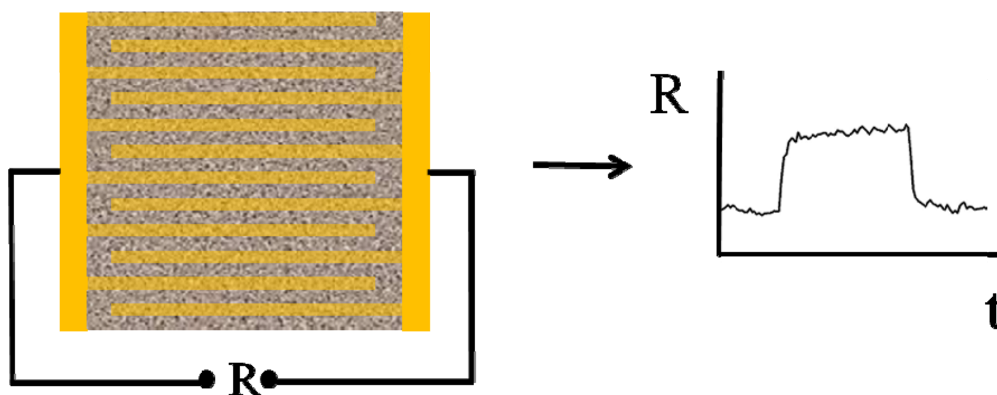

Figure 1.1 Schematic of a chemiresistor comprised of interdigitated electrodes (in gold) covered with an MPN film (in gray). The resistance, *R*, is monitored over time, *t*, for the presence of a vapor. The response is reversible, and the chemiresistor's resistance will return to its previous value after the compound has left the film.

Typically, the change in resistance, normalized by the baseline resistance, of an MPN-coated chemiresistor varies linearly with vapor concentration, and detection limits in the parts-per-billion (ppb), by volume, range are achievable[5-8].

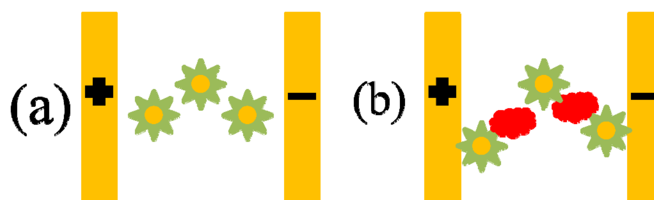

Figure 1.2 (a) A schematic of MPNs between two electrodes. (b) In the presence of an analyte (red shape), the spacing between the nanoparticles increases causing an increase in resistance.

The sorption of a vapor with a difference dielectric constant than the ligand matrix can also cause a change in the resistance of a chemiresistor[5, 6]. Chemiresistors are also frequently used because their properties can be easily tuned by employing MPNs

with different core sizes and ligand structures. Ligands can be chosen to impart partial chemical selectivity, and arrays of chemiresistors can be used for chemical identification[9-11]. Chemiresistors have been used for applications such as monitoring for environmental toxicants[12-14] and explosives[15, 16].

Chemiresistor arrays have been referred to as electronic noses. This label is applied to partially selective sensor arrays that generate a response pattern for a given VOC. Pattern recognition system statistical methods then allow for the identification and differentiation of individual VOCs[11]. It has been mistakenly assumed that increasing the number of sensors in the array will improve the identification of components of complex mixtures[10]. In actuality, the identification of complex mixtures is more dependent on the number of vapors in the mixture, their concentrations, and the diversity of the MPN coatings in the array[17, 18]. It was shown that at low vapor concentrations, arrays of three sensors provided comparable identification of a mixture of 16 organic vapors to arrays of six sensors[18].

There has been a collaborative effort at the University of Michigan to create a micro-gas chromatography (μGC) system for identifying complex vapor mixtures [14, 19, 20]. This includes the many challenges associated with miniaturizing a traditional gas chromatography (GC) system, such as the microfabrication of the components and system integration. There have been ongoing efforts at the Center for Wireless Integrated Microsystems (WIMS) to build μGC systems with applications such as the detection of breath biomarkers of respiratory disease [21] and environmental monitoring [22]. The research in this thesis has been part of a collaboration to create a portable, low power system for

the rapid detection of explosives for homeland security applications[23]. The sensing devices in this system are an array of MPN-coated chemiresistors. The challenges associated with miniaturizing these sensor arrays, as well as improving the limit of detection and long term stability, is the focus of this thesis.

1.2 Monolayer Protected Nanoparticles

An MPN is a particle with a monolayer of ligands bound to the surface. In the case of gold MPNs (hereafter simply referred to as MPNs), a thiolate ligand is attached to the gold core with a sulfur bond as shown in Figure 1.3. Because their structure can be easily adjusted, such as the core size and ligand type, MPNs are used in many applications. They are heavily used as interfacial layers in sensing devices such as thickness shear mode resonators[24, 25], biological sensors[26-28], and chemiresistors[1, 5, 6, 8, 24, 25, 29, 30].

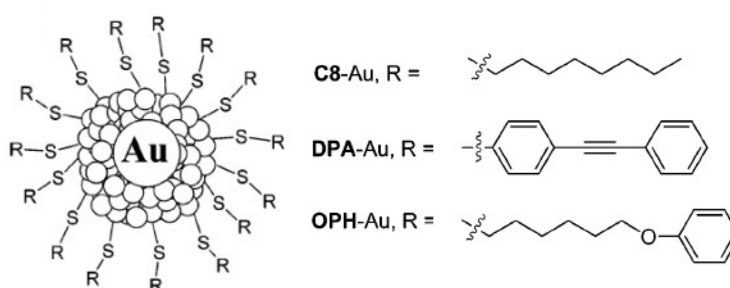

Figure 1.3 Graphic representation of a monolayer protected gold nanoparticle. The nanoparticle core consists of a cluster of gold (Au) atoms surrounded by a monolayer of ligand (R) bound to the surface via a sulfur bond (S). Commonly used ligands are 1-octanethiol (C8), 4-mercaptodiphenylacetylene (DPA), and 1-mercapto-6-phenoxyhexane (OPH). Reprinted from Rowe *et al.*[31].

1.2.1 MPN Synthesis

Gold nanoparticles are generally synthesized by the reduction of a gold salt with a stabilizing molecule in solution. One of the most commonly used methods was developed by Brust *et al.*[32]. This method uses a two-phase (water-toluene) reduction of $HAuCl_4^-$ by sodium borohydride in the presence of an alkanethiol. $HAuCl_4^-$ is dissolved in water while tetraoctylammoniumbromide is dissolved in toluene. This mixture is vigorously stirred until the $HAuCl_4^-$ is transferred to the toluene phase, then the ligand is added. Sodium borohydride is also added and vigorously stirred to reduce the gold into nanoparticles.

While this form of synthesis is very effective, the synthesized MPNs are known to be contaminated with residual tetraoctylammoniumbromide[33]. This is particularly undesirable in nanoparticle solutions that are used for vapor sensing. MPN films with ionic contaminants have been reported to suffer from decreased vapor sensitivity and humidity effects[31, 34]. As shown in Figure 1.4, chemiresistors coated with a film of dodecanethiol (C12) gold MPNs synthesized with the two-phase method have a current strongly dependent of the frequency of the applied voltage which is indicative of ionic contamination.

To overcome ionic contamination, a single-phase synthesis method can be used [31]. In this method, $HAuCl_4^-$ is dissolved in anhydrous tetrahydrofuran then the thiol is added. The reducing agent, $LiBH_4$, in anhydrous tetrahydrofuran is added. Toluene is then added under reduced pressure to remove the tetrahydrofuran. The solution is diluted again with toluene and washed with water. After the removal of toluene, the

nanoparticles are suspended in acetonitrile then isolated in a fritted-glass funnel and washed with ethanol to remove excess ligand. The purified nanoparticles are then suspended in toluene. As seen in Figure 1.4, the chemiresistor coated with a film synthesized via the single-phase method does not have a current strongly dependent on frequency. This indicates that the transport is dominated by tunneling and not ionic conduction. Transmission electron microscope (TEM) images of octanethiol (C8) coated gold nanoparticles and a histogram of diameters is shown in Figure 1.5.

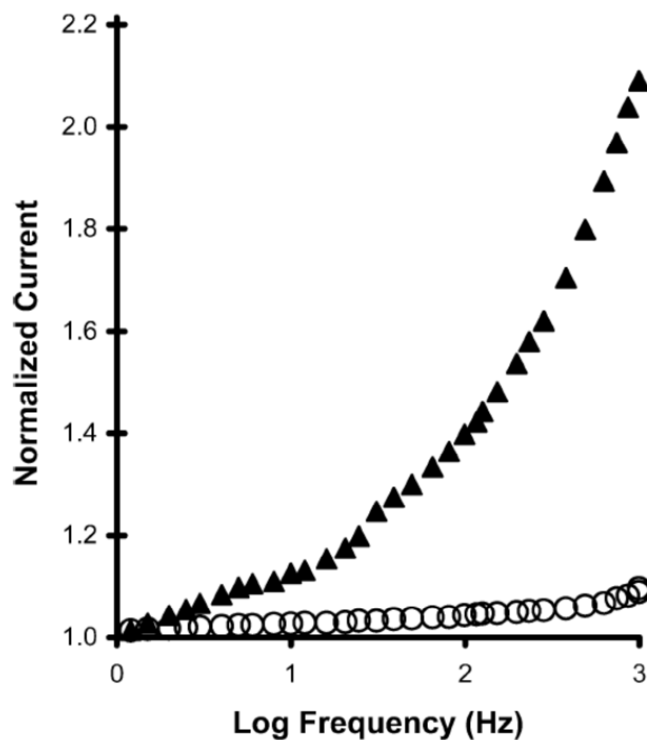

Figure 1.4 In-phase current through films of C12, normalized to the in-phase current value at 1 Hz ac frequency, as a function of the frequency of the applied voltage. In-phase current measurements were collected over a 1-kHz range where the parasitic effects of the out-of-phase current are negligible. Filled triangles: C12 prepared by the Brust method. Open circles: C12-Au prepared by the single-phase method. Reprinted from Rowe *et al.*[31].

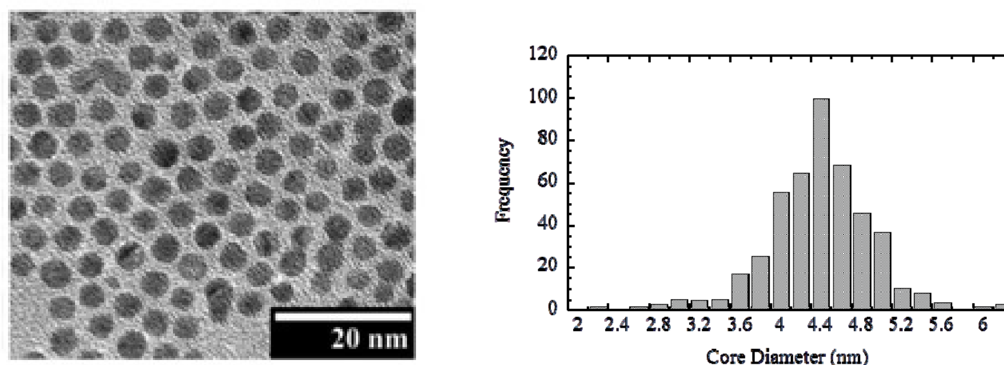

Figure 1.5 TEM image of C8 nanoparticles synthesized using a single phase synthesis method and a histogram of their diameters. Reprinted from Rowe *et al.* [31].

1.3 Gas Chromatography

Gas chromatography (GC) is a method of separating and identifying the components of mixtures of volatile compounds. A carrier gas is used to move the mixture through a long capillary tube, known as a column, whose inner surface is covered with a polymeric stationary phase. The VOCs in the mixture interact with the stationary phase by reversible partitioning causing each VOC to exit the column, or elute, at different times. Once the VOCs exit the column, they enter detector of the GC[35].

1.3.1 Micro-scale Gas Chromatography

Micro-scale gas chromatography (μGC) systems aim to scale down a traditional gas chromatography system by miniaturizing the components with micro-electromechanical systems technology making the system portable and low power while maintaining the performance of a GC system. In μGC systems, arrays of chemiresistors

with different MPN coatings are used as the detectors. By using an array of chemiresistors, each of which is coated with a film of MPNs having a different thiolate-monolayer structure, it is possible to obtain a pattern of responses that can assist in differentiating one vapor from another[6, 19, 20, 29, 36].

Like a traditional GC system, a μGC system separates mixtures of vapors for detection. This involves the microfabrication of the components. There have been a few reports on μGC systems, including work at the University of Michigan's Wireless Integrated Microsystems (WIMS) Center[14, 19, 20, 36-38]. A simplified schematic of a μGC is shown in Figure 1.6. A vapor mixture is captured through the inlet and sent to a preconcentrator. Mixtures are moved through the system by a micropump. The mixture is then separated through a microfabricated column. The compounds then exit the column and reach the chemiresistors at different times for identification. An array with different MPN coatings is used to help identify the mixture. The signals of the chemiresistors are read by the instrumentation electronics.

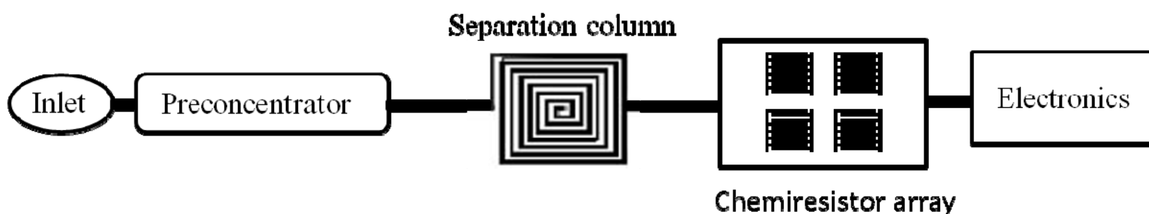

Figure 1.6 Basic schematic for a micro-gas chromatography system.

While this thesis focuses on the chemiresistor array, the research was done with a goal of integrating the array into a μGC system for the trace detection of explosives. This

project was collaborative effort between several research groups at the University of Michigan and Michigan State University. The collaboration was led by Dr. Edward T. Zellers, whose research group was responsible for many aspects of the μGC component fabrication, such as the columns, preconcentrators[39], and MPN synthesis[31]. The design of a read-out electronics chip was overseen by Dr. Andrew Mason, and we created a monolithic sensor system was fabricated using this chip[40]. The micro-fluidic packaging of the sensor system was led by Dr. Wen Li[41]. The work featured in this thesis was overseen by Dr. Çagliyan Kurdak and focuses on the MPN-coated chemiresistor arrays.

1.4 Chemiresistor Fabrication

The two components of a chemiresistor are the interdigitated electrodes (IDEs) and the MPN film. The IDEs can be easily fabricated with photolithography. As the components of the μGC system decrease, it may become necessary to shrink the components beyond the capabilities of photolithography. To create IDEs with submicron features, electron beam lithography can be used.

1.4.1 Electron Beam Lithography

Electron beam lithography (EBL) is analogous to photolithography but an electron source rather than light is used to alter the polymer resist. This is done with the use of a scanning electron microscope (SEM). While a mask is used in photolithography to expose selected areas, in EBL a SEM is programmed to expose the resist in a pattern

by scanning the beam in the desired region. Like in photolithography, there are both positive and negative resists. In a positive resist, the incident electrons will sever bonds within the resist rendering it soluble. In a negative resist, the resist is crosslinked and become insoluble[42].

Because of the high resolution of a SEM, EBL can be used to fabricate IDEs with submicron features[7, 43, 44]. Chemiresistors with electrodes with width and spacing of 100 nm have been reported[7, 45]. We have fabricated chemiresistors of this size, with electrodes with 100 nm width and spacing, as shown in Figure 1.7. Devices were fabricated by a typical liftoff process. A process outline for preparing samples for electron beam lithography is shown in Appendix A. A guide for adding contact pads for IDEs is outlined in Appendix B.

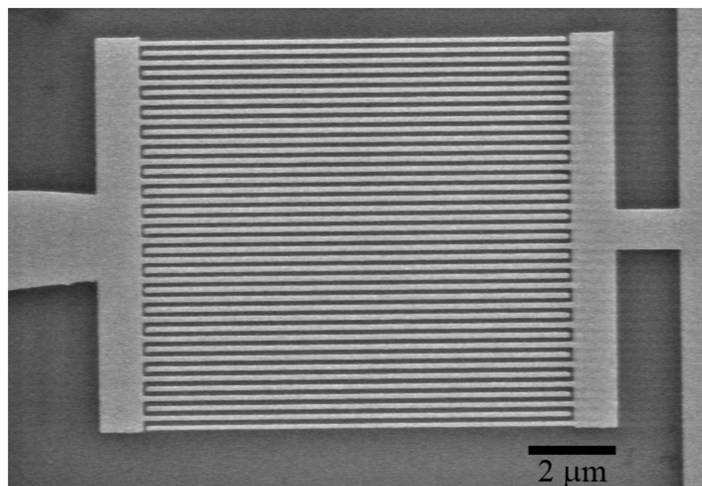

Figure 1.7 SEM image of an IDE with electrodes with 100 nm width and spacing and 10 μm in length.

Although EBL can be used to fabricate devices with sub-micron features, the resolution that can be obtained is constrained by the scattering of electrons. Incident

electrons can scatter within the resist layer causing a broadened beam effect. This is known as forward scattering and can be minimized by using the thinnest resist possible and the highest accelerating voltage. Electrons that penetrate the substrate can also backscatter. This can cause over exposure of the resist as well as exposure of unwanted regions. The indirect exposure of areas adjacent to the electron beam is known as the proximity effect. A practical resolution of 20 nm is observed due to beam broadening by secondary electrons[42].

1.4.2 MPN Film Coating

There are several methods that are widely used to coat IDEs with MPN films. One popular method is to create a film using an airbrush. This is done by propelling a nanoparticle solution with pressure regulated air. The mass deposited can be estimated by coating a thickness shear mode resonator alongside the sensor array[6]. The film thickness can be estimated (accurate only to one significant figure) by gravimetric measurements of the film mass[1].

Several techniques can be used to form monolayer MPN films. The Langmuir-Blodgett[46] and Langmuir–Schaeffer[47] techniques work by crosslinking neighboring nanoparticles with bifunctional linkers at the air/water interface while the sample is slowly withdrawn from solution. Monolayer films can also be formed by employing rapid early-stage evaporation and an attractive particle interface interaction by including excess thiol in the nanoparticle solution[48]. With excess thiol in the solution, monolayer islands of nanoparticles form on the top layer of the drop. These islands merge to create a

continuous monolayer. As the solvent evaporates, the monolayer approaches and eventually lies onto the substrate. While these techniques create highly uniform monolayer films, their high noise properties make them undesirable for sensor applications[49].

Methods such as dip-pen nanolithography[50], micro-contact printing[51], and micro-dispensing systems could potentially be used to pattern an array with several types of MPN films. Dip-pen nanolithography is done by loading an AFM tip with droplets of nanoparticle solutions. The tip is scanned across the surface, and the MPNs are deposited when their affinity for the surface exceeds that for the tip. This technique relies on the water meniscus between the AFM tip and the substrate. Therefore, only water soluble MPNs can be deposited. This technique can also be time prohibitive since the tip requires reloading after the MPNs on the tip are depleted. Micro-contact printing uses a stamp, usually comprised of polydimethylsiloxane (PDMS), inked with the desired solution. This technique requires the alignment of the stamp with the sensor array which may be difficult as the sensors decrease in size. Micro-dispensing systems, like inkjet printers, use piezoelectric controlled nozzles to eject droplets of solution onto a surface. If sensors are spaced wider than the area of the dried droplet, this technique can be used to pattern different arrays on MPNs. This technique suffers from the coffee stain phenomenon where the majority of the nanoparticles settle on the outer ring of the droplet[52]. An example of an array coated with a micro-dispensed film is shown in Figure 1.8. Using a Microfab Jetlab 4 dispensing system, we were able to coat an array with four different MPN films.

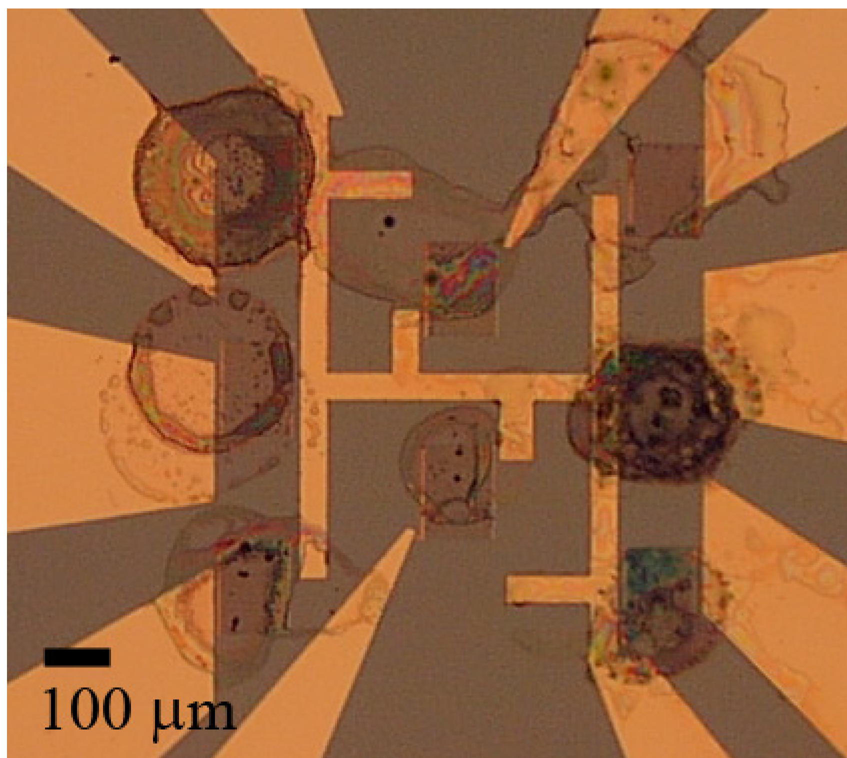

Figure 1.8 An eight sensor array coated with four different MPN films. The coffee stain pattern, where the majority of MPNs settle on the outer edge of the film is clearly seen.

Electron beam induced crosslinking can also be used to coat individual chemiresistors in an array with different MPN films[7, 30, 53, 54]. The incident electrons sever bonds within the ligand forming radicals free to link ligands on neighboring MPNs, rendering the film insoluble[54]. This technique can be used to precisely expose discrete areas in an array with the accuracy of an SEM and selectively crosslink MPNs on each sensor in an array sequentially. This technique can be exploited to pattern arrays with different MPN films. We patterned an OPH MPN film on an array with a 4 µm space between IDEs as shown in Figure 1.9. This technique will be discussed further in Chapter 3.

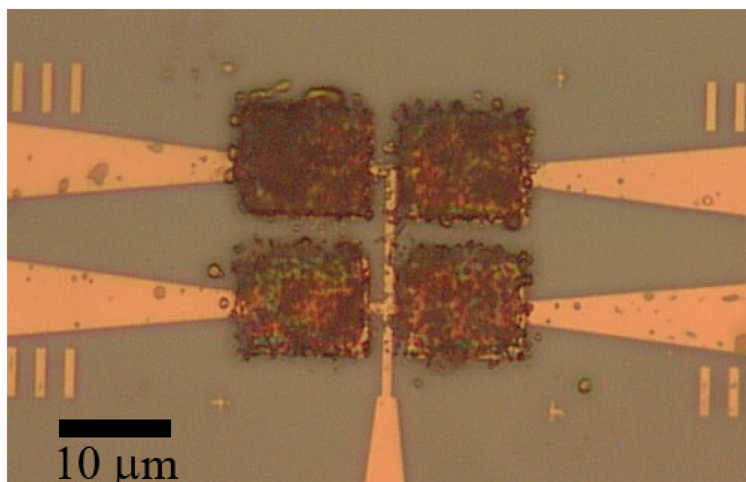

Figure 1.9 A 2×2 array has been patterned with an OPH MPN film via electron beam induced crosslinking. This technique has the resolution of a SEM; hence the spacing between the films (4 µm) can be easily seen.

1.5 Transport in Nanoparticle Films

It has been well established that electrical transport through the film is dominated by the tunneling of electrons between the gold cores[2, 3, 43, 55]. At low temperatures, MPN-coated chemiresistors show insulating behaviors due to single electron effects[2]. Unlike one and two dimensional networks of metallic islands[56], transport through a three dimensional MPN film is not well understood. Studies on alkanethiols show that tunneling can occur through the highest unoccupied molecular orbital (HOMO) or lowest unoccupied molecular orbital (LUMO)[57]. In order to better understand the electrical properties of MPN films, we have modeled the electric field through a MPN-coated chemiresistors to calculate the resistance and capacitance for a given electrode and film configuration.

1.5.1 Modeling of Capacitance and Resistance in an MPN Film

We modeled the electric field through an MPN film through Fourier series analysis. In this model, the IDEs are held at a potential, V, and separated by a distance, t, as shown in Figure 1.10. The nanoparticle film has thickness d with a dielectric constant κ_1. The region above the film is presumed to be infinite with a dielectric constant κ_2. This model can be used to calculate the resistance of a chemiresistor.

In addition to the resistance, the capacitance can also be monitored for the presence of a chemical species[58, 59]. These "chemicapacitors" function like chemiresistors except that their capacitance rather than resistance in monitored. This is due to a change in the permittivity of the film which alters the capacitance. Multimodal sensing, where both the resistance and capacitance response are monitored, may offer additional information for discriminating analytes.

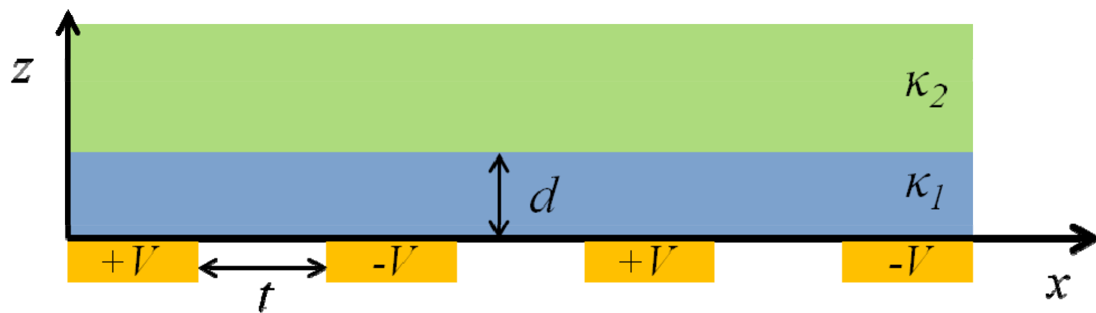

Figure 1.10 Schematic for the potential, V, of interdigitated electrodes separated by distance t with covered with a nanoparticle of thickness d and dielectric constant κ_1. The region above is infinite with dielectric constant κ_2.

The potential can be described as

$$V(x,z) = \sum_{n=1}^{\infty} V_n(z) \cos k_n x, \tag{1.1}$$

where x is perpendicular to the length of the electrodes, z is the surface normal,

$$k_n = \frac{n\pi}{2t}. \tag{1.2}$$

and

$$V_n(z) = \begin{cases} V_{n1}e^{-k_n z} + V_{n2}e^{k_n z} & 0 < z < d \\ V_{n3} - k_n z & d < z < 0 \end{cases}. \tag{1.3}$$

Using Maxwell's equations to solve for the boundary conditions, the coefficients are:

$$V_{n1} = \frac{V_{n0}(\kappa_1+\kappa_2)e^{2k_n d}}{\kappa_2(e^{2k_n d}-1)+\kappa_1(e^{2k_n d}+1)} \tag{1.4a}$$

$$V_{n2} = \frac{V_{n0}(\kappa_1+\kappa_2)e^{2k_n d}}{\kappa_2(e^{2k_n d}-1)+\kappa_1(e^{2k_n d}+1)} \tag{1.4b}$$

$$V_{n3} = \frac{V_{n0}(\kappa_1+\kappa_2)e^{2k_n d}}{\kappa_2(e^{2k_n d}-1)+\kappa_1(e^{2k_n d}+1)}. \tag{1.4c}$$

To determine the capacitance within the nanoparticle film region, $0 < z < d$, the electric field, E, can be calculated from V and used to calculate the energy density, u_E, and therefore the energy, U, which is related to capacitance as shown in Equations 1.5 and 1.6

$$U = \frac{1}{2}CV^2 \tag{1.5}$$

$$U = \iiint u_E dxdydz = \frac{1}{2}\varepsilon_0|E|^2 \tag{1.6}$$

where ε_0 vacuum permittivity. First, the electric field in the MPN region must be found.

$$E = -\nabla V = \left(-\frac{\partial}{\partial x}\hat{x} - \frac{\partial}{\partial z}\hat{z}\right) \sum_{n=1}^{\infty} V_n(z) \cos k_n x \quad (1.7a)$$

$$E = \sum_{n=1}^{\infty} k_n [\sin k_n x (V_{n1} e^{-k_n z} + V_{n2} e^{k_n z}) \hat{x} - \cos k_n x (-V_{n1} e^{-k_n z} + V_{n2} e^{k_n z}) \hat{z}] \quad (1.7b)$$

$$|E|^2 = \sum_{n=1}^{\infty} k_n [{V_{n1}}^2 e^{-2k_n z} + {V_{n2}}^2 e^{2k_n z} + 2V_{n1} V_{n2} (sin^2 k_n x - cos^2 k_n x)] \quad (1.7c)$$

Combining Equations 1.6 with 1.7c gives

$$U = \sum_{n=1}^{\infty} \frac{1}{4} \varepsilon_0 k_n A [{V_{n1}}^2 (1 - e^{-2k_n d}) + {V_{n2}}^2 (e^{2k_n d} - 1)] \quad (1.8)$$

where A is area of the sensor. Using Equation 1.5, the capacitance is found to be

$$C = \frac{1}{2V^2} \varepsilon_0 A \sum_{n=1}^{\infty} {k_n}^2 [{V_{n1}}^2 (1 - e^{-2k_n d}) + {V_{n2}}^2 (e^{2k_n d} - 1)]. \quad (1.9)$$

Using Equations 1.3 and 1.7b, the electric field lines and potential can be plotted for a given IDE and film configuration as shown in Figure 1.11. The interdigitated electrodes are represented by the gold bars and are separated by distance t. The shaded region indicates the area covered by the MPN film.

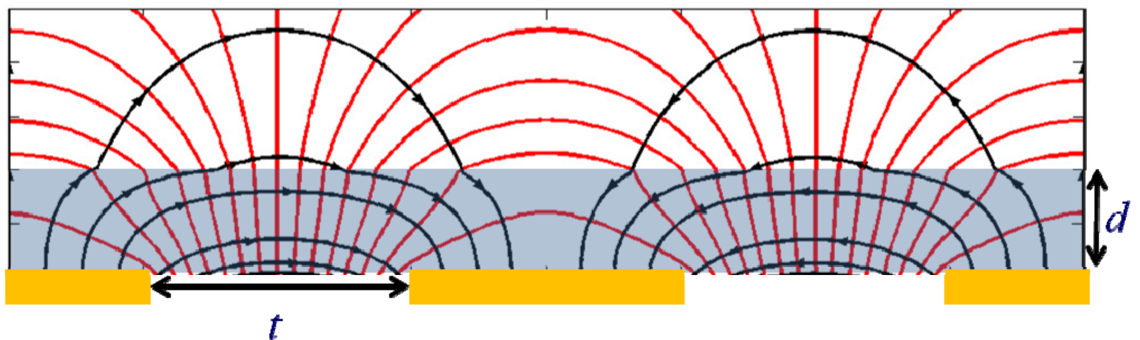

Figure 1.11 Electric field and potential lines for interdigitated electrodes (gold bars) with spacing t and a film thickness d (indicated by shaded region) with an arbitrary dielectric constant (κ=5) to represent the MPN film.

The conductance, G, can be calculated similarly. Conductance, which is the inverse of resistance, can be related to the power, P, by

$$G = {}^{1}/_{R} = {}^{I}/_{V} = {}^{P}/_{V^2}. \tag{1.10}$$

The total power can be expressed in terms of the electric field

$$P = \int \sigma |E|^2 dxdydz \tag{1.11}$$

where σ is the conductivity.

$$P = \frac{1}{4}\sigma A k_n [{V_{n1}}^2(1 - e^{-2k_n d}) + {V_{n2}}^2(e^{2k_n d} - 1)] \tag{1.11b}$$

Finally, the conductance be written as

$$G = \frac{1}{4V^2}\sigma A k_n [{V_{n1}}^2(1 - e^{-2k_n d}) + {V_{n2}}^2(e^{2k_n d} - 1)]. \tag{1.12}$$

1.5.2 Tunneling

The conduction of electrons between two metals separated by an insulating region is prohibited in classical physics. However, it has been proven with quantum mechanics that there is a probability of transmission through such barriers. This phenomenon of particles passing though barriers higher than their own energy is known as tunneling. This has been shown to be the dominant form of electron transport through MPN films[2, 3, 55, 60].

Consider a particle with mass m and energy E that encounters a potential barrier V, as shown in Figure 1.12.

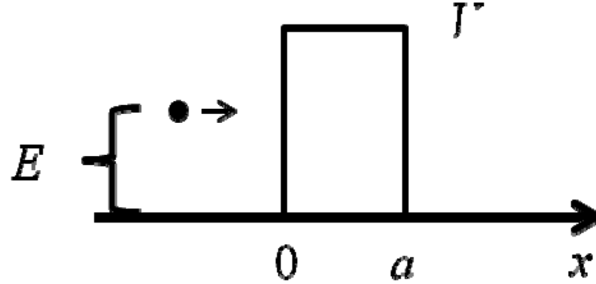

Figure 1.12 A particle with energy E encounters a potential barrier, V, of width a. Classically, the particle will rebound at $x = 0$, but quantum mechanics has proven that the particle has a probability of tunneling through the barrier.

The probability of finding the particle within a region is given by its wave function, $\psi(x)$. For a rectangular barrier, $\psi(x)$ is defined as follows for the three regions

$$\psi(x) = Ae^{-ikx} + Be^{ikx}, \ \ x < 0 \tag{1.13}$$

$$\psi(x) = Ce^{\kappa x} + De^{-\kappa x}, \quad 0 < x < a \tag{1.14}$$

$$\psi(x) = Fe^{-ikx}, \qquad x > a \tag{1.15}$$

where $= \sqrt{2mE/\hbar^2}$, $\kappa = \sqrt{2m(V-E)/\hbar^2}$, and A, B, C, D, E and F are constants. The probability of tunneling is given by the transmission coefficient, T.

$$T = |F/A|^2 \tag{1.16}$$

Solving for the boundary conditions that $\psi(x)$ and $\frac{\partial\psi(x)}{\partial x}$ be continuous at $x = 0$ and $x = a$ gives

$$T = 1/(1 + \frac{1}{4}\frac{V^2}{E(V-E)}\sinh^2(\kappa a)). \quad (1.17)$$

For the case of a slowly varying potential, the Wentzel–Kramers–Brillouin expansion is used to calculate *T*. By expanding the hyperbolic sine function in terms of exponentials and keeping only the leading term, Equation 1.17 can be approximated by

$$T = e^{-2\kappa a}. \quad (1.18)$$

For electron tunneling through an MPN, the width of the potential barrier will be the distance between neighboring nanoparticles, δ.

1.5.3 Distinguishing Electron and Hole Tunneling

While it has been determined that tunneling is the dominant method of transport in a MPN film, it is unknown whether electrons or holes are tunneling. Tunneling through a molecule can happen through the lowest unoccupied molecular orbital (LUMO) or highest occupied molecular orbital (HOMO) as shown in Figure 1.13.

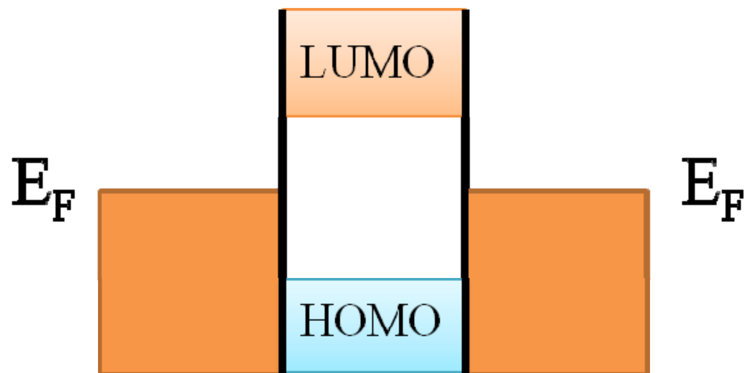

Figure 1.13 Energy diagram of two gold electrodes separated by an alkanethiol molecule. Tunneling can occur through either the LUMO or the HOMO.

Whether tunneling is through the LUMO or HOMO can be ascertained by measuring the thermoelectric voltage[61]. The sign of the voltage will indicate the location of the Fermi energy, E_F, with respect to the LUMO or HOMO. Proximity of E_F to the LUMO denotes electron tunneling, while proximity of E_F to the HOMO denotes hole tunneling. While current-voltage (I-V) measurements can determine whether transport is through tunneling, it does not reveal the position of the Fermi energy with respect to the LUMO and HOMO. We developed a new technique for measuring the thermoelectric voltage of MPN films which is presented in Chapter 5.

1.5.4 Coulomb Blockade

Chemiresistors coated with MPN films can exhibit nonlinear I-V characteristics low temperatures[2, 49]. Because electron transport through the film is by tunneling, resistivity of the film is highly sensitive to charging effects of the nanoparticles.

Tunneling through an MPN film can be thought of as tunneling through islands. When an electron tunnels to an island, the island becomes charged. The charging energy, E_c, is inversely proportional to the capacitance, C, of the island as shown in Equation 1.19.

$$E_c = e^2/2C \tag{1.19}$$

For small capacitance values, the charging energy can be large enough to prevent the tunneling of another electron. This happens when the charging energy is larger than energy associated with thermal fluctuations, k_BT, where k_B is the Boltzmann constant. The electrons do not have enough energy to overcome the charging barrier. This is known as Coulomb blockade.

Coulomb blockade also occurs when the charging energy is larger with the energy associated with quantum fluctuations, E_Q. This energy is defined through the Heisenberg Uncertainty Principle. An electron has an energy uncertainty defined by

$$\Delta E_Q \geq h/\Delta t, \tag{1.20}$$

where h is the Planck constant. A capacitor being charged through a resistor has a time constant of $t = RC$, therefore the Equation 1.20 becomes

$$\Delta E_Q \geq h/R_T C. \tag{1.21}$$

When the E_C exceeds E_Q, tunneling cannot occur.

$$e^2/2C \geq h/R_T C \tag{1.22}$$

Using Equation 1.22, the tunnel resistance, R_T, can be written as

$$R_T \geq {}^{h}\!/_{e^2}. \tag{1.23}$$

When the tunnel resistance is greater than ${}^{h}\!/_{e^2}$, or 25.8 kΩ, tunneling cannot occur.

The tunneling barrier can be overcome in the presence of a large enough bias voltage, V_b. When the bias voltage is smaller than the charge of the electron divided by the capacitance, tunneling cannot occur.

$$V_b < {}^{e}\!/_{C} \tag{1.24}$$

This behavior can be seen in the I-V characteristics of MPN films. In Figure 1.14, at low bias voltages, there is no current through the MPN film. At a certain threshold voltage, current will begin to flow. As the temperature decreases, the I-V curves become more and more non-linear due to the charging energy exceeding k_BT.

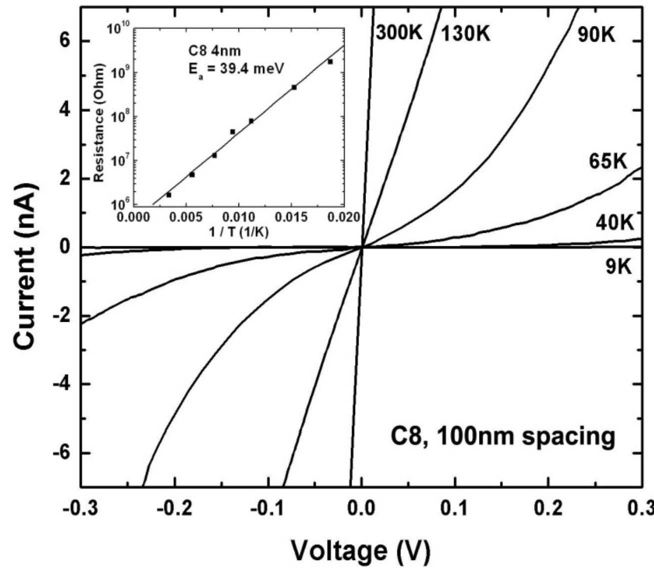

Figure 1.14 I-V characteristics of a 4 nm diameter C8 coated chemiresistor at different temperatures. Non-linear I-V curves are visible at lower temperatures indicative of Coulomb blockade. Reprinted from Kurdak *et al.*[2].

1.5.5 Charging Energy

An MPN can be thought of as a spherical capacitor consisting of a solid metal sphere of radius r, and a ligand shell of radius $r + \delta$. In an MPN film, the ligands have been found to intercalate nearly the entire length of the ligand[62]. For simplicity, δ will be used for both interparticle distance and the length of the ligand. The self capacitance of a MPN is therefore

$$C = 4\pi\kappa\varepsilon_0/(\frac{1}{r} - \frac{1}{r+\delta}) \quad (1.25)$$

where ε_0 is the permittivity and κ is the dielectric constant of the ligand layer. From Equation 1.19, the charging energy, E_c, can be calculated.

$$E_c = e^2(1 - \frac{r}{\delta+r})/8\pi\kappa\varepsilon_0 r \quad (1.26)$$

The resistivity of the film, ρ, will be proportional to the activation energy, E_a, using the Arrhenius equation

$$\rho \propto e^{E_a/k_B T}, \quad (1.27)$$

where T is temperature. E_a and E_C are not equal but are proportional. E_C is proportional to some fraction of E_C; therefore ρ will also scale with E_C. Note that E_C is not only dependent on δ but also κ. In the presence of an analyte with a large dielectric constant, E_C can be sufficiently lowered so that the increase in resistivity from the film swelling response is suppressed. This can lead to a reduction in resistance for certain analytes.

1.5.6 Transport Regimes through Metal Islands

While the dynamics of transport through islands is well understood, the transport through a MPN film is decidedly more complicated. The MPN film is essentially a three-dimensional (3D) network of tunneling islands with a random distribution of offset charges which lead to nonlinear current regimes. Although the transport through 3D metallic islands is not well understood, Middleton and Wingreen developed a theory to explain the transport through 1D and 2D arrays of metal islands at zero temperature[56]. In transport through metal dots separated by tunnel barriers, there are three transport regimes. As previously stated, Coulomb blockade will occur at small bias voltages until a threshold voltage, V_{th}, is reached. At V_b below V_{th}, there is no current flow as shown in Figure 1.15(a).

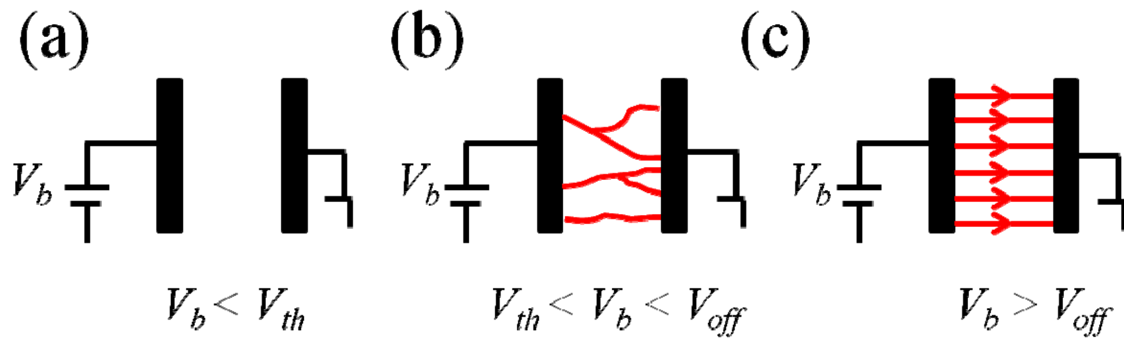

Figure 1.15 The three transport regimes, at *T*=0, for tunneling through metallic islands. (a) No current flows when the bias voltage, V_b, is below the threshold voltage, V_{th}. (b) In between V_{th} and V_{off}, where all channels are open, current flows nonuniformly through select channels. (c) At large V_b, all channels are open and current flows uniformly.

The threshold voltage was found to be proportional to the linear array size. At sufficiently high voltage, V_{off}, the I-V characteristics are linear and current flows through all channels. In between these two regimes is the scaling regime where current

flows nonuniformly through a select few channels that are energetically more favorable due to offset charge disorder. In this regime, the current scales as

$$I \sim \left({}^{V_b}/_{V_{th}} - 1 \right)^{\zeta} \tag{1.28}$$

where $\zeta = 1$ for a 1D array and $\zeta = 5/3$ for a 2D array and is depicted in Figure 1.15(b). In 2D arrays of metallic islands at nonzero temperature, subthreshold currents were found to be nonzero and were thermally activated with activation energies that decrease as the voltage is increased. When $V_b > V_{th}$, current was found to be independent of temperature at low temperatures[63], where $T < E_c/k_B$.

1.5.7 Engineering Transport Properties

As the diameter of the nanoparticle decreases, the charging energy can exceed the thermal energy causing Coulomb blockade at low temperatures. Because the charging energy is a function of the nanoparticle radius, it can be engineered by changing the size of the nanoparticles. Temperature dependent I-V measurements have shown the difference in transport properties of nanoparticles with different core diameters[2]. Nanoparticles with a smaller radius are found to have a larger Coulomb blockage gap as shown in Figure 1.16.

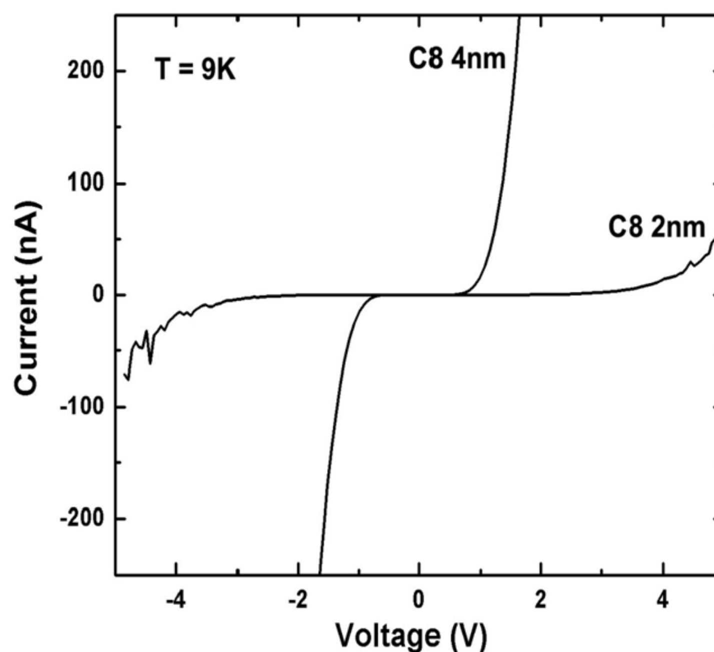

Figure 1.16 Coulomb blockade is more pronounced for the smaller (2 nm) diameter C8 MPN film. Reprinted from Kurdak *et al.*[2].

Tunneling can also be engineered through design of the ligand structure. Changing the length of the ligand will increase the spacing between particles, δ, causing an increase in resistivity as shown in Figure 1.17(a). The film with the longest ligands, octadecanethiol (C18), had a significantly higher resistance than octanethiol (C8) and dodecanethiol (C12)[2]. Ligands with a lower LUMO energy can also be used to alter the tunneling properties. 4-mercaptodiphenylacetylene (DPA), 4-nitro-4-mercaptodiphenylacetylene (NDPA), and 3,5-dinitro-4-mercaptodiphenylacetylene (DNDPA) were found to have lower tunneling resistance than a C12 film as shown in Figure 1.17(b).

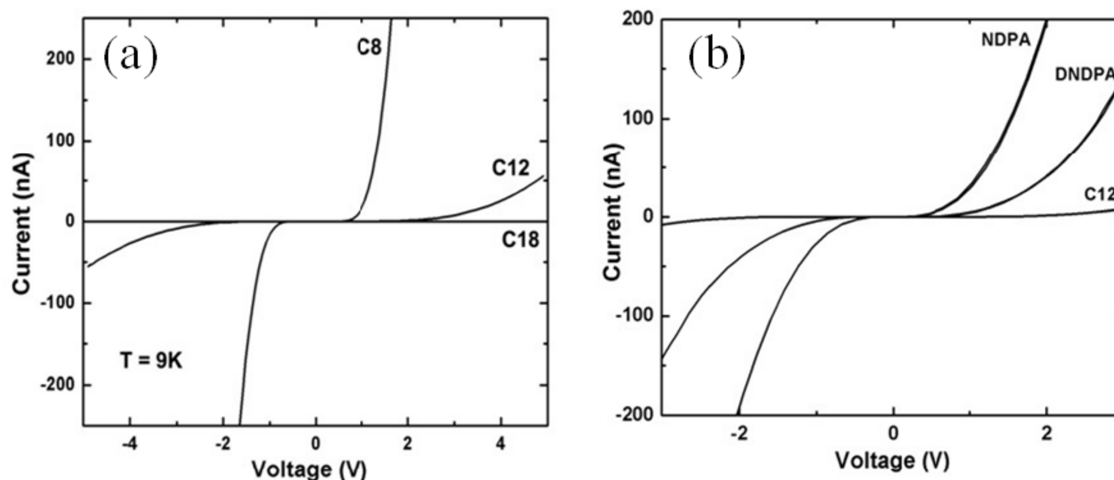

Figure 1.17 (a) I-V characteristics of C8, C12, and C18 MPNs at 9 K. MPNs with longer ligand are found to have an increase in resistance. (b) I-V characteristics of C12, NDPA, and DNDPA MPNs at 1.5 K. The tunnel coupling of MPNs can be changes by using ligands with different LUMO energies. Reprinted from Kurdak *et al* [2].

1.6 Improving Limit of Detection

The limit of detection (LOD) is given by the ratio of the background noise to the sensitivity. Particular interest has been taken in studying the sensitivity of such sensors, but there have been few studies on their noise properties. Since they rely on vapor partitioning, in principle, the sensitivity of MPN-coated chemiresistors should be independent of the size of the device. Evidence to support this has been published[6, 29]. However, the noise properties must also be considered, and previous reports have shown that such sensors exhibit $1/f$ type noise, with a noise prefactor of the normalized power spectral density function that scales inversely with the sensor area[64, 65].

1.6.1 1/*f* noise

Noise that scales inversely with frequency is referred to as $1/f$ noise, or flicker noise. Flicker noise refers to any noise spectrum that scales at $1/f^{\alpha}$, and $0 < \alpha < 2$ [66]. It is sometimes referred to as pink noise due to its scaling properties lying between those of white noise ($1/f^{0}$) and red noise ($1/f^{2}$). $1/f$ noise is often called ubiquitous due to its occurrence in widely different systems such as stock market systems[67], semiconductors[68], human cognition[69], and music[70]. An example of $1/f$ noise is shown in Figure 1.18.

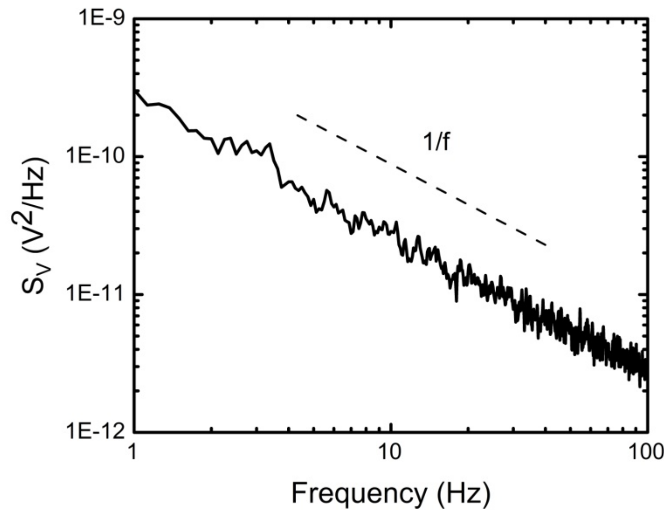

Figure 1.18 The power spectral density function, S_V, of a typical sensor coated with C8 nanoparticles exhibits $1/f$-type noise.

Chemiresistors utilizing MPN films as interfacial layers have been shown to exhibit $1/f$ type noise[49, 64, 65]. The noise prefactor has also been shown to scale inversely with sensor area indicating that the noise arises from intrinsic rather than extrinsic processes. Extrinsic processes, such as temperature fluctuations, would not scale with the size of the device. Possible causes of this noise could be anything that affects the tunnel

coupling between nanoparticles, such as the motion of the nanoparticles or conformational changes of the ligand sphere[65]. Devices of the same area have noise amplitudes that range three orders of magnitude. The cause of this scatter is unknown and is the subject of Chapter 2.

1.6.2 Optimizing Sensor Size

Since they rely on vapor partitioning, in principle, the sensitivity of MPN-coated chemiresistors should be independent of the size of the device[6, 29]. The noise of chemiresistors scales inversely with sensor area, A, which suggests that the smallest resistance change that can be detected in this type of chemiresistor would scale as $\sqrt{1/A}$. Thus, the limit of detection in terms of the mass of the analyte is expected to scale as $\sqrt{A}$, and using smaller chemiresistors should permit detection of smaller quantities of analytes.

At a systems level, in addition to the size of the sensor array, one must consider the diameter of the separation column, the volume of the head space of the detector cell in which the array is housed, the thickness of the MPN film deposited on each sensor, and the vapor-film partition coefficient of the analyte. These factors have not been studied systematically, but will all have an effect on the LOD. To achieve the highest performance for a given application, we must coordinate the scaling of all of the key components of a μGC system. The methodology associated with miniaturizing sensor

areas is presented in Chapter 3, and Chapter 6 focuses on the motivation and methodology for creating a microfabricated sensor system.

1.7 Chemiresistor Stability

Chemiresistors experience changes in baseline resistance, which have been hypothesized to be caused by degradation of the gold nanoparticle core or alkanethiol coating. Previous studies have shown that alkanethiols are susceptible to oxidation[71-74]. Oxidation of the sulfur bond has been shown to occur within hours of exposure to ambient air[73]. A recent study claims that oxidation of the thiol bond leads to a loss of the ligand coating and subsequently causes coalescence of nanoparticles[71].

For integration into a μGC system, chemiresistors must be functional for extended periods. For explosives detection, the system will most likely be heated to expedite the movement of the target analytes through the system due to their low volatility. It is therefore important to determine the stability of the MPN films at elevated temperatures. We studied the baseline drift and sensitivity to toluene vapor for chemiresistor arrays at elevated temperatures. The results are shown in Chapter 4. Electron beam induced crosslinking was also investigated as a possible means to decrease baseline drift.

1.8 References

1. H. Wohltjen and A. W. Snow, Anal. Chem. **70** (14), 2856-2859 (1998).
2. Ç. Kurdak, J. Kim, L. A. Farina, K. M. Lewis, X. Bai, M. P. Rowe and A. J. Matzger, Turk. J. Phys. **27**, 419-426 (2003).
3. P. E. Trudeau, A. Orozco, E. Kwan and A. A. Dhirani, J. Chem. Phys. **117** (8), 3978-3981 (2002).
4. A. W. Snow and H. Wohltjen, Chem. Mat. **10** (4), 947-949 (1998).
5. Y. Joseph, A. Peic, X. D. Chen, J. Michl, T. Vossmeyer and A. Yasuda, J. Phys. Chem. C **111** (34), 12855-12859 (2007).
6. W. H. Steinecker, M. P. Rowe and E. T. Zellers, Anal. Chem. **79** (13), 4977-4986 (2007).
7. E. Covington, F. I. Bohrer, C. Xu, E. T. Zellers and C. Kurdak, Lab Chip **10** (22), 3058-3060 (2010).
8. F. J. Ibanez and F. P. Zamborini, Langmuir **22** (23), 9789-9796 (2006).
9. E. T. Zellers, J. Park, T. Hsu and W. A. Groves, Anal. Chem. **70** (19), 4191-4201 (1998).
10. M. C. Lonergan, E. J. Severin, B. J. Doleman, S. A. Beaber, R. H. Grubb and N. S. Lewis, Chem. Mat. **8** (9), 2298-2312 (1996).
11. J. W. Gardner and P. N. Bartlett, Sen. Actuat. B-Chem. **18** (1-3), 211-220 (1994).
12. Q. Y. Zhong, R. A. Veeneman, W. H. Steinecker, C. R. Jia, S. A. Batterman and E. T. Zellers, J. Environ. Monit. **9** (5), 440-448 (2007).
13. J. S. Cooper, E. Chow, L. J. Hubble, L. Wieczorek, K.-H. Mueller and B. Raguse, Sens. Lett. **9** (2), 609-611 (2011).
14. S. K. Kim, H. Chang and E. T. Zellers, Anal. Chem. **83** (18), 7198-7206 (2011).
15. J. Yinon, Anal. Chem. **75** (5), 99-105 (2003).
16. R. R. Smardzewski, N. L. Jarvis, A. W. Snow and H. Wohltjen, *Nanoelectronic chemical sensors for chemical agent and explosives detection*. (2006).
17. J. W. Grate and M. H. Abraham, Sen. Actuat. B-Chem. **3** (2), 85-111 (1991).
18. J. Park, W. A. Groves and E. T. Zellers, Anal. Chem. **71** (17), 3877-3886 (1999).

19. C. J. Lu, W. H. Steinecker, W. C. Tian, M. C. Oborny, J. M. Nichols, M. Agah, J. A. Potkay, H. K. L. Chan, J. Driscoll, R. D. Sacks, K. D. Wise, S. W. Pang and E. T. Zellers, Lab Chip **5** (10), 1123-1131 (2005).

20. H. Kim, W. H. Steinecker, S. Reidy, G. R. Lambertus, A. A. Astle, K. Najafi, E. T. Zellers, L. P. Bernal, P. D. Washabaugh and K. D. Wise, Solid-State Sensors, Actuators and Microsystems Conference, 1505-1508 (2007).

21. S. K. Kim, H. Chang and E. T. Zellers, Solid-State Sensors, Actuators and Microsystems Conference, 128-131 (2009).

22. S. K. Kim, H. Chang, J. G. Bryant, D. R. Burris and E. T. Zellers, Solid-State Sensors, Actuators and Microsystems Conference, 799-802 (2011).

23. G. Serrano, H. Chang and E. T. Zellers, Solid-State Sensors, Actuators and Microsystems Conference, 1654-1657 (2009).

24. J. W. Grate, D. A. Nelson and R. Skaggs, Anal. Chem. **75** (8), 1868-1879 (2003).

25. L. Han, D. R. Daniel, M. M. Maye and C. J. Zhong, Anal. Chem. **73** (18), 4441-4449 (2001).

26. C. Thiruppathiraja, S. Kamatchiammal, P. Adaikkappan, D. J. Santhosh and M. Alagar, Anal. Biochem. **417** (1), 73-79 (2011).

27. J. M. Pingarrón, P. Yáñez-Sedeño and A. González-Cortés, Electrochimica Acta **53** (19), 5848-5866 (2008).

28. S. Guo and E. Wang, Analytica Chimica Acta **598** (2), 181-192 (2007).

29. Q.-Y. Cai and E. T. Zellers, Anal. Chem. **74** (14), 3533-3539 (2002).

30. F. I. Bohrer, E. Covington, C. Kurdak and E. T. Zellers, Anal. Chem. **83** (10), 3687-3695 (2011).

31. M. P. Rowe, K. E. Plass, K. Kim, Ç. Kurdak, E. T. Zellers and A. J. Matzger, Chem. Mat. **16** (18), 3513-3517 (2004).

32. M. Brust, M. Walker, D. Bethell, D. J. Schiffrin and R. Whyman, Chem. Commun. (7), 801-802 (1994).

33. C. A. Waters, A. J. Mills, K. A. Johnson and D. J. Schiffrin, Chem. Commun. (4), 540-541 (2003).

34. J. Guo, P. Pang and Q. Cai, Sen. Actuat. B-Chem. **120** (2), 521-528 (2007).

35. J. M. Miller, *Chromatography: concepts and contrasts*. (Wiley, 2005).

36. Q. Zhong, W. H. Steinecker and E. T. Zellers, Analyst **134** (2), 283-293 (2009).

37. S. Zampolli, I. Elmi, F. Mancarella, P. Betti, E. Dalcanale, G. C. Cardinali and M. Severi, Sens. Actuator B-Chem. **141** (1), 322-328 (2009).

38. P. R. Lewis, P. Manginell, D. R. Adkins, R. J. Kottenstette, D. R. Wheeler, S. S. Sokolowski, D. E. Trudell, J. E. Byrnes, M. Okandan, J. M. Bauer, R. G. Manley and C. Frye-Mason, IEEE Sens. J. **6** (3), 784-795 (2006).

39. T. Sukaew, H. Chang, G. Serrano and E. T. Zellers, Analyst **136** (8), 1664-1674 (2011).

40. X. Mu, E. Covington, D. Rairigh, Ç. Kurdak, E. T. Zellers and A. Mason, submitted (2011).

41. N. Ward, X. Mu, G. Serrano, E. Covington, Ç. Kurdak, E. T. Zellers, A. Mason and W. Li, submitted (2011).

42. M. A. McCord and M. J. Rooks, in *SPIE's Handbook of Microlithography, Micromachining, and Microfabrication* (SPIE, Bellingham, Washington, 1997), Vol. 1, pp. 139-250.

43. M. G. Ancona, A. W. Snow, E. E. Foos, W. Kruppa and R. Bass, IEEE Sens. J. **6** (6), 1403-1414 (2006).

44. F. I. Bohrer, E. Covington, C. Kurdak and E. T. Zellers, Solid-State Sensors, Actuators and Microsystems Conference, 148-151 (2009).

45. K. Ueno, M. Hayashida, J.-Y. Ye and H. Misawa, Electrochem. Commun. **7** (2), 161-165 (2005).

46. S. W. Chen, Langmuir **17** (9), 2878-2884 (2001).

47. A. Nabok, S. Y. Heriot and T. H. Richardson, Phys. Status Solidi B **242** (4), 797-802 (2005).

48. T. P. Bigioni, X.-M. Lin, T. T. Nguyen, E. I. Corwin, T. A. Witten and H. M. Jaeger, Nat. Mater. **5** (4), 265-270 (2006).

49. E. L. Covington, R. W. Turner, C. Kurdak, M. P. Rowe, X. Chao and E. T. Zellers, Proceedings of the IEEE Sensors Conference, 102-105 (2008).

50. W. C. M. Wang, R. M. Stoltenberg, S. H. Liu and Z. N. Bao, ACS Nano **2** (10), 2135-2142 (2008).

51. F. J. Ibanez, U. Gowrishetty, M. M. Crain, K. M. Walsh and F. P. Zamborini, Anal. Chem. **78** (3), 753-761 (2006).

52. R. D. Deegan, O. Bakajin, T. F. Dupont, G. Huber, S. R. Nagel and T. A. Witten, Phys. Rev. E **62** (1), 756 (2000).

53. W. H. Steinecker, K. Sun Kyu, F. I. Bohrer, L. Farina, C. Kurdak and E. T. Zellers, IEEE Sens. J. **11** (2), 469-480 (2011).

54. M. H. V. Werts, M. Lambert, J. P. Bourgoin and M. Brust, Nano Letters **2** (1), 43-47 (2002).

55. M. G. Ancona, W. Kruppa, R. W. Rendell, A. W. Snow, D. Park and J. B. Boos, Phys. Rev. B **64** (3) (2001).

56. A. A. Middleton and N. S. Wingreen, Phys. Rev. Lett. **71** (19), 3198-3201 (1993).

57. W. Y. Wang, T. Lee and M. A. Reed, Rep. Prog. Phys. **68** (3), 523-544 (2005).

58. S. V. Patel, T. E. Mlsna, B. Fruhberger, E. Klaassen, S. Cemalovic and D. R. Baselt, Sen. Actuat. B-Chem. **96** (3), 541-553 (2003).

59. P. Oikonomou, G. P. Patsis, A. Botsialas, K. Manoli, D. Goustouridis, N. A. Pantazis, A. Kavadias, E. Valamontes, T. Ganetsos, M. Sanopoulou and I. Raptis, Microelectron. Eng. **88** (8), 2359-2363 (2011).

60. R. H. Terrill, T. A. Postlethwaite, C. H. Chen, C. D. Poon, A. Terzis, A. D. Chen, J. E. Hutchison, M. R. Clark, G. Wignall, J. D. Londono, R. Superfine, M. Falvo, C. S. Johnson, E. T. Samulski and R. W. Murray, J. Am. Chem. Soc. **117** (50), 12537-12548 (1995).

61. M. Paulsson and S. Datta, Phys. Rev. B **67** (24), 241403 (2003).

62. M. D. Porter, T. B. Bright, D. L. Allara and C. E. D. Chidsey, J. Am. Chem. Soc. **109** (12), 3559-3568 (1987).

63. Ç. Kurdak, A. J. Rimberg, T. R. Ho and J. Clarke, Phys. Rev. B **57** (12), R6842-R6845 (1998).

64. W. Kruppa, M. G. Ancona, R. W. Rendell, A. W. Snow, E. E. Foos and R. Bass, Appl. Phys. Lett. **88** (5) (2006).

65. C. Kurdak, J. Kim, A. Kuo, J. J. Lucido, L. A. Farina, X. Bai, M. P. Rowe and A. J. Matzger, Appl. Phys. Lett. **86** (7), 073506 (2005).

66. P. Dutta and P. M. Horn, Reviews of Modern Physics **53** (3), 497-516 (1981).

67. A. W. Lo, Econometrica **59** (5), 1279-1313 (1991).

68. F. N. Hooge, IEEE Trans. Electron Devices **41** (11), 1926-1935 (1994).

69. D. L. Gilden, T. Thornton and M. W. Mallon, Science **267** (5205), 1837-1839 (1995).

70. R. F. Voss and J. Clarke, Nature **258** (5533), 317-318 (1975).

71. Y. Joseph, B. Guse and G. Nelles, Chem. Mat. **21** (8), 1670-1676 (2009).

72. T. M. Willey, A. L. Vance, T. van Buuren, C. Bostedt, L. J. Terminello and C. S. Fadley, Surf. Sci. **576** (1-3), 188-196 (2005).

73. M. H. Schoenfisch and J. E. Pemberton, J. Am. Chem. Soc. **120** (18), 4502-4513 (1998).

74. N. Sandhyarani and T. Pradeep, Chem. Phys. Lett. **338** (1), 33-36 (2001).

Chapter 2

Electrical Noise in Gold Thiolate Nanoparticle Chemical Sensors

2.1 Introduction

The measurement of any signal is obscured by additional unwanted signals known as noise. Noise can arise from intrinsic processes within the quantity being measured or from external influences. Techniques such as low-noise amplifiers, filtering, and signal averaging can be used to reduce the measured noise but not the noise itself. Studying the intrinsic noise of a system can lead to an understanding of the fundamental cause of the noise. Finding the cause may enable one to decrease the noise within a system.

Understanding the fundamental noise for chemiresistors is important because the limit of detection (LOD) is dependent on the noise. The International Union of Pure and Applied Chemistry (IUPAC) defines LOD as the smallest measured, x_L, that can be detected with reasonable certainty for a given analytical procedure[1]. The value of x_L is given by

$$x_L = \bar{x}_{bi} + k\sigma_{bi} \quad (2.1)$$

where $\bar{x}_{bi}$ is the mean of the blank measurement, σ_{bi} is the standard deviation of the blank measure, and k is a numerical factor that is chosen according to the confidence

level desired and if often chosen to be three. For a chemiresistor, the blank measurement will be the baseline resistance of the chemiresistor in the absence of a chemical species.

While this is the most commonly used method for determining the limit of detection, it does not express the fundamental limit of detection. The blank measurement of a sensor can vary greatly between systems due to noise from the readout electronics. In order to determine the fundamental LOD, it must be defined in terms of the fundamental noise of the sensor.

A more accurate definition of LOD for a chemiresistor is the ratio of the noise to the sensitivity where the sensitivity is the normalized change in resistance, ${}^{\Delta R}/_{R_b}$, over the vapor concentration.

$$Sensitivity = ({}^{\Delta R}/_{R_b})/C_{ppm} \tag{2.2}$$

In Equation 2.2, R_b is the baseline resistance and C_{ppm} is the concentration in part per million. While particular interest has been taken in studying the sensitivity of chemiresistors, there have been few studies on their noise properties. Chemiresistors have been shown to exhibit 1/*f*-type, where the noise scales inversely with frequency, *f*. Studies have shown that 1/*f* noise of chemiresistors scales inversely with area, indicating it is caused by intrinsic processes[2, 3]. Sensors of the same area have large variations in their noise amplitude, and the cause of this scatter was investigated. We studied the change in noise amplitude from variations in the thickness of the MPN film, film purity, and amount of electron beam crosslinking.

2.2 Noise Power Spectral Density Function

When measuring the noise of a voltage signal, the noise is commonly presented as the root mean square voltage, V_{rms}. As shown in Equation 2.3, this is the square root of the mean of the squared voltage, V.

$$V_{rms} = \sqrt{\langle V(t)^2 \rangle} \tag{2.3}$$

While this is a widely used practice for expressing noise, it is an inferior representation of the true noise of the system, because it is dependent on the bandwidth of the measurement. To determine the noise independent of bandwidth, the noise power spectral density function should be measured. This is the noise power per unit bandwidth and describes how the noise is distributed with respect to frequency.

To understand the meaning of the noise power spectral density function, begin with a voltage signal. Measuring the voltage of a device over a period $-T \leq t \leq T$ will give an average voltage, $\langle V \rangle$.

$$\langle V \rangle = \frac{1}{2T} \int_{-T}^{T} V(t) dt \tag{2.4}$$

To represent the magnitude of how much the voltage varies, the root mean square voltage, V_{rms}, is usually presented.

$$V_{rms} = \sqrt{\langle V(t)^2 \rangle} = \sqrt{\frac{1}{2T} \int_{-T}^{T} [V(t)]^2 dt} \tag{2.5}$$

The autocorrelation function for voltage is defined as

$$R(\tau) = \langle V(t)V(t-\tau) \rangle = \frac{1}{2T} \int_{-T}^{T} V(t)V(t-\tau) dt. \tag{2.6}$$

Note that for $\tau = 0$, this will be equal to ${V_{rms}}^2$. Taking the Fourier transform of the autocorrelation function gives the power spectral density function, $S(f)$ where f is frequency. The one sided Fourier transform of the autocorrelation function is defined as

$$S(f) = \mathcal{F}(R(\tau)) = \int_0^\infty F(\tau) e^{-2\pi i f \tau}\, d\tau. \tag{2.7}$$

For voltage, the noise power spectral density function will be referred to as $S_V(f)$.

2.2.1 Thermal Noise

Chemiresistors have multiple sources of noise. Like all resistors, they have thermally activated noise, or Johnson noise[4]. This type of noise is referred to as white noise, because it has a flat frequency spectrum. The noise power spectral density function, $S_v^{thermal}$, for a resistor, R, at temperature T is

$$S_v^{thermal}(f) = 4 k_B T R \tag{2.8}$$

where k_B is the Boltzmann constant. Note that this form of noise is fundamental and irreducible.

2.2.2 1/f-type noise

Chemiresistors have also been shown to exhibit 1/f type noise or flicker noise. A brief introduction to 1/f type noise is presented in Chapter 1. Flicker noise occurs in a wide variety of systems, and no unifying principle has been found to explain its

existence[5, 6]. At low frequencies, flicker noise is the dominant form of excess noise[6]. Though once thought to be a surface effect, it has been shown to scale with the number of charge carriers within a device indicating it is caused by intrinsic processes [7]. For voltage, the power spectral density function for flicker noise is defined as

$$S_V^{flicker}(f) = \frac{\alpha_H}{N}\frac{V^2}{f} \tag{2.9}$$

where N is the number of charge carriers and α_H is the Hooge parameter. Note that this is independent of temperature and material parameters. Since the noise is inversely proportional to N, and therefore sample volume, it is thought to be a bulk rather than surface effect.

2.3 Measuring Noise Amplitude

The noise power spectral density function can be measured using a spectrum analyzer. A typical experimental set-up to measure noise is shown in Figure 2.1. A voltage bias is applied across the chemiresistor. The signal is then sent to a low-noise current sensitive amplifier. The gain of the amplifier is controlled through a feedback resistor. An EG&G PARC 181 current sensitive amplifier was used with a selectable gain ranging from 10^{-4} A/V to 10^{-9} A/V. The noise power spectral density function is then measured by a SR780 spectrum analyzer which takes the fast Fourier transform (FFT) of the input voltage signal to compute its frequency spectrum.

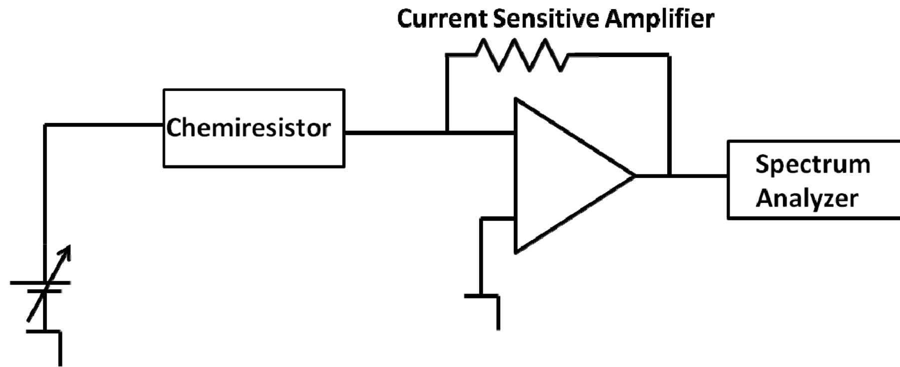

Figure 2.1 Experimental set-up for measuring noise of a chemiresistor using a variable bias voltage, current sensitive amplifier and spectrum analyzer.

The power spectral density function has units of V^2/Hz. The noise power spectral density function for a typical C8 coated chemiresistor at bias voltages of 0.1 and 0.3 V is shown in Figure 2.2. The inset of Figure 2.2 shows that $S_V(f)$ scales quadratically with the applied voltage.

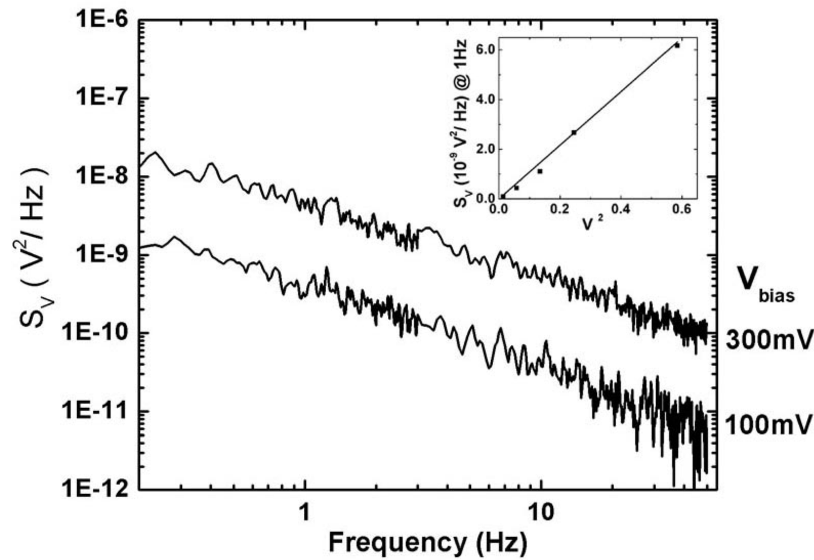

Figure 2.2 The noise power spectral density function, $S_V(f)$, for a chemiresistor at bias voltages of 0.1 and 0.3 V. As shown in the inset, $S_V(f)$ scales quadratically with voltage.

The noise amplitude, A, is calculated from the power spectral density function as shown below.

$$S_I/_{I^2} = S_V/_{V^2} = A/_f \tag{2.10}$$

2.3.2 Scaling in Noise Amplitude

Several studies on chemiresistors utilizing MPN films as interfacial layers have shown that they exhibit $1/f$ type noise[2, 3, 8] where the noise scales inversely with frequency. The noise amplitude has also been shown to scale inversely with sensor area, as shown in Figure 2.3, indicating that the noise arises from intrinsic processes. If the noise was caused by an extrinsic process, such as temperature, it would be independent of the size of the device. When the noise scales with the device size, the cause of the noise cannot be attributed to an external influence and is therefore caused by an intrinsic process. A recent study has also compared the noise amplitude of MPN coated resistors measured in both air and water[9]. The noise prefactor was found to be independent of the measurement environment further proving that $1/f$ noise is not caused by surface effects.

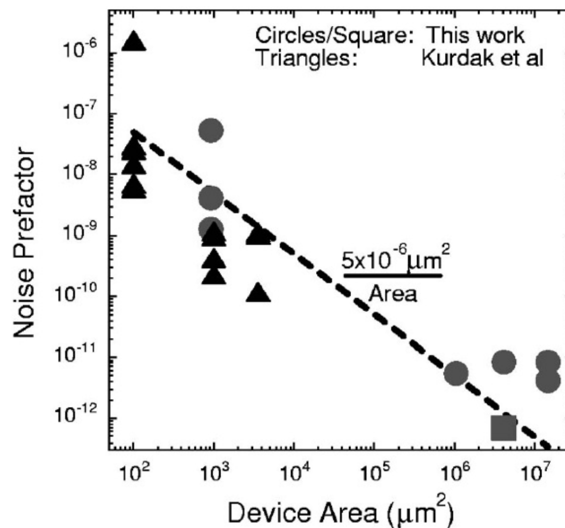

Figure 2.3 The noise amplitude, or prefactor, of a chemiresistor scales inversely with sensor area. Reprinted from Kruppa *et al.*[3].

Note the large scatter in the data from Figure 2.3. A device with area 10^3 μm^2 can have a noise prefactor spanning three orders of magnitude. The large scatter in noise amplitude was the motivation for this study. To determine a cause for this scatter, we studied chemiresistors of the same area. The chemiresistor's volume was changed by altering the film thickness. We extracted the noise amplitude from the power spectral density function in order to determine if variations in film thickness and film uniformity were the cause of the large scatter in noise amplitude.

2.4 Fabrication of Chemiresistors

In this study, chemiresistors were made of interdigitated electrodes (IDEs) coated with nanoparticle films. We fabricated IDEs via electron beam lithography and a liftoff process to create 200 Å thick electrodes with a 20 Å titanium adhesion layer. IDEs were

made with 300 nm electrode width and spacing comprising an active area of $50\times60\ \mu m^2$. A scanning electron microscope (SEM) image of an IDE is shown in Figure 2.4.

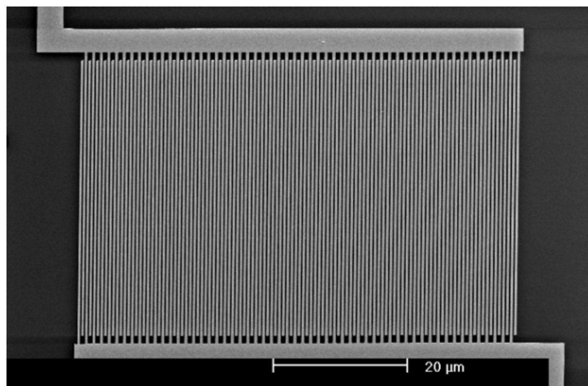

Figure 2.4 A $50x60\ \mu m^2$ device comprised of interdigitated electrodes with 0.3 µm width and spacing.

2.4.2 Micro-deposition of Nanoparticle Solutions

The coating of the nanoparticle films was done using a Microfab Jetlab 4 micro-dispensing system. This system allows one to dispense a small amount of solution on the surface of a substrate at a specified point. In this study, the nanoparticle solutions were comprised of 1-octanethiol (C8) nanoparticles in toluene or trichloroethylene (TCE). Each drop, as shown in Figure 2.5, had a diameter of approximately 75 µm. A single IDE on an array was coated by dispensing one drop of the solution and waiting for the droplet to dry on the surface of the sensor. When the solution hits the surface, it fully covers the active region of the interdigitated electrodes. After waiting several minutes for the droplet to dry, another droplet was deposited.

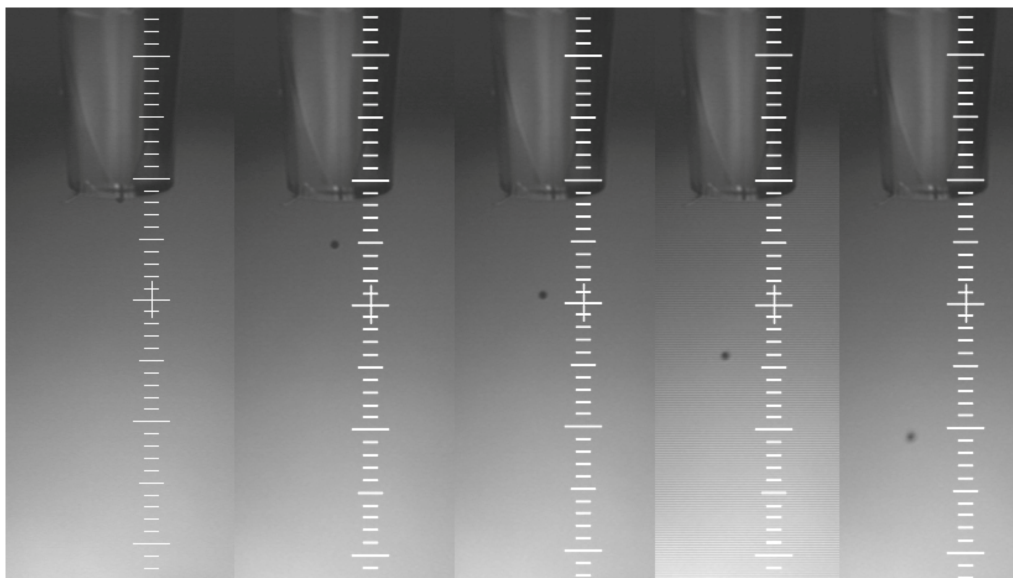

Figure 2.5 Progression of a drop of toluene as it is ejected from the micro-dispensing system. Each division is 100 μm, therefore the droplet is approximately 75 μm in diameter.

Although the micro-dispensing system could effectively coat the sensors with a nanoparticle film, the resulting film was highly non-uniform. The deposited nanoparticles would obtain a "coffee stain" pattern, where the majority of the nanoparticles settled in a ring on the outside of the droplet as shown in Figure 2.6. This occurs when the contact line is pinned to the substrate, which can be caused by surface roughness or chemical heterogeneities. As the liquid from the edge of the droplet evaporates, liquid is replenished from a flow from the interior of the droplet. The flow accounts for the transfer of the solute to the outer edge of the droplet and the formation of a ring pattern[10].

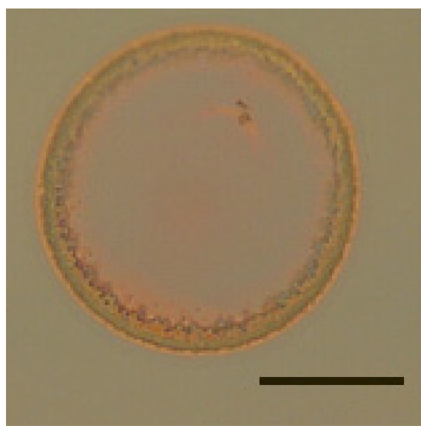

Figure 2.6 Nanoparticles dry in a "coffee ring" pattern where the majority of nanoparticles settle in a thick outer ring leaving a thinner interior film. The scale bar indicated 75 µm.

2.4.3 Monolayer Films Deposition

In order to produce a more uniform film, we created a monolayer of MPNs on a chemiresistor by controlling the evaporation kinetics and particle interaction with the liquid-air interface[11]. This is done by employing rapid early-stage evaporation and an attractive particle interface interaction by including excess thiol in the nanoparticle solution. Monolayer islands form on the surface of the drop and eventually merge to create a continuous monolayer across in entire liquid-air interface. As the liquid evaporates, the monolayer moves toward the surface eventually leaving the monolayer sheet on the substrate. The creation of a monolayer was confirmed by visual inspection of the film under the microscope.

2.5 Noise Amplitude Versus Film Morphology

We coated four chemiresistors with the micro-dispensing system, and noise measurements were performed after each interval of depositing five drops. The sensor's noise was measured with a setup consisting of a battery operated DC power supply, a low-noise current sensitive amplifier, and a spectrum analyzer. For most of the noise measurements, the voltage was set to 500 mV and the gain of the amplifier was 10^{-7} A/V. Sensors were also measured at different bias voltages to check the linearity of the device current as well as noise. In the first sensor studied, noise measurements were taken after every deposition of five drops of C8 dissolved in toluene until 50 drops had been deposited on the sensor. Noise measurements were then taken with 65, 80, and 100 drops deposited on the sensor. Another sample was coated from the same C8 in toluene solution with measurements ranging from 5 to 60 drops. An additional sample was studied using a similar method with C8 dissolved in trichloroethylene (TCE). Noise measurements on the monolayer film coated sensors were performed using the same experimental setup. Current-voltage (I-V) measurements were also taken on the monolayer coated sensors.

2.5.1 I-V Characteristics of Monolayer Films

We studied the I-V characteristics of the self assembled monolayer films and found them to be nonlinear. In Figure 2.7, we show a typical I-V curve taken on a monolayer film at room temperature. The nonlinearity of the I-V characteristics arises from the Coulomb Blockade effect. The Coulomb Blockade effect on thick films of nanoparticles was previously studied by measuring temperature dependent I-V

measurements. The activation energy for transport is approximately 40 meV for C8 nanoparticles with a 4 nm diameter[12]. In monolayer films, the nanoparticles will have only 6 nearest neighbors instead of 12; therefore the capacitance of the particles will be smaller. Thus, charging energy for tunneling and the associated activation energy for electrical transport are expected to be larger, which would explain why the nonlinearity persists even at room temperature in monolayer films.

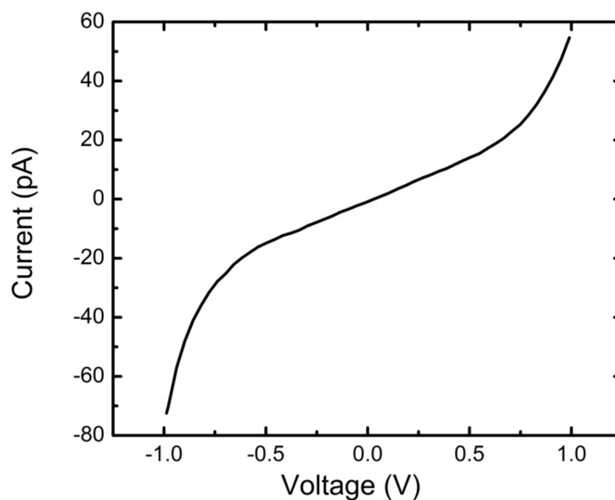

Figure 2.7 Chemiresistors coated with a monolayer film exhibit Coulomb blockade behavior at room temperature.

2.5.2 Noise Amplitude Versus Chemiresistor Resistance

All chemiresistors we studied exhibited 1/*f* type noise. There was an approximately five order of magnitude scatter in the noise amplitude extracted from the same area sensors. Both the resistance of the films and the noise prefactor were decreased as more and more nanoparticles were added onto the sensors. Since using a technique such as atomic force microscopy to obtain an accurate film thickness for each droplet

deposition would be time prohibitive, the assumption was made that more deposited nanoparticles leads to a thicker film and therefore a lower resistance. While this is mostly true, it is possible that depositing more drops can lead to a lower resistance. Additional drops can rewet the previous nanoparticle film and create an entirely new film. If the majority of the nanoparticles do not dry within the active region of the IDEs, the resistance can be lowered.

Figure 2.8 shows the noise prefactor versus resistance for all the sensors. Monolayer films had the highest noise prefactor, while sensors with thick films, deposited by the micro-dispensing system, had significantly lower noise. This result is not unexpected; in situations where $1/f$ noise is caused by intrinsic processes, the noise is expected to scale inversely with the volume of the device[7]. Thicker films result in more nanoparticles participating in the current therefore lowering the resistance of the sensors as well as the noise prefactor. While monolayer films had the most uniform film thickness, their high resistance and noise prefactor make them undesirable for use as a sensor.

Note that sensors coated from the same nanoparticle solutions follow the same linear trend. The two samples coated from solution of C8 in toluene follow the same linear relationship between noise amplitude and resistance. The other sample that was coated from the solution of C8 in TCE follow a linear trend, but its resistance is lower than the other samples with the same noise prefactor. Other than film thickness variations, scatter in noise data could be cause by variations in the nanoparticle solutions

itself. For example, different nanoparticle batches could have varying levels of purity causing variations in baseline resistance.

Figure 2.8 Chemiresistors with monolayer films of octanethiol (C8) MPNs have the highest noise prefactor while films deposited with the micro-dispensing system can have 5 times lower noise depending on film thickness. The scatter in the data may be caused by differences in nanoparticles solutions.

2.6 Nanoparticle Film Contamination

As previously discussed, one possible cause of the large scatter in the noise properties of chemiresistors could be contaminants within the MPN film. Impurities, such as ionic contaminants from the nanoparticle synthesis, could have significant effects on the electronic properties of the film and cause irreversible changes in the baseline resistance of the sensors. Nanoparticles have been synthesize using a single phase synthesis[13] in order to eliminate ionic contaminants commonly introduced using the Brust

synthesis method[14]. It is still possible that other contaminants could be incorporated into the film during the synthesis or film deposition process.

In order to study the effects of contaminants on vapor sensitivity, we systematically contaminated a C8 nanoparticle solution with the organic compound naphthalene. An array, with sensors with an area of 0.5×0.5 mm^2, was coated with a C8 nanoparticle film with 0% or 20% naphthalene. The noise amplitude was then measured, and the results are shown in Figure 2.9. As in Figure 2.8, chemiresistors with larger resistance have larger noise amplitudes. This was found for both “pure” and contaminated chemiresistors. For chemiresistors with similar resistance values, there were still large variations in the noise amplitude spanning one to two orders of magnitude. This cannot be attributed to the percent of naphthalene contamination, because it was also seen in the uncontaminated samples.

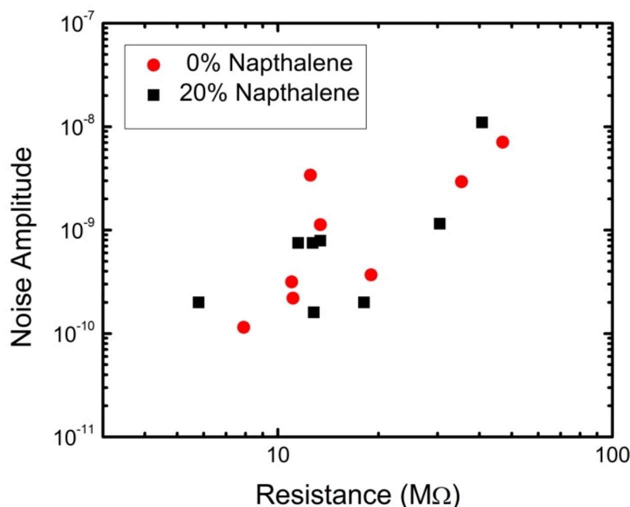

Figure 2.9 Noise amplitude versus resistance for chemiresistors with either 0% or 20% naphthalene added to the C8 nanoparticle solution. The trend follows that of Figure 2.8 where chemiresistors of high resistance have larger noise amplitudes, but the large scatter in the data cannot be attributed to naphthalene contamination.

2.7 Electron Beam Induced Crosslinking for Noise Reduction

One possible cause of noise in chemiresistors could be the motion of nanoparticles or conformation changes of the ligand coating. To reduce these possible causes of noise, we crosslinked the films via electron beam exposure. This is done by exposing the nanoparticle film to a high energy electron beam which is done with a scanning electron microscope. The incident electrons sever bonds within the ligand forming radicals free to link neighboring particles[15]. This will cause a more rigid nanoparticle film by limiting the movement of the nanoparticles. If noise is caused by the movement of nanoparticles, electron beam induced crosslink should lead to a reduction of the noise prefactor.

To test this hypothesis, we exposed a 50x60 μm^2 C8-coated chemiresistors to various electron beam doses. We configured the SEM to allow for noise testing without removing the chemiresistor for the SEM chamber. The chemiresistor was exposed at 30 kV and doses of 200, 400, 600, 800, 1100, 1400 and 2000 $\mu C/cm^2$. Low frequency measurements were performed after each exposure, and 1/*f*-type noise was observed at every exposure dose. As shown in Figure 2.10, a reduction in the noise prefactor was observed between exposure doses of 400 – 1100 $\mu C/cm^2$. In a previous study, an exposure dose of 500 $\mu C/cm^2$ was shown to sufficiently crosslink a C8 film and leave it insoluble to toluene[16]. While an improvement in the noise prefactor was seen at these doses, it was not significant enough to account for all of the noise in the system. As

previously reported[2], there must be several processes contributing to the noise in this system.

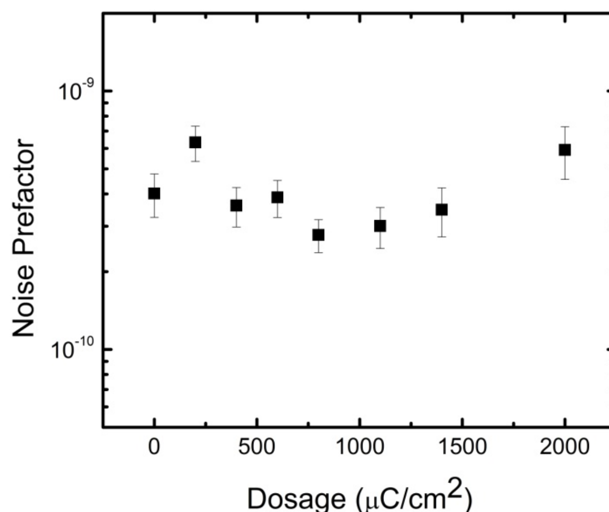

Figure 2.10 Change in noise prefactor as a function of the electron beam dosage of cross-linked sensors.

2.8 Conclusions

Lowering the noise amplitude of a chemiresistor is one way to improve its limit of detection. Chemiresistors have been shown to exhibit $1/f$ type noise that scales inversely with device volume indicating that the noise arises from intrinsic processes. Devices with the same volume can have noise amplitudes ranging multiple orders of magnitude, and the cause of this scatter was unknown. Variations in film thickness were explored as possible causes for large variations in noise amplitude.

By depositing thick nanoparticle films, rather than monolayer films, we were able to decrease the noise by five orders of magnitude. Although monolayer films were highly

uniform, their low noise prefactor made them preferable to uniform monolayer films. All chemiresistors coated has their resistance and noise prefactor lowered as more nanoparticles were added onto the interdigitated electrodes. Chemiresistors coated from different batches of nanoparticles solutions had variations in initial resistance in noise prefactor. It was hypothesized that solutions may have varying amounts of contaminants that could cause sample to sample variations in noise amplitude and resistance. This could be another factor in the large scatter in noise amplitude for devices of similar size.

We systematically contaminated 1-octanethiol solutions with the organic compound naphthalene to determine if contaminants could cause an increase in noise amplitude. Once again, a relationship between chemiresistor resistance and noise amplitude was observed. Highly resistive chemiresistors had the highest noise amplitude. Naphthalene coated samples were generally not found to have high noise amplitudes; therefore, other causes for large variations in noise amplitude, such as ionic contaminants, must be investigated.

We also explored electron beam induced crosslinking as a means to reduce the noise of chemiresistors by limiting the movement of nanoparticles by rigidly connecting them to neighboring nanoparticles through their ligands. A chemiresistor's noise properties were studied after subsequent electron beam exposure doses. The noise amplitude was found to be decreased for doses between 400 and 1100 $\mu C/cm^2$. While the noise amplitude was reduced for these doses, it was not significant enough to claim that $1/f$ type noise is caused solely by nanoparticle movement. As previously theorized, there are likely several contributing mechanisms to the intrinsic noise of chemiresistors. For

the case of MPN coated chemiresistors, the origins of 1/*f* type noise are still undetermined. A recent paper suggests electron interactions with atomic vibrations in the bulk gold[17] as a one possible cause of 1/*f* type noise.

2.9 References

1. IUPAC, *IUPAC. Compendium of Chemical Terminology "Gold Book"*. (Blackwell Scientific Publications, 2006).
2. C. Kurdak, J. Kim, A. Kuo, J. J. Lucido, L. A. Farina, X. Bai, M. P. Rowe and A. J. Matzger, Appl. Phys. Lett. **86** (7), 073506 (2005).
3. W. Kruppa, M. G. Ancona, R. W. Rendell, A. W. Snow, E. E. Foos and R. Bass, Appl. Phys. Lett. **88** (5) (2006).
4. J. B. Johnson, Phys. Rev. **32** (1), 97-109 (1928).
5. F. N. Hooge, T. G. M. Kleinpenning and L. K. J. Vandamme, Rep. Prog. Phys. **44** (5), 479-532 (1981).
6. P. Dutta and P. M. Horn, Reviews of Modern Physics **53** (3), 497-516 (1981).
7. F. N. Hooge, Phys. Lett. A **29 A** (3) (1969).
8. E. L. Covington, R. W. Turner, C. Kurdak, M. P. Rowe, X. Chao and E. T. Zellers, Proceedings of the IEEE Sensors Conference, 102-105 (2008).
9. L. Hubble, L. Wieczorek, K. Muller, E. Chow, J. Cooper and B. Raguse, 2010 International Conference on Nanoscience and Nanotechnology (ICONN), 37-40 (2010).
10. R. D. Deegan, O. Bakajin, T. F. Dupont, G. Huber, S. R. Nagel and T. A. Witten, Phys. Rev. E **62** (1), 756 (2000).
11. T. P. Bigioni, X.-M. Lin, T. T. Nguyen, E. I. Corwin, T. A. Witten and H. M. Jaeger, Nat. Mater. **5** (4), 265-270 (2006).
12. Ç. Kurdak, J. Kim, L. A. Farina, K. M. Lewis, X. Bai, M. P. Rowe and A. J. Matzger, Turk. J. Phys. **27**, 419-426 (2003).
13. M. Brust, M. Walker, D. Bethell, D. J. Schiffrin and R. Whyman, J. Chem. Soc.-Chem. Commun. (7), 801-802 (1994).
14. M. P. Rowe, K. E. Plass, K. Kim, Ç. Kurdak, E. T. Zellers and A. J. Matzger, Chem. Mat. **16** (18), 3513-3517 (2004).
15. M. H. V. Werts, M. Lambert, J. P. Bourgoin and M. Brust, Nano Letters **2** (1), 43-47 (2002).
16. W. H. Steinecker, K. Sun Kyu, F. I. Bohrer, L. Farina, C. Kurdak and E. T. Zellers, IEEE Sens. J. **11** (2), 469-480 (2011).

17. M. N. Mihaila, 21st International Conference on Noise and Fluctuations (ICNF), 61-64 (2011).

Chapter 3

Electron Beam Induced Crosslinking of Gold Thiolate Nanoparticles

3.1 Introduction

In Chapter 2, electron beam induced crosslinking was proposed as a possible way to reduce the noise of chemiresistors by linking the nanoparticle together by their ligands. In theory, crosslinking the nanoparticles will decrease their mobility and potentially reduce the noise of the sensor. While the noise properties of crosslinked MPN films were not heavily improved by crosslinking, there is another application for electron beam induced crosslinking. Crosslinking renders an MPN film insoluble; therefore, it can be used to pattern a chemiresistor array with different types of MPN films.

Electron beam induced crosslinking has a distinct advantage over other patterning methods in that it can produce tightly spaced chemiresistors with different MPN films. Electron beam induced crosslinking can be used to precisely expose discrete areas on an array with the accuracy of a SEM. Doing so, it is possible to selectively crosslink desired sensors on an array without exposing adjacent sensors to the electron beam. This is referred to as electron beam induced crosslink patterning. We used this technique to

pattern tightly spaced sensors with four different nanoparticle films resulting in the smallest chemiresistor array ever reported[1].

In order to determine the effects of crosslinking on the MPN films, we studied the properties of chemiresistors before and after electron beam exposure. The chemiresistor's resistance, along with its I-V characteristics, was studied after exposure to determine if crosslinking changes the electrical transport mechanism. An electron beam induced crosslink patterned film of octanethiol (C8) was exposed to determine the effect of crosslinking on vapor sensitivity. The responses to four vapors were also compared using statistical analysis to determine if crosslinking impairs the diversity of responses.

3.2 In-Situ measurements of Crosslinked films

3.2.1 Experimental Methods

As described in Chapter 2, a SEM was configured so that a chemiresistor could be electrically characterized without having to remove the sample from the chamber making it possible to measure the resistance and noise measurements of the chemiresistor in situ. A 50×60 μm^2 device with electrodes with width and spacing of 300 nm was coated with 1-octanethiol (C8) nanoparticles. The chemiresistor was exposed at 30 kV and measured after exposure doses of 200, 400, 600, 800, 1100, 1400 and 2000 $\mu C/cm^2$. The measurements were taken with a bias voltage of 200 mV and a current sensitive amplifier with a gain of 10^{-7} A/V.

3.2.2 Changes in Resistance

In a paper by Steinecker *et al.*, electron beam induced crosslinking was found to reduce the resistance of MPN-coated chemiresistors[2]. This was hypothesized to be caused be either an increase dielectric constant of the thiolate ligand layer, a decrease in the interparticle distance, or a decrease in the electron tunneling constant. Due to the size of the decrease in resistance (5-8 fold), an increase in dielectric constant was ruled an unlikely. For a C8 film, the dielectric constant would have to increase from 2.8 to > 40 to account for the decrease in resistance. Changes in the electron tunneling constant were also ruled out due to the magnitude of change need for the corresponding resistance decrease. It was therefore decided that the decrease in resistance was likely caused by a decrease in the interparticle distance. A 5-8 fold decrease in resistance corresponds to approximately a 10% decrease in interparticle distance.

Exposure to the electron beam source most likely causes a scission in the C─C and C─H bonds caused by secondary electrons generated in the substrate[3]. The radicals created are then able to form new bonds between ligands on neighboring nanoparticles. The doses used here (200-2000 μC/cm^2), are believed to be sufficient to crosslink the film without completely removing all of the C8 ligand[2]. A study by Lin et al. reported that a minimum dose of 7000 μC/cm^2 is needed to completely remove all of the ligand coating from 1-dodecanethiol (C12) gold nanoparticles[4].

The initial resistance, before any electron beam exposure, of the C8-coated chemiresistor we studied was 4.3 MΩ. After each exposure, the resistance of the chemiresistor decreased. Figure 3.1 shows the evolution of the resistance of the chemiresistor after repeated exposure to the electron beam. There was an 11 fold decrease

in resistance after a 2000 μC/cm^2 exposure dose. This decrease is most likely caused by a reduction in the distance between neighboring nanoparticles. Using Equations 1.24 and 1.25, an 11 fold decrease in resistance would correspond to an 11% decrease in MPN spacing.

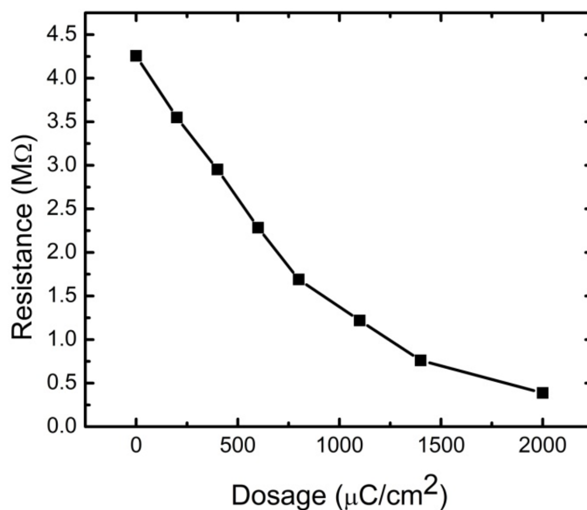

Figure 3.1 Decrease in resistance of a C8 coated sensor after repeated SEM exposure.

3.3 Effect of Crosslinking on Activation Energy

As shown in Figure 3.1, an electron beam dose of 2 mC/cm^2 was found to cause an 11 fold reduction in resistance. In a previous study in our research group, a C8 coated chemiresistor was measured after an even greater electron beam doses to determine the effects of high electron beam exposure[5]. The change in resistance for an electron beam dose up to 11 mC/cm^2 is shown in Figure 3.2. Like the previous chemiresistor, the resistance decreases with increasing electron beam exposure. For a dose of 11 mC/cm^2, the chemiresistor experiences a nearly 50 fold decrease in resistance. This magnitude of

the resistance change is consistent with the expectation that crosslinking will causes a decrease in interparticle distance due to the removal of ligands. Even at such a large exposure, the change in MPN spacing isn't significant. A 50 fold decrease in resistance would correspond to less than a 20% decrease in MPN spacing.

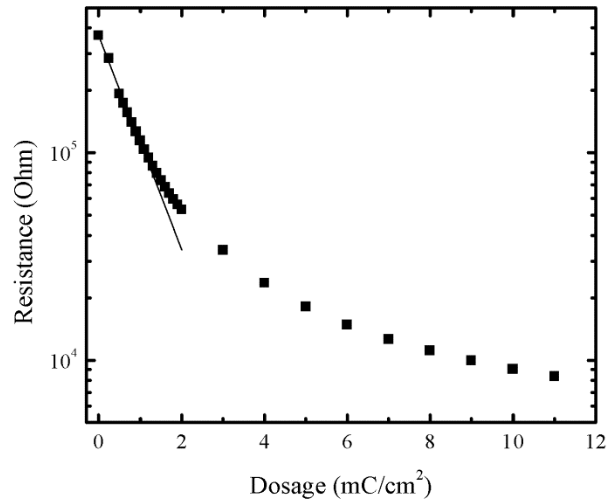

Figure 3.2 A C8 coated chemiresistor's resistance decreases with increasing electron beam exposure leading to a nearly two order of magnitude decrease.

In addition to resistance measurements, the I-V characteristics were measured before and after electron beam exposure. From these measurements, the activation energy was extracted and is shown for the chemiresistor before exposure and after a dose of 11 mC/cm^2 in Figure 3.3. After the large exposure dose, there was a decrease in the activation energy indicating an increase in the capacitance. According to Equation 1.23, this increase in capacitance would be consistent with a reduction in the interparticle distance. A decrease from 37.1 meV to 8.1 meV corresponds to a factor of 10 decrease in MPN spacing. An increase in capacitance could also be caused by an increase in the

radius of the gold nanoparticle core. Since an electron beam of exposure of 7 mC/cm^2 was shown to remove all ligands from a C12 particle[4], it is possible that at this dose the nanoparticle could coalescence from the loss of ligand coating. Assuming a constant MPN spacing of 1.75 nm[2, 6], the MPN radius would change from 2.7 nm to 6.6 nm. Using Equation 1.25, this would correspond to only a factor on 3 decrease in the resistance; therefore, an increase in the size of the MPN radius cannot be attributed to the large decrease in resistance and activation and energy. Transmission electron microscope scans of electron beam irradiated films by Werts *et al*. and Lin *et al*. confirmed that gold particle cores remain intact and do not sinter[3, 4].

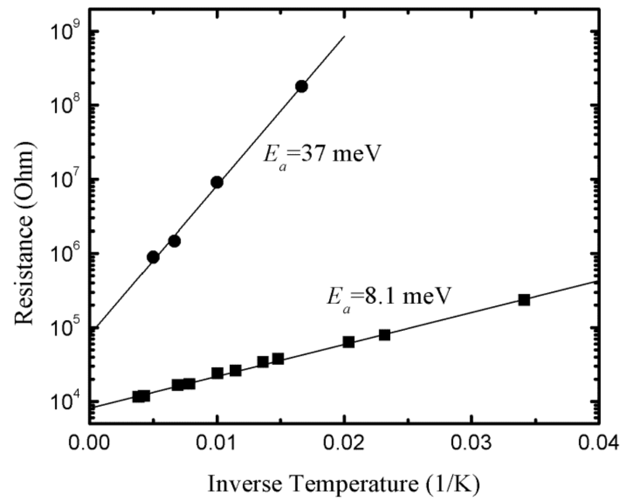

Figure 3.3 The activation energy before and after an electron beam exposure of 11 mC/cm^2. The large exposure dose leads to a decrease in activation energy consistent with a reduction in the average distance between nanoparticles.

3.4 Electron-beam Induced Crosslinking for Array Patterning

For electron beam induced crosslink patterning, incident electrons with sufficiently high energy (30 keV) were used to break the chemical bonds within the thiolate ligands, permitting the formation of new bonds between the ligand fragments on neighboring nanoparticles[3]. An electron beam dose of 600 $\mu C/cm^2$ was used on the basis of previous studies showing that this was sufficient to render films of several MPNs insoluble [2] and reduce the noise in the films[7]. By restricting the region of the array that is exposed, only the desired areas on an area can be patterned with a nanoparticle film.

Using this technique, Werts *et al.* was able to pattern 40 nm wide lines of *n*-hexanethiol (C6) films[3]. This was done on Langmuir-Blodgett deposited films of monolayers and tri-layers. The C6 films were exposed to electron beam doses ranging from 0.8 mC/cm^2 to 6 mC/cm^2. Underexposure (0.8 mC/cm^2) of the films led to a reduced films thickness and discontinuities in the pattern. Over exposure (6 mC/cm^2) led to broadening of the patterned caused by the backscattering of electrons through the substrate. The dose needed to create a film thickness equal to the original film was found to be dependent on the alkanethiol length and the electron beam accelerating voltage.

In contrast to the study by Werts *et al.*, where their goal was to create nanometer scale structures, our goal was to pattern thick films of MPNs on nanometer scale IDEs. In their study, electrodes were fabricated on top of their "nanowires" after electron beam patterning. Using this technique, we desired to pattern an array of chemiresistors with MPN films so every chemiresistor in the array would have a different MPN film coating.

Since they were able to achieve a resolution of 50 nm, we were optimistic that we would be able to pattern films with a 4 μm spacing between IDEs.

3.4.1 Chemiresistor Fabrication

Interdigitated electrodes were defined by electron-beam lithography and were made by a liftoff process from evaporated films of Au (200 Å) and Ti (20 Å, for adhesion) on a Si substrate with a thermally-grown oxide layer. Each chemiresistor is comprised of 20 pairs of IDEs with width and spacing of 100 nm and occupies an active area of $10\times10\ \mu m^2$. The sensors are arranged in a 2×2 array with 4 μm spacing between adjacent IDEs. An electron micrograph of the array is shown in Figure 3.4.

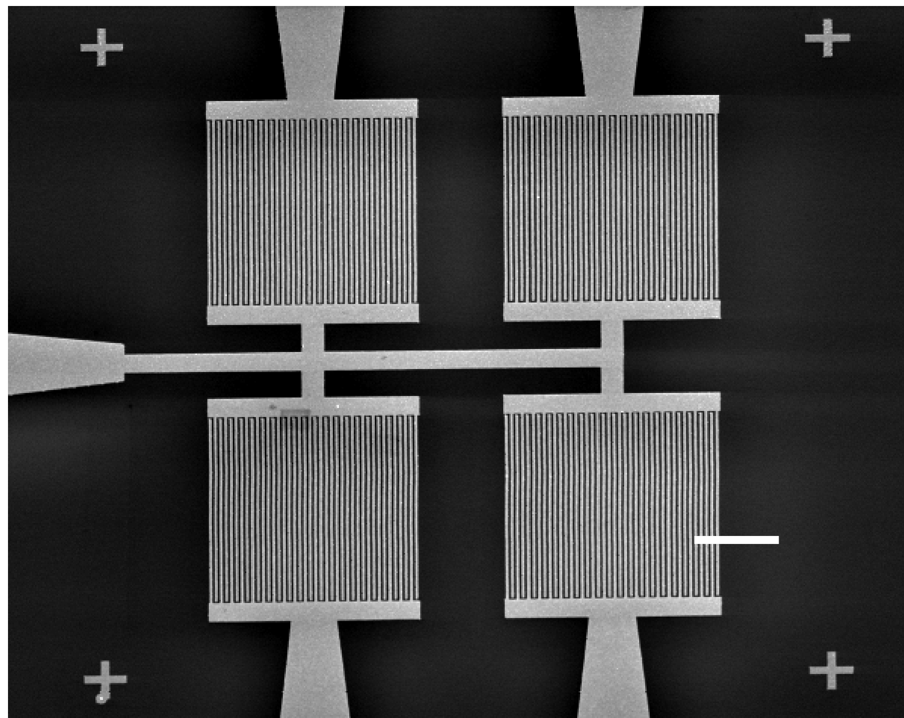

Figure 3.4 SEM image of an array with four chemiresistors with 20 pairs of interdigitated electrodes with 100 nm width and spacing. Adjacent chemiresistors are spaced by 4 μm. The scale bar indicates 5 μm.

3.4.2 Film Deposition

Nanoparticles with average Au core diameters ranging from 3.9-4.5 nm were synthesized in the Zellers lab using the method of Rowe *et al.*[8] with thiolate ligands derived from either 1-octanethiol (C8), 1-mercapto-6-phenoxyhexane (OPH), 7-hydroxy-7,7-bis(trifluoromethyl)-heptane-1-thiol (HFA) or mercapto-diphenylacetylene (DPA). All nanoparticles were dissolved in toluene except HFA which was dissolved in acetone.

A micro-dispensing system (Jetlab 4, Microfab, Plano, TX) was used to deposit the MPNs from solution. The tight spacing between devices precluded the use of more conventional spray-coating or solvent casting methods. Even with this deposition system, the minimum size of the dried film is in the range of 100-200 μm in diameter and sensors would need to be spaced roughly 100 μm apart to ensure that each sensor had a different film type. The resulting films are also highly non-uniform. As previously discussed, a coffee stain pattern is formed where the majority of the nanoparticles settle in a thick ring, leaving the interior with a significantly thinner film[9]. In Chapter 2, it was shown that thicker MPN films have lower noise which makes them more desirable for use as a sensor[10]. To account for this we aim the edge of the coffee stain, the thickest portion of the film, directly on top of the desired IDE. An example of this is shown in Figure 3.5.

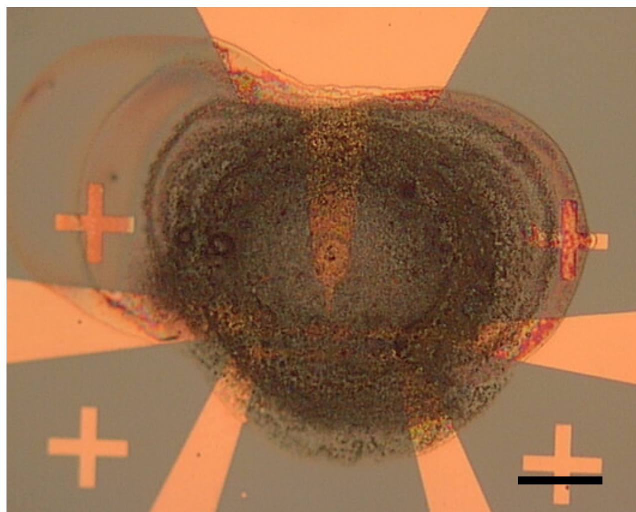

Figure 3.5 Optical image of a four sensor array with a micro-dispensed nanoparticle film covering all IDEs. The thickest portion of the film, the coffee ring, is placed directly over the IDEs to ensure the thickest possible film coating. The scale bar indicated 50 μm.

3.4.3 Mono-MPN array Patterning

If desired, all of the chemiresistors on an array can be crosslinked with the same MPN film creating a mono-MPN array. This could be useful in limiting the sensing material to only active area of the chemiresistors. Figure 3.6 shows an array before and after the patterning process. In this array, we patterned all the IDEs with an OPH nanoparticle film. The 4 μm gap between the chemiresistors is unpatterned and can easily be seen. The gold crosses seen in the image are alignment markers. Before the exposure, the electron beam is aligned through a series of alignment marks on the substrate. This prevents the film from being exposed during the SEM set-up procedure.

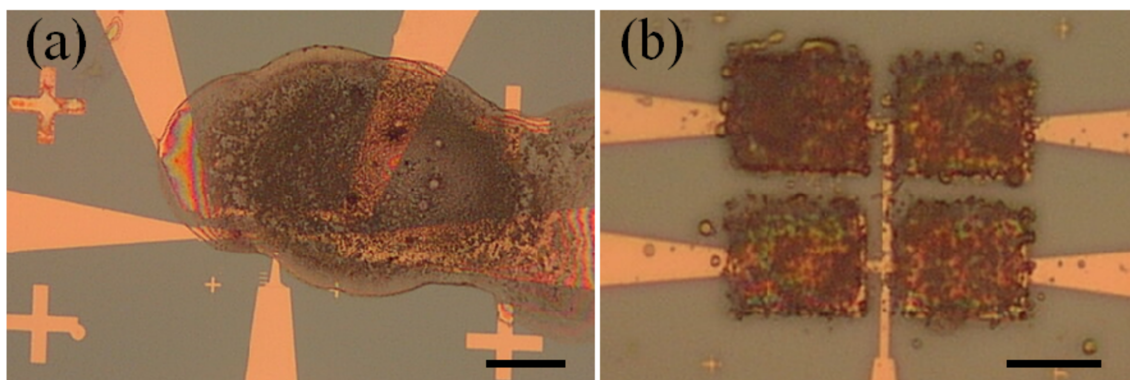

Figure 3.6 (a) Optical image of an array covered with an OPH nanoparticle film. Scale bar indicated 50 μm. (b) After electron beam exposure, the array was rinsed with toluene leaving only the active areas of the array patterned with the OPH nanoparticle film.

Since the films deposited by the micro-dispensing system are non-uniform, the resulting patterned film is also non-uniform. We performed an atomic force microscopy (AFM) scan on another array with all sensors coated with an OPH film. The array and resulting AFM scan can be seen in Figure 3.7. Analysis of the AFM scan revealed an average thickness of 244 nm and a standard deviation of 130 nm.

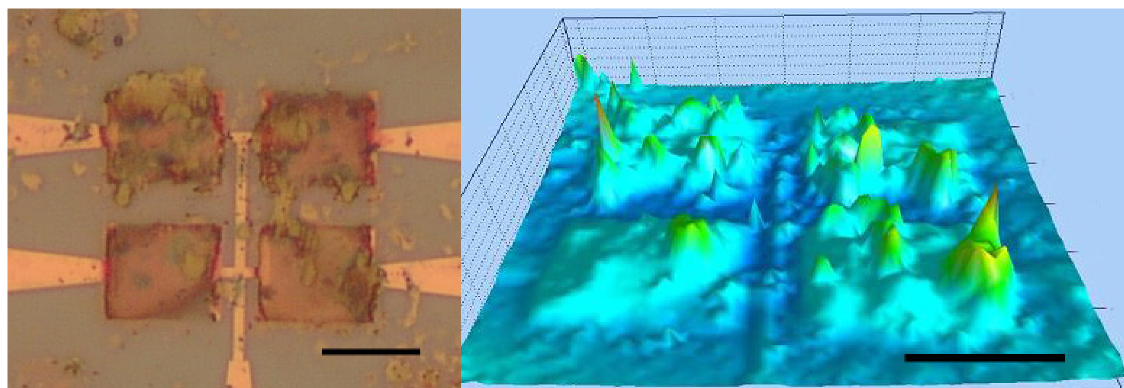

Figure 3.7 (left) Optical image of a crosslinked OPH nanoparticle array. (right) AFM image of the same array. The average film thickness if 244 nm. Scale bars in both images indicate 10 μm.

3.4.4 Multi-MPN Array

In addition to coating an array with identical films, electron beam induced crosslink patterning can also be used to pattern an array with different nanoparticle films. This is done with a multi-step coating, exposure and rising process. An example of this process is shown in Figure 3.8. Initially, we coated the array with a C8 film that covered all IDEs on the array. We then exposed only the top left IDEs to an electron beam dose 600 $\mu C/cm^2$ and subsequently rinsed with toluene. After the toluene rinse, only the exposed sensor is left coated with a C8 film, as shown in Figure 3.8(a). We then coated the array with an OPH film. The top right sensor was solely exposed then rinsed with toluene. Figure 3.8(b) shows the array with the two patterned IDEs. We then coated the array with an HFA film, and the bottom left IDEs were exposed and solvent rinsed as shown in Figure 3.8(c). Finally, the array was coated with a DPA film, and the bottom right IDEs were patterned and solvent rinsed. The resulting fully patterned array can be seen in 3.8(d).

This process does have the drawback of being time prohibitive. Each desired film coating requires its own coating and exposure procedure. While this process is not as fast and syringe or spray coating, unlike these methods, it allows for the patterning of tightly spaced IDEs. There is also room for possible cross contamination of the nanoparticle films. As seen in Figure 3.8(b), some OPH residue is left on the bottom right sensor after the solvent rinse. Cross contamination could be caused by accidental electron beam exposure on undesired IDEs or misalignment during the SEM set-up. The resulting films are also highly non-uniform. For the multicoated array, the film thicknesses were

measured by AFM and were: 1.96 μm for C8, 549.20 nm for OPH, 613.83 nm for DPA, and 175.54 nm for HFA. Even with these potential disadvantages, electron beam induced crosslink patterning is a highly effective method for patterning closely spaced sensors with different MPN films.

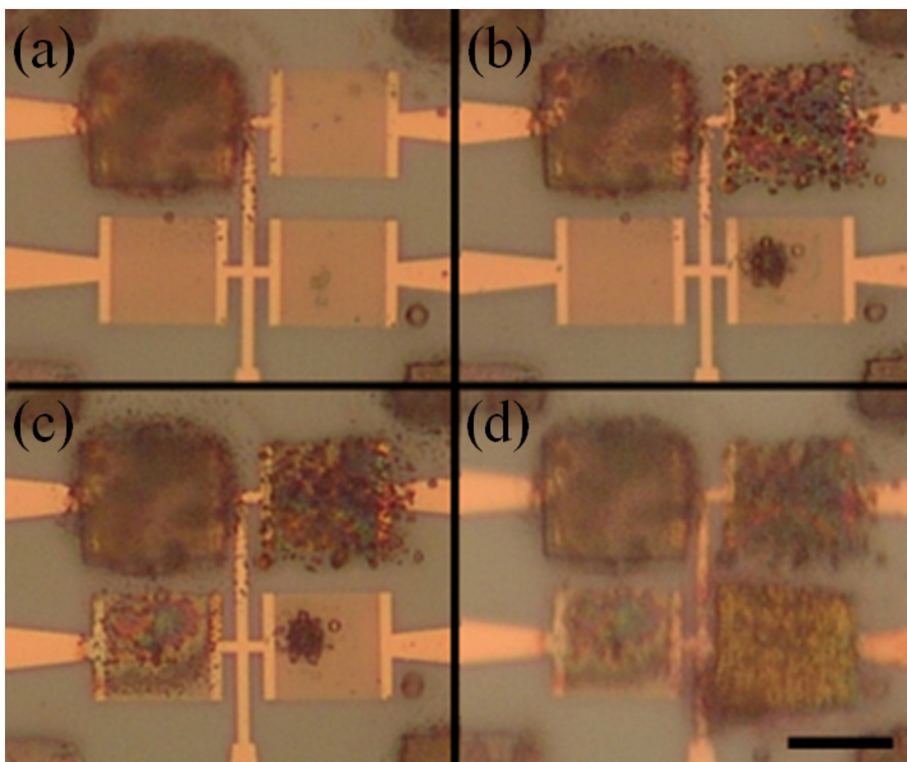

Figure 3.8 Optical images of a chemiresistor array at different stages in the crosslink patterning process. (a) The top left IDEs are exposed to 600 μC/cm^2 of electron-beam radiation. The array was rinsed with toluene leaving the irradiated sensor coated with a patterned C8 film. (b) The top right IDEs were patterned with an OPH film. (c) The bottom left IDEs were patterned with an HFA film. (d) The bottom right IDEs were patterned with a DPA film. Since the alignment marks at the periphery of the image are also repeatedly exposed during beam alignment, they are also coated. The scale bar indicates 10 μm.

3.5 Vapor Testing of Crosslinked Films

The chemiresistor sensitivities were determined for vapors of 2-butanone, toluene, *n*-propanol, and *n*-octane to which the array was exposed individually at discrete concentrations over a 10-20 fold range (between 0.8 and 26% of saturation). For these tests, the array was mounted in a 0.5-L chamber maintained at 25.0 ± 0.1 °C and test atmospheres were generated by passing scrubbed, dry air through a fritted bubbler containing the liquid solvent and diluting with metered dry air. Exposure at a given concentration for five minutes was followed by purging with air for a similar time period. An example of a response to a vapor exposure is shown in Figure 3.9. Vapor concentrations were verified by passing aliquots to a calibrated flame ionization detector.

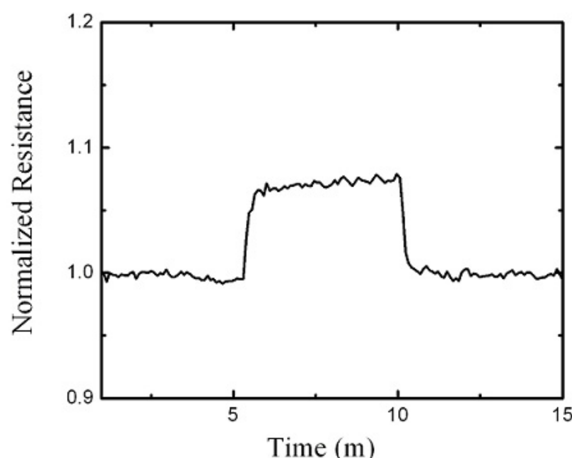

Figure 3.9 The normalized change in resistance of the HFA coated chemiresistor while being exposed to 3100 ppm of toluene.

Sensor outputs were measured by recording the ac current using a lock-in amplifier and then converting the signal to resistance. Baseline resistances, R_b, ranged from 10 to 200 MΩ. All chemiresistors exhibited reversible responses to the vapors, with

time constants typically < 6 sec, consistent with those reported for unpatterned films[2, 11, 12]. Plots of $\Delta R/R_b$ versus concentration (mg/m^3) are linear (forced-zero linear regression r^2 values are ≥ 0.98 with the exception of 2-butanone with OPH, for which one of the responses at a mid-range concentration deviated from linearity to an extent sufficient to reduce the r^2 value to 0.95). Figure 3.10 shows a representative subset of calibration curves for *n*-propanol. The sensitivities were taken as the slopes of the calibration curves and are presented in Figure 3.11 as a set of bar charts for each vapor. Values for C8 and OPH are very similar to those reported for larger chemiresistors with unpatterned C8 and OPH films[2].

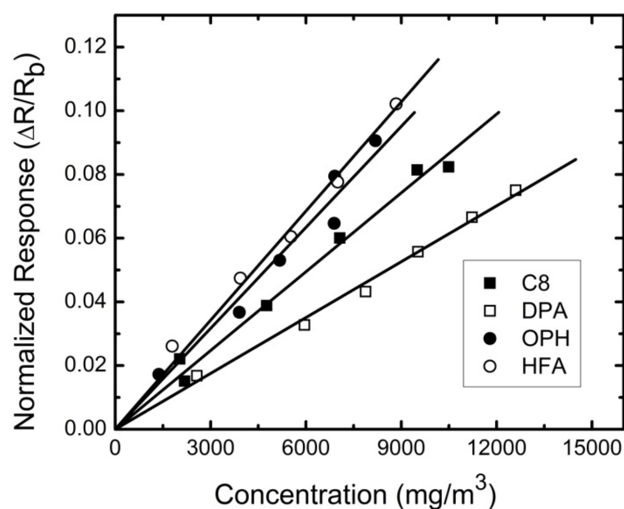

Figure 3.10 Calibration curves for *n*-propanol.

The magnitude of the response of an MPN-coated chemiresistor typically is strongly affected by the amount of vapor that partitions into the MPN film at a given vapor concentration[12]. Accordingly, the sensitivities to 2-butanone are lower than those to *n*-propanol because the former is more volatile (i.e., the vapor pressure of 2-butanone is

95 torr and that of *n*-propanol is 21 torr). Functional-group interactions between the vapors and the thiolate tail groups will also affect sensitivities, and it is these interactions that largely govern the differences in the collective pattern of responses used for vapor discrimination with an array. It is clear from visual inspection of the data in Figure 3.11 that the array response patterns for these two vapors are quite distinct, and that they could be discriminated from each other on the basis of their patterns to an extent similar to that reported for other MPN-coated chemiresistor arrays[2, 13-15]. The sensors also exhibit a preferential sensitivity toward *n*-propanol which could be explained by the crosslinking process rendering the films more polar. This is also supported by the similarity in response of C8 and OPH to 2-butanone and octane.

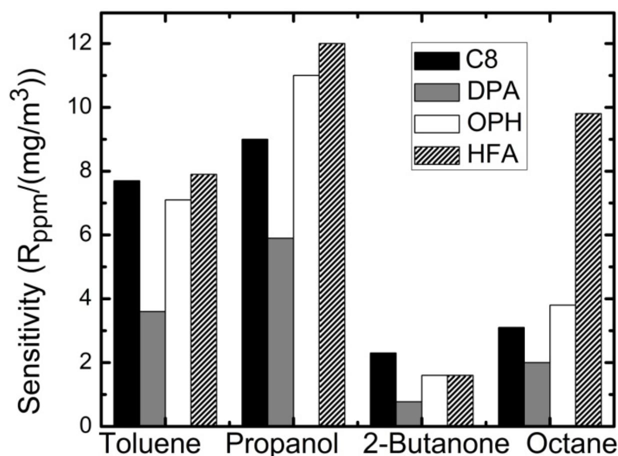

Figure 3.11 Sensitivities ($R_{ppm}/mg\cdot m^{-3}$) of the array sensors for the four test vapors ($R_{ppm} = \Delta R/R_b \times 10^6$).

Linear discriminant analyses (LDA) and extended disjoint principal component regression (EDPCR) were performed by Dr. Forest Bohrer to determine if crosslinking decreased the diversity of responses[11]. Monte Carlo simulations (500 iterations) were

used to generate error-enhanced responses. The statistical methods used are detailed in previous studies[16, 17]. The following relative errors were superimposed on responses from experimental sensitivities: 7.4%, 5.8%, 5.8%, and 4.4% for C8, DPA, OPH, and HFA, respectively. Each simulated response vector was projected onto the plane created from the first and second linear discriminant, shown in Figure 3.12, shows good separation of the response vectors.

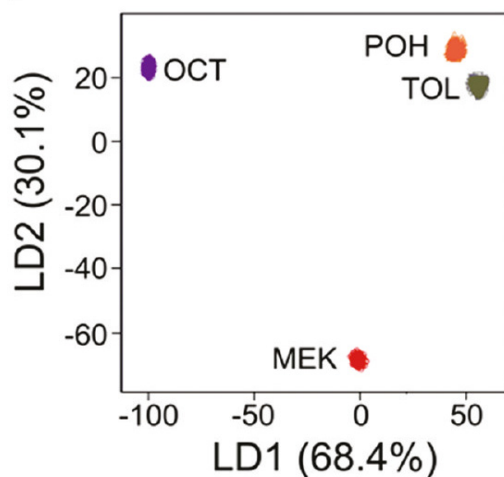

Figure 3.12 LDA plot from multiple-MPN array of data generated by Monte Carlo simulations (500 iterations per vapor) with the following relative errors superimposed on responses from experimental sensitivities: 7.4%, 5.8%, 5.8%, and 4.4% for C8, DPA, OPH, and HFA, respectively. The vapors are *n*-octane (OCT), *n*-propanol (OPH), toluene (TOL) and 2-butanone (MEK).

EDPCR was used to generate statistical estimates of recognition rates for the individual vapors and then for all possible binary mixtures. EDPCR analysis gives an average recognition rate of 96% for individual vapor discriminations and 83% for binary mixture

discriminations (range 58 − 98%). Thus, despite crosslinked induced effects on the films, the expected performance is comparable to that of unpatterned films[11].

3.6 Conclusions

We studied the effects of electron beam induced crosslinking on MPN-coated chemiresistors. Electron beam exposure lowers the resistance of the chemiresistor which is consistent with nanoparticles moving closer together. This is caused by loss of ligand through the crosslinking process which will shorten the ligand monolayer and decrease the distance between neighboring nanoparticles. Current-voltage measurements performed before and after crosslinking show a decrease in activation energy which further supports the notion that the interparticle distance is decreasing.

We successfully patterned an array of MPN-coated chemiresistors occupying an area of just 600 μm^2 by use of sequential electron beam crosslink induced patterning of the nanoparticle films. This is the smallest chemiresistor vapor sensor array yet reported. It was demonstrated that the sensors in this array respond rapidly and reversibly and provide differential sensitivities comparable to those from larger chemiresistors with unpatterned MPNs of similar structure. These results bode well for the ultimate use of such chemiresistor arrays as detectors in μGCs for complex mixture analyses. If properly configured, these small arrays will require very small samples of vapors for detection which, in turn, will permit miniaturization of upstream μGC components (e.g., preconcentrators and separation columns).

3.7 References

1. E. Covington, F. I. Bohrer, C. Xu, E. T. Zellers and C. Kurdak, Lab Chip **10** (22), 3058-3060 (2010).
2. W. H. Steinecker, K. Sun Kyu, F. I. Bohrer, L. Farina, C. Kurdak and E. T. Zellers, IEEE Sens. J. **11** (2), 469-480 (2011).
3. M. H. V. Werts, M. Lambert, J.-P. Bourgoin and M. Brust, Nano Lett. **2** (1), 43-47 (2001).
4. X. Lin, Appl. Phys. Lett. **78** (13), 1915 (2001).
5. H. Wu and Ç. Kurdak, unpublished.
6. F. I. Bohrer, E. Covington, C. Kurdak and E. T. Zellers, Solid-State Sensors, Actuators and Microsystems Conference, 148-151 (2009).
7. E. L. Covington, R. W. Turner, C. Kurdak, M. P. Rowe, X. Chao and E. T. Zellers, Proceedings of the IEEE Sensors Conference, 102-105 (2008).
8. M. P. Rowe, K. E. Plass, K. Kim, Ç. Kurdak, E. T. Zellers and A. J. Matzger, Chem. Mat. **16** (18), 3513-3517 (2004).
9. R. D. Deegan, O. Bakajin, T. F. Dupont, G. Huber, S. R. Nagel and T. A. Witten, Phys. Rev. E **62** (1), 756 (2000).
10. E. L. Covington, R. W. Turner, C. Kurdak, M. P. Rowe, X. Chao and E. T. Zellers, Proceedings of the IEEE Sensors Conference, 102-105, (2008).
11. F. I. Bohrer, E. Covington, C. Kurdak and E. T. Zellers, Anal. Chem. **83** (10), 3687-3695 (2011).
12. W. H. Steinecker, M. P. Rowe and E. T. Zellers, Anal. Chem. **79** (13), 4977-4986 (2007).
13. C.-J. Lu, W. H. Steinecker, W.-C. Tian, M. C. Oborny, J. M. Nichols, M. Agah, J. A. Potkay, H. K. L. Chan, J. Driscoll, R. D. Sacks, K. D. Wise, S. W. Pang and E. T. Zellers, Lab Chip **5** (10), 1123-1131 (2005).
14. C. Jin and E. T. Zellers, Sens and Actuat. B-Chem. **139** (2), 548-556 (2009).
15. Q.-Y. Cai and E. T. Zellers, Anal. Chem. **74** (14), 3533-3539 (2002).
16. E. T. Zellers, J. Park, T. Hsu and W. A. Groves, Anal. Chem. **70** (19), 4191-4201 (1998).
17. M.-D. Hsieh and E. T. Zellers, Anal. Chem. **76** (7), 1885-1895 (2004).

Chapter 4

Stability of Gold Nanoparticle Films

4.1 Introduction

Chemiresistors with thiolated gold nanoparticle films have been studied for extended periods to determine their long term stability. Chemiresistors experience changes in baseline drift, which has been hypothesized to be caused by degradation of the gold nanoparticle core or alkanethiol coating. Previous studies have shown alkanethiols are susceptible to oxidation[1-4]. Oxidation of the sulfur bond has shown to oxidize within hours of exposure to ambient air[3]. A recent study claims that oxidation of the thiol bond leads to a loss of the ligand coating and subsequently causes coalescence of nanoparticles[1].

We studied chemiresistors over extended periods to observe their changes in baseline resistance and sensitivity to toluene vapor. Unlike previous MPN films stability studies[1], we continuously monitored the baseline resistance of arrays of chemiresistors. While integrated into μGC system, chemiresistors may need to be heated to increase the movement of low volatility compounds through the system. In order to determine if elevated temperatures expedited the aging process, we also continuously monitored the

resistance of chemiresistor arrays at different temperatures. Low temperature I-V measurements were also performed to determine changes in the size of the gold nanoparticle cores. We also crosslinked the MPN films on chemiresistors to potentially prevent loss of ligand and hopefully increase the long term stability of their baseline resistance and vapor sensitivity. We also studied the effects of impurities in an MPN film on vapor sensitivity.

4.2 Experimental Methods

4.2.1 Sensor Fabrication

In this study, most sensor arrays consisted of interdigitated electrodes organized in a 4x2 array patterned onto thermally grown SiO_2 layers over Si substrates by standard photolithography and lift-off processing. Individual sensors were made of 24 pairs of 0.5 mm long electrodes spaced by 5 μm. The electrodes were deposited by sputtering 400 nm of gold over a 40 nm chrome adhesion layer. Sensors were mounted onto a 16 pin DIP header with indium solder then coated with nanoparticle solutions via syringe deposition. Sensors of this type are referred to as standard sensors. We also fabricated smaller chemiresistors by electron beam lithography. These sensors have an active area of 100×140 μm^2 and 116 pairs of interdigitated electrodes with 0.3 μm electrode width and spacing. The nanoparticles used in the study were 1-octanethiol (C8), 1-mercapto-6-phenoxyhexane (OPH), 4-mercapto-diphenyl-acetylene (DPA), and 7-hydroxy-7,7-bis(trifluoromethyl)-heptane-1-thiol (HFA) and were synthesize by a single phase synthesis method in the Zellers lab [5].

4.2.2 Vapor Testing System

In order to simultaneously monitor the resistance of all sensors on an array, we made a system that could enclose an array for vapor testing and heating studies. Sensors were mounted into a metal block with a small outlet for wires used to interface with a HP Multiplexer. A solid metal cap, with a small recess volume for the array, was used to cover the mounted array for temperature studies to ensure uniform temperature in the sensor chamber.

For vapor testing, a nitrogen cylinder and a cylinder containing 200 pm toluene in air was connected with flow meters that were connected to a three way valve to control the direction of flow. The sensor chamber was fitted with a metal lid with a small inlet for the incoming vapor. This enclosure was not air tight to allow incoming nitrogen or toluene to flow out.

4.3 Low Temperature Measurements

It has been observed that the resistance of gold nanoparticle chemiresistors can change drastically over time, and the cause of these changes has not been determined. The changes in the resistance of the films and their sensitivities to vapors could be caused by changes in the gold nanoparticle cores, changes in the thiol coating, or exposure to environmental disruptors, such as UV light or ozone. While determining the cause of some of these factors could prove to be difficult, determining the integrity of the gold

nanoparticle cores can be done by measuring the activation energy through low temperature current-voltage (I-V) measurements.

4.3.1 Change Activation Energy

Because electron transport through the film is by tunneling, it is highly sensitive to charging effects of the nanoparticles. The charging energy, E_C, between nanoparticles is defined as,

$$E_C = e^2/2\text{c} \tag{4.1}$$

where e is the electron charge and C is capacitance of the tunnel junction. The main contributor of the capacitance is the self-capacitance of the nanoparticle,

$$C = 4\pi\varepsilon\varepsilon_0/(\frac{1}{r} - \frac{1}{r+\delta}) \tag{4.2}$$

where ε is the dielectric constant of the surrounding material and d is the diameter of the nanoparticle. When the charging energy is larger than thermal fluctuations, k_BT, where k_B is the Boltzmann constant, tunneling cannot occur. As the diameter of the nanoparticle decreases, the charging energy can exceed the thermal energy causing Coulomb blockade at low temperatures.

By taking temperature dependent I-V measurements, the charging energy can be determined by plotting resistance versus temperature in an Arrhenius plot. When fitted to an exponential line, the slope corresponds to the activation energy. By performing these measurements at different stages in the sensor's life, the change in the size of the gold

nanoparticle core can be calculated. A change in the nanoparticle size would indicate that the changes in the nanoparticles films properties could be due the gold nanoparticle core degrading over time or coalescing due to loss of ligand.

4.3.2 Low temperature IV measurements

We fabricated a 100×140 μm^2 chemiresistor with 116 pairs of interdigitated electrodes with 0.3 μm width and spacing via electron beam lithography. The electrodes where then coated with a 5.5 mg/mL C8 MPN in toluene solution by a Microfab Jetlab 4 micro-dispensing system. Because of the evaporation of toluene from the film, the resistance of the chemiresistor changes frequently directly after coating. The chemiresistor's resistance was allowed to stabilize for three days before being measured to be 0.8 MΩ. At this time, it was mounted in a variable temperature cryostat. The sample was allowed to warm to room temperature from 1.5 K while the voltage was repeatedly swept from -2 V to 2 V and the current was constantly recorded. The I-V curves for temperatures 10, 100, 175 and 292 K are shown in Figure 4.1(top), and non-linear I-V characteristics are clearly visible at low temperatures. The insert shows the resistance versus inverse temperature with an exponential fit of the Arrhenius equation. From this, the activation energy was found to be 20.8 meV.

After warming to room temperature, the chemiresistor was stored for 90 days in a static-control box. Over this time, the resistance dropped from 0.8 MΩ to 18.4 KΩ. The chemiresistor was again mounted in a variable temperature cryostat and cooled to 1.5 K

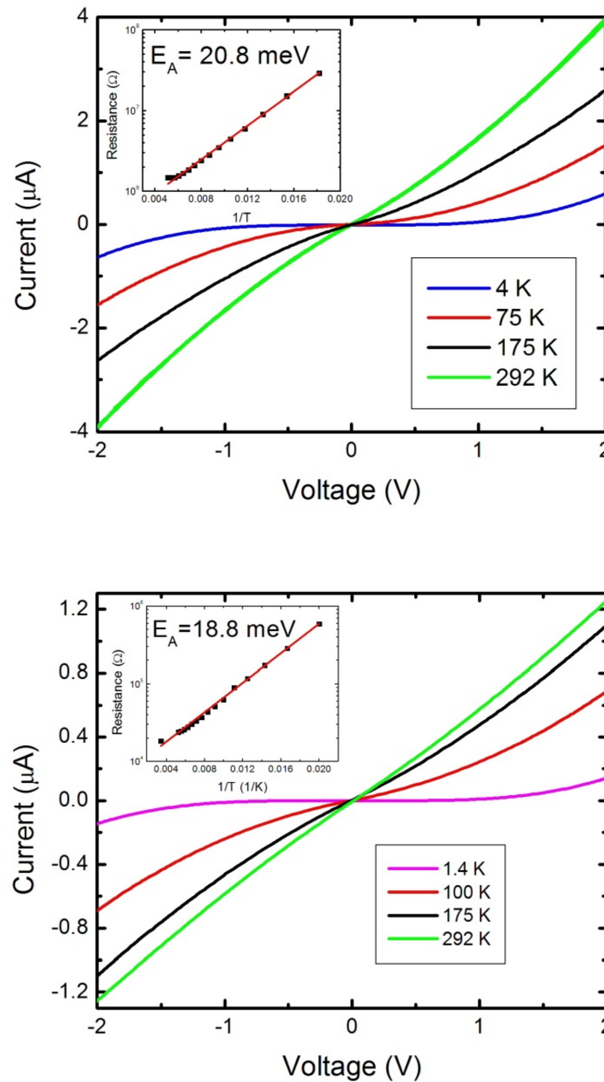

Figure 4.1 (top) Temperature dependent IV measurements taken on day three after coating the interdigitated electrodes. The insert shows the corresponding Arrhenius plot where the activation energy was found to be 20.8 meV. (bottom) Temperature dependent IV measurements taken on day 93. The insert shows the corresponding Arrhenius plot where the activation energy was found to be 18.8 meV.

and allowed to warm to room temperature. The voltage was also swept from -2 V to 2 V while continually measuring the current. The I-V curves for temperatures 1.4, 100, 175 and 292 K are shown in Figure 4.1(bottom). The activation energy was calculated to be 18.8 meV. In Figure 4.2, the Arrhenius plots for both day three and 93 are plotted together. While the resistance of the chemiresistor decreased by a factor of 43 over the 90 day period, the activation energy decreased by less than 10%. If the change in activation energy was caused by a change in the spacing between MPNs, we can use Equation 1.18 to determine the magnitude of this change. For C8 MPNs, the distance between neighboring nanoparticles has been estimated to be 17.6 Å[6, 7]. While the magnitude of the tunneling barrier for C8 MPNs is unknown, we can estimate its magnitude to be on the order of 2 eV. At this value, the corresponding κ will be 7.3×10^{9}. For a factor of 43 change in resistance, the corresponding change in interparticle distance can be found using

$$e^{-2\kappa\Delta\delta} = \frac{1}{43}. \tag{4.3}$$

Using the κ value calculated above, Δδ is 2.6 Å. This corresponds to an approximately 15% decrease in the spacing between MPNs. The drastic change in resistance is not caused by degradation or agglomeration of the gold nanoparticle cores and can most likely be contributed changes in the ligand coating.

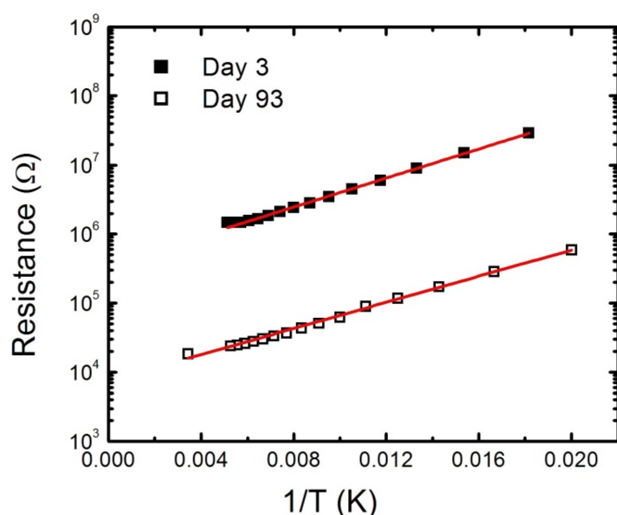

Figure 4.2 Arrhenius plots for the sensor at day 3 and 93. While the resistance changed from 0.8 MΩ to 18.4 kΩ, the activation energy only changed from 20.8 meV to 18.8 meV indicating that change in resistance is not due to decay in the gold nanoparticle core.

4.4 Baseline Resistance Drift

We continuously monitored the baseline resistance of several chemiresistor arrays at room temperature. Some arrays were also measured at elevated temperatures to determine if temperature increases the rate of drift. Typically, the resistance of a sensor would decrease over time, but some were shown to increase, especially at elevated temperatures. Usually, the rate of drift is found to be the greatest in the days following the MPN film coating. After this break in period, the baseline resistance drift rate will slow over time.

In addition to stability in baseline resistance, it is important to determine stability in the sensing ability of the chemiresistors. Since it may be necessary to heat sensors when integrated into a μGC system, it is necessary to determine the stability of the

sensitivity at room temperature and elevated temperatures. Sensitivity is defined as the normalized change in resistance, $\Delta R/R_b$, where R_b is the baseline resistance, divided by the vapor concentration, C. Sensitivity will be defined here using vapor concentration in parts per million, C_{ppm}.

$$Sensitivity = \left({}^{\Delta R}/_{R_b}\right)/C_{ppm} \tag{4.4}$$

A typical resistance trace during a vapor exposure is shown in Figure 4.3. Each exposure is repeated to determine reproducibility. In between exposures, the chamber is purged with nitrogen to expedite the reversal to R_b. Each exposure is held for 300 seconds and spaced with at least a 300 second nitrogen purge.

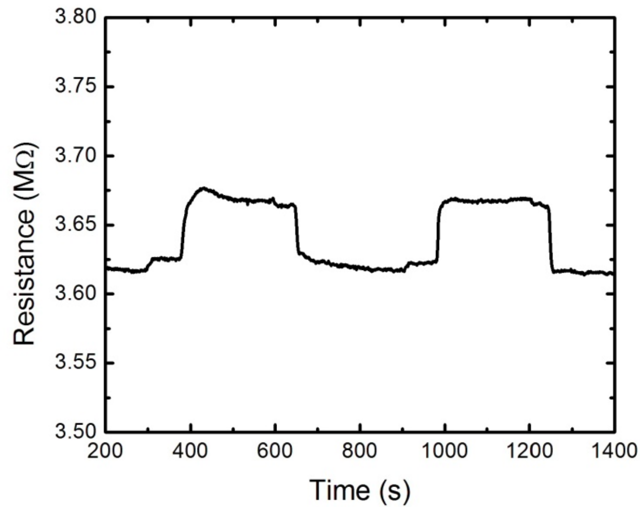

Figure 4.3 Change in resistance of a C8 coated sensor array after to exposures to 200 ppm of toluene vapor for 300 seconds. The exposure is repeated to determine reproducibility.

4.4.2 Decline in Drift Rate

We coated an OPH film on a standard array. The sensor's baseline resistance was measured three times over a twenty day period. Over this time period, the average percent change in resistance was -73% which corresponds to an average three fold decrease. Table 4.1 shows the change in baseline resistance over the twenty day period. The rate of change is greatest in the first few days after coating. This is most likely caused by changes within the nanoparticle film due to the gradual evaporation of solvent from the coating process. After this break in period, the rate of change in resistance slows as the resistance decreases. Although the baseline resistance of the sensors varied by nearly a factor of four, the percent change in resistance was similar for all sensors on the array. This indicates that the cause of the baseline drift is not distinct for an individual sensor on an array.

Sensor	**Resistance (MΩ) Day 1**	**Resistance (MΩ) Day 4**	**Resistance (MΩ) Day 20**	**Total Percent Change**
1	1.41	0.45	0.32	-77
2	1.36	0.56	0.41	-70
3	2.79	0.82	0.59	-79
4	1.36	0.55	0.39	-71
5	0.92	0.36	0.26	-72
6	0.81	0.30	0.22	-73
7	0.76	0.31	0.24	-68
8	1.18	0.46	0.34	-71

Table 4.1 The resistance for sensors on a standard array B on Day 1, 4 and 20. The total percent change over the 20 days is also shown. Although their initial resistance values vary greatly, the rate of change between sensors is comparable.

4.4.3 Stability at Elevated Temperatures

In order to determine the stability at elevated temperatures, several arrays were raised to temperatures ranging from 45°C-100°C. During this time, the resistance was monitored to observe the change in resistance. After heating, the sensors were allowed to cool to room temperature for vapor testing. This process was repeated several times to determine the affect of repeated temperature ramps on vapor sensitivity.

A standard array was coated with C8 nanoparticle film. The array was then monitored for 28 days at various temperatures. Sensors were tested at various temperatures to determine how temperature affects the rate of resistance drift. The array was initially monitored at room temperature for 46 hours. All sensors experienced a decrease in baseline resistance. The sensors were also heated to 50°C, 70°C, and 90°C. The array was taken to each temperature twice for an average of 24 hours. After each period of being heated, the array was allowed to cool to room temperature for vapor testing.

All sensors experienced a decrease in resistance during both periods at 50°C. After heating, the sign of the room temperature drift changed. The resistance of all sensors began to slowly increase. At 70°C, the resistance continued to increase and during and after heating. The drift remained positive for all remaining measurements. The rates of drift per hour all increased all elevated temperatures. The greatest change was seen during the first period at 90 °C where the drift rate per hour was 7.3 ± 2.0%. The drift rate slowed again after returning to room temperature as seen in Figure 4.4.

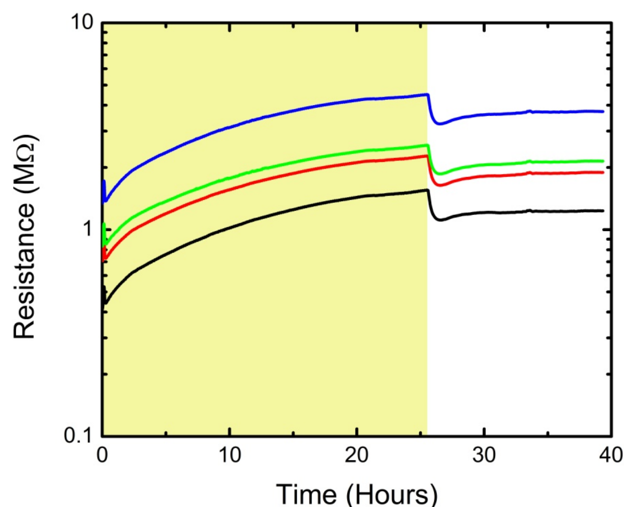

Figure 4.4 On standard C8 array, the change in resistance increases when the array is heated to 90°C (highlighted area). The drift rate slows once the array is cooled to room temperature.

Vapor testing was performed after the array was cooled to room temperature. Figure 4.5 shows sensitivity versus resistance values for each sensor. Heating the sensor led to an increase in vapor sensitivity. Before heating, the average sensitivity to toluene was 68±7. After the last heating period at 90°C, the average sensitivity rose to 117±13. Even though heating the array to 90°C increased the drift rate of the baseline resistance, it increased the vapor sensitivity.

Another array was coated with a C8 nanoparticle film. After coating, it was left to stabilize for five days to avoid testing during the "break-in" period. By day 5, the resistance values had dropped by a factor of 3. Vapor testing was performed, and the average sensitive to 200 ppm of toluene was found to be 63 ± 4. The array was kept at room temperature for an additional two weeks to monitor the baseline drift and fluctuations in sensitivity. During this time, the baseline resistances were found to have

been reduced by an average factor of 68 from their initial values. Vapor tests were performed on days 9, 13 and 15 and found to have an average value of 35±3.

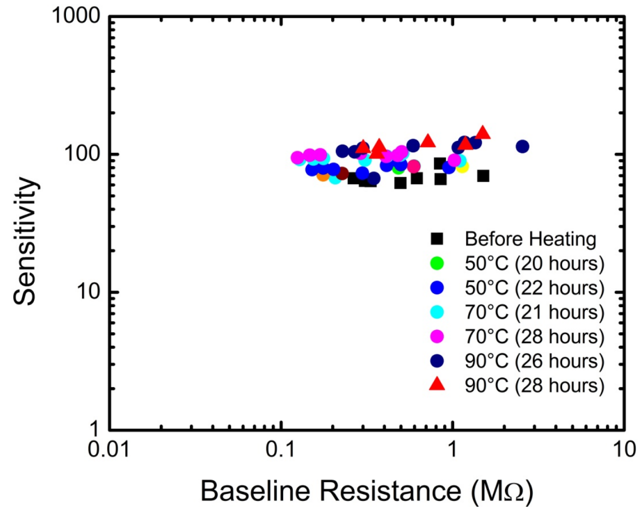

Figure 4.5 Sensitivity versus resistance for a C8 array before and after heating to 50°C, 70°C, and 90°C for a cumulative 145 hours. Vapor tests were performed after the array had been cooled to room temperature.

Over the next 29 days, the array was heated from room temperature to 70°C on six occasions for an average of 34 hours. The cumulative heating time was 204 hours. During this time, the resistance experienced both upward and downward drifts while heated. Vapor testing was performed after the array was cooled to room temperature. The sensitivity values can be seen in Figure 4.6. Over the 48 day period, the resistance of the sensors dropped an average factor of 63 from their initial value. After the 204 hours of heating, the average sensitivity to toluene changed to 41±12. Although the sensors

experience a huge decrease in baseline resistance, they only experience a 35% decrease in sensitivity.

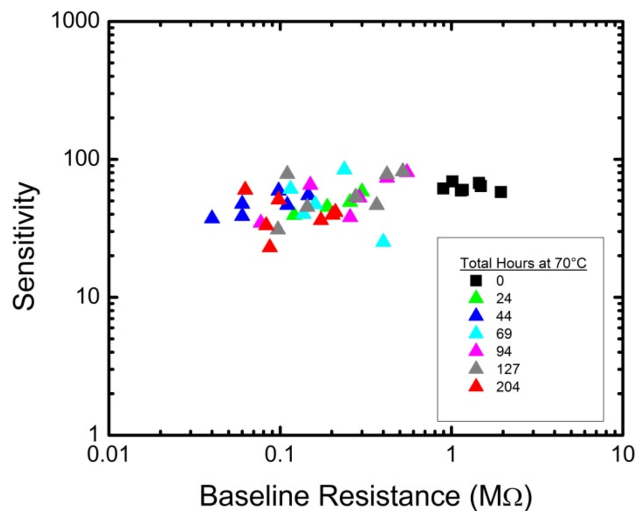

Figure 4.6 The sensitivity values $((\Delta R/R_{b})/C_{ppm})$ of C8 coated array to toluene vapor before and after heating to 70°C.

Another array was coated with a C8 film for further studies. The array was kept at room temperature for 25 days to monitor the drift in baseline resistance. During this time, the sensor arrays experienced an average decrease in resistance of 133±58 fold. Vapor testing was also performed to determine any decline in sensitivity. These values are compared in Table 4.2. Sensitivity values changed from 54±4 to 52±6 once again demonstrating that significant decreases in resistance do not impact vapor sensitivity.

From days 23 to 46, the sensor was heated to 50°C, 65°C and 15 times to 80°C. Like previous studies, the sensors were allowed to cool to room temperature for vapor testing. Figure 4.7 shows the change in sensitivity and baseline resistance for the sensor

before and after heating. The sensor was held at elevated temperatures for a cumulative 441 hours for an average duration of 26 hours.

Sensor	Day 1 Resistance (MΩ)	Day 22 Resistance (MΩ)	Day 1 Sensitivity	Day 22 Sensitivity
1	4.5	0.042	53	46
2	7.4	0.036	54	--
3	19.3	0.280	51	54
4	12.0	0.150	49	--
5	21.1	0.100	61	55
6	23.6	0.120	59	63
7	26.8	0.270	53	49
8	4.50	0.040	50	47

Table 4.2 Comparison of baseline resistance and sensitivity values for a C8 array on day 1 and day 22 while at room temperature. Values are missing for sensors 2 and 4 due to a connection error.

During this period, the sensor experience fluctuations in baseline resistance and vapor sensitivity. After its initial decrease, the sensitivity steadily increased with each temperature ramp until day 39, after 267 cumulative hours of being heated, when they reached their highest average value of 71±3. At this point, the sensitivity values began to decrease reaching their lowest point on day 46 with an average value of 44±7. From day 1 to day 46, the overall change in resistance was an average factor of 13±4. The average sensitivity changed from 54±4 to 44±7.

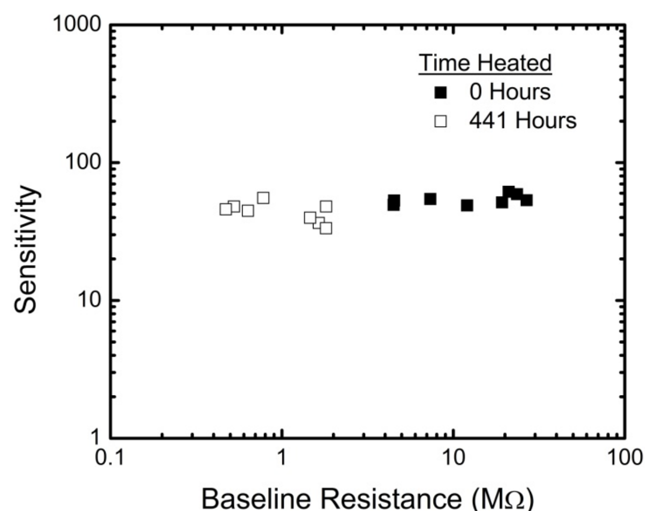

Figure 4.7 Sensitivity versus baseline resistance for a C8 coated array before after being heated to up to 80°C or 441 hours. Note that a large change in baseline resistance does not lead to a decrease in sensitivity.

In Figure 4.7, you can see that the range of resistance value covers over two orders of magnitude while sensitivity values are well within one order of magnitude. This once again demonstrates that large changes in resistance do not correspond with large changes in sensitivity. This data also suggests that gold nanoparticle coated sensor arrays can be operated at elevated temperatures without damaging vapor sensitivity. The sensor array was held at 80°C for a total of 398 hours for an average of 27 hours without any significant impact on vapor sensitivity. Sensors tested after being held at 80°C had an average sensitivity value of 54±10.

4.5 Electron Beam Induced Crosslinking

If changes in resistance in the chemiresistors are due to loss or changes in the thiol coatings, it may be possible to stabilize them through crosslinking. Crosslinking the nanoparticles through the thiol coatings could reduce the movement of nanoparticles on the surface, therefore causing less drift in baseline resistance. Crosslinking has been previously shown to reduce the noise in C8 coated sensor arrays[8]. The effects of crosslinking on chemiresistor stability were investigated by monitoring the change in baseline resistance on both uncrosslinked and crosslinked films at different temperatures

4.5.1 Drift in Baseline Resistance

A standard array was coated with four nanoparticle films. The films used were C8, OPH, and DPA. Each film was used to coat two sensors. One sensors of each film type was then exposed to a 600 μC/cm^2 electron beam dose at 30 keV. The resulting films were then monitored for changes in baseline resistance at different temperatures. In order to ensure uniform temperature, the sensors were kept in a metal enclosure previously used for vapor testing. The vapor inlet cap was replaced with a solid metal lid to ensure uniform temperature and limit exposure to outside air. Heating was done by setting the metal enclosure on a hot plate while monitoring the temperature with a thermistor inside the enclosure. The arrays were monitored at 22 ºC, 50 ºC, 75 ºC, 90 ºC, 105 ºC, and 125 ºC. The sensor was monitored for three days at each temperature. The percent change in resistance per day for all sensors is shown in Figure 4.8.

In general, the crosslinked arrays experienced less drift than uncrosslinked arrays. This trend became more pronounced at elevated temperatures. From 22 ºC to 105 ºC, all sensors had less than a 20% change in resistance per day. At 125 ºC, all sensors exhibited a significant increase in daily drift, ranging from 30% – 73%. At this temperature, the uncrosslinked sensors drifted, on average, 1.5 times faster than crosslinked arrays. While crosslinking helped decrease the drift, the upper limit for stable behavior at elevated temperature was found to be 105 °C.

For integration into a μGC system, sensors with stable baseline resistance are desirable as well as maintaining this stability at elevated temperatures. At room temperature, crosslinking does not significantly improve the stability of the baseline resistance. As the temperature is increased, the crosslinked arrays do exhibit greater baseline resistance stability. Crosslinked and uncrosslinked arrays experience less than 20% drift up to 105 °C, and begin to deteriorate rapidly at 125 °C. At 75 °C, the drift for uncrosslinked sensors was 13.2% and 9.4% for crosslinked sensors which makes it a reliable operating temperature for sensors integrated into a μGC system.

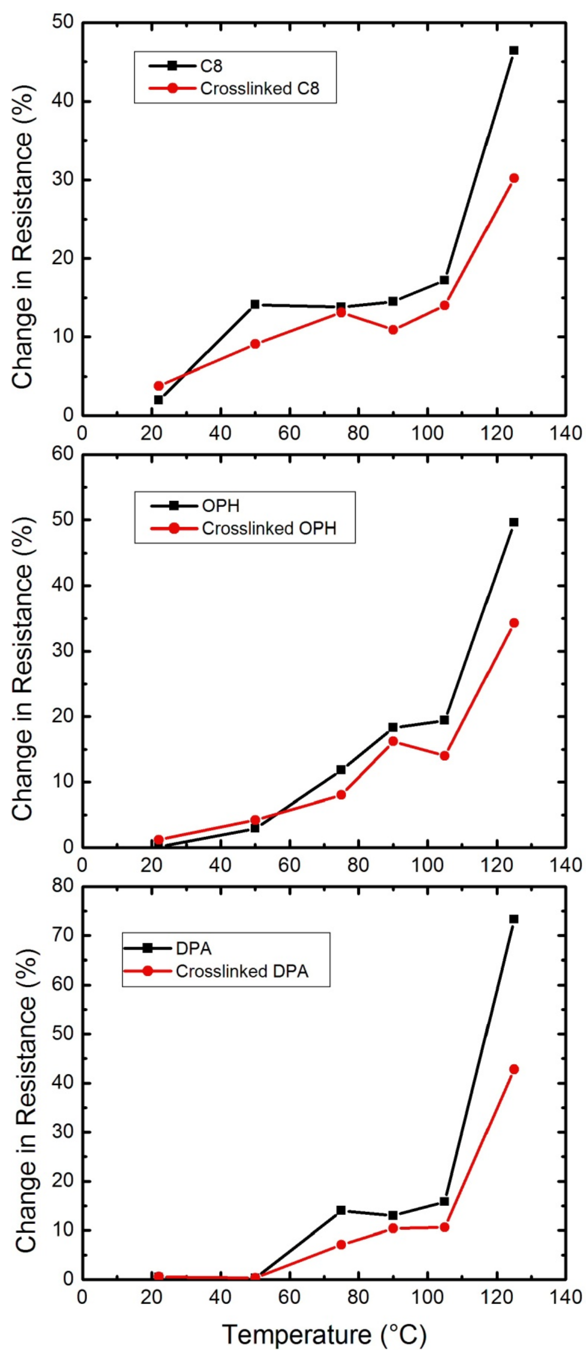

Figure 4.8 The daily percent change in resistance of an array coated with C8, OPH, and DPA films where half of the sensors are crosslinked. The sensors were monitored at 22 ºC, 50 ºC, 75 ºC, 90 ºC, 105 ºC, and 125 ºC. Crosslinked films generally experience less drift especially at elevated temperatures.

4.5.2 Changes in Vapor Sensitivity

While crosslinking the nanoparticle films may increase stability in baseline resistance, it can also decrease vapor sensitivity. Crosslinking the nanoparticles limits the swelling response from incoming vapors, because nanoparticles are more rigidly connected and cannot freely move apart when exposed to an analyte. It is therefore important to determine how significantly crosslinking can impact vapor sensitivity.

C8 coated sensors were exposed to a different electron beam doses. All sensors were exposed at 14 nA and 30 keV. The exposure doses were 100, 300, 600, 900, 1500, 1800, and 2000 $\mu C/cm^2$. One sensor was not exposed. Sensors were then tested for their sensitivity to toluene vapor. The results are shown in Figure 4.9. The sensitivity to toluene decreases with increasing electron beam dose. From no exposure to 2000 $\mu C/cm^2$, there is a 38% drop in sensitivity. In previous studies, 600 $\mu C/cm^2$ was found to decrease the noise prefactor of a chemiresistor. At this dose, the sensitivity decreased by only 13.5%.

This array was also heated to 50°C, 70°C, and 90°C to determine if crosslinking had any effect on vapor sensitivity of sensors that have been heated. Figure 4.9 also shows the sensitivity to toluene vapor after being heated and cooled to room temperature. The array was heated to 70°C for 16 hours, 50°C for 18 hours and 90°C for 6 hours. The sensitivity increased by an average 48% after being held at an elevated temperature for 40 cumulative hours. The greatest increase in sensitivity occurred with the uncrosslinked sensor (62%). The most crosslinked sensor (2000 $\mu C/cm^2$) experienced a 53% increase.

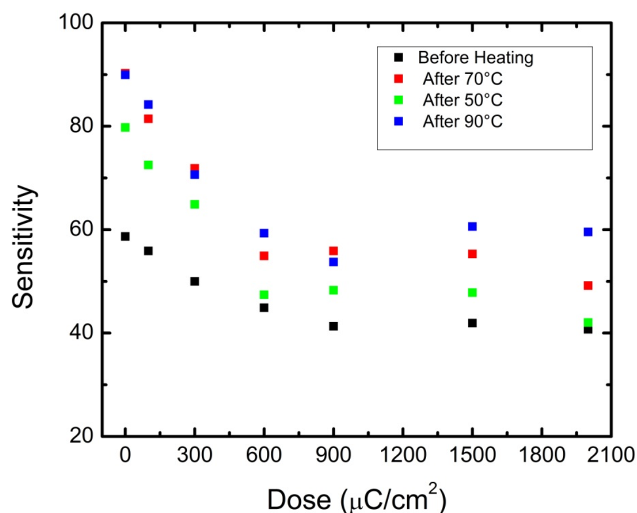

Figure 4.9 Higher electron beam exposure leads to a decreased sensitivity to toluene vapor. This trend continues after heating the arrays to 50°C, 70°C, and 90°C.

4.6 Film Contamination

One possible cause on chemiresistor instability could be contaminates within the nanoparticle film. Impurities, such as ionic contaminants from the nanoparticle synthesis, could have significant effects on the electronic properties of the film and cause irreversible changes in the baseline resistance of the sensors. Nanoparticles have been synthesized using a single phase synthesis[5] in order to eliminate ionic contaminants commonly introduced using the Brust synthesis method[9]. It is still possible that other contaminants could be incorporated into the film during the synthesis or film deposition process.

In order to study the effects of contaminates on vapor sensitivity, we systematically contaminated a C8 nanoparticle solution with the organic compound

naphthalene. The effect of naphthalene on noise prefactor was discussed in Chapter 2. A standard array was coated with a C8 nanoparticle film with 0%, 10%, or 20% naphthalene. Sensors were exposed to a 200 ppm toluene vapor mixture in air. Sensitivity values were averaged for films of the same contaminate level and found to decrease with increasing the percentage of naphthalene in the film. Sensitivity values are shown in Figure 4.10. The average sensitivity decreased by 9% from a pure C8 film to 20% naphthalene film, indicating that film purity does affect the performance of MPN coated chemiresistors. Sensors with higher naphthalene concentration had higher baseline resistances. This is most likely caused by an increased spacing between nanoparticles due to displacement from naphthalene. Due the increased spacing between nanoparticles, the swelling response of the film could be compromised causing a decrease in sensitivity.

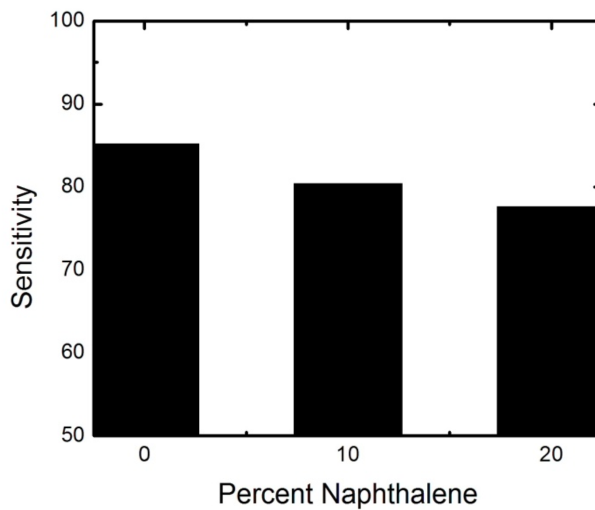

Figure 4.10 The sensitivity ($\left(\Delta R/R_b\right)/C_{ppm}$) to toluene vapor decreases and the percentage of naphthalene in the C8 nanoparticle film increases.

4.7 Conclusions

Chemiresistors experience changes in baseline resistance over time. At room temperature, chemiresistors usually have a reduction in resistance, although increases in baseline resistance have also been observed. Previous studies have stated that the change in baseline resistance is caused by oxidation of the sulfur bond causing loss of the nanoparticle's ligand coating, which causes coalescences of nanoparticles[1]. We investigated these claims by performing temperature dependent I-V measurements on a sample aged for 90 days. Over this period, the sensor experienced a drastic reduction in resistance but less than 10% change in activation energy; therefore, the large change in resistance cannot be attributed to changes in the sizes of the gold core of the nanoparticles. Although loss of ligand could cause a downward drift in resistance by allowing closer spacing between nanoparticles, the loss isn't significant enough to cause agglomeration of the gold cores.

We monitored chemiresistor arrays at room temperature and elevated temperature over extended periods to monitor their baseline drift and changes in sensitivity to toluene vapor. All arrays experienced changes in baseline resistance, although the sign of the drift varied between different arrays. While the sign of the drift could change from array to array, all sensor on a single array experience the same direction of drift. The rate of drift was also comparable between sensors on the same array regardless of their initial resistance values. Heating was found to increase the drift rate, although the rate slowed once the array was cooled to room temperature.

We also studied the changes in sensitivity to toluene vapor. Even after large changes in resistance, sensors remained response to toluene. While baseline resistance could change by orders of magnitude, vapor sensitivity did not show significant changes. Even sensors that were heated did not experience reduction in vapor sensitivity. Some arrays even experienced an increase in vapor sensitivity after extended periods at elevated temperatures. This indicates that chemiresistors arrays can be operated at elevated temperatures without compromising sensor performance.

Electron beam induced crosslinking was investigated as a means to stabilize the baseline resistance of the nanoparticles. If the change in resistance is due to loss of ligand, crosslinking the ligands through electron beam exposure may inhibit this loss by causing a more rigid nanoparticle film. We monitored an array with both crosslinked and uncrosslinked sensors at different temperature to compare the changes in resistance. Even after crosslinking, sensors experience large changes in baseline resistance. At temperatures below 100°C, the magnitude of drift was similar between uncrosslinked and crosslinked sensors. Above 100°C, crosslinked sensors did experience less drift.

We crosslinked another array to determine the effect of electron beam induced crosslinking on vapor sensitivity. Each sensor on an array was crosslinked with a different electron beam dose. The sensors were vapor tested, and crosslinked sensors had a lower sensitivity to toluene vapor. This is most likely due to a reduction in the swelling response of the nanoparticle film. Nanoparticles linked together by their ligands have less freedom to move apart from neighboring nanoparticle causing a reduction in the swelling response. This array was also heated to see if crosslinked helped maintain vapor

sensitivity after heating. All sensors experienced an increase in sensitivity after heating, although the largest increase was seen with uncrosslinked sensor. Overall, crosslinking was not found to reduce the baseline drift of the sensors and was found to reduce the vapor response.

Impurities in the nanoparticle film were hypothesized to be a cause of instability and reduction of vapor sensitivity. An increase in baseline resistance could be caused by the nanoparticle film absorbing impurities within the testing chamber. We purposefully contaminated an array with naphthalene to investigate the effect of impurities on vapor sensitivity. Sensors with the highest level of naphthalene had the lowest sensitivity to toluene vapor indicating that nanoparticle purity is imperative in improving the limit of detection.

Although the cause of the changes in baseline resistance was not found, it was shown to not be caused by changes in the size of the nanoparticle core. All sensors on the same array experience the same direction in drift and similar magnitudes of change indicating that the cause of change is unique to a particular array and not the individual sensor. It was also shown that sensors remain responsive after large changes from their initial resistance values. Sensitivity was also not compromised from keeping the sensors at elevated temperatures for extended periods which is a promising result for integration into a μGC system.

4.8 References

1. Y. Joseph, B. Guse and G. Nelles, Chem. Mat. **21** (8), 1670-1676 (2009).
2. T. M. Willey, A. L. Vance, T. van Buuren, C. Bostedt, L. J. Terminello and C. S. Fadley, Surf. Sci. **576** (1-3), 188-196 (2005).
3. M. H. Schoenfisch and J. E. Pemberton, J. Am. Chem. Soc. **120** (18), 4502-4513 (1998).
4. N. Sandhyarani and T. Pradeep, Chem. Phys. Lett. **338** (1), 33-36 (2001).
5. M. P. Rowe, K. E. Plass, K. Kim, Ç. Kurdak, E. T. Zellers and A. J. Matzger, Chem. Mat. **16** (18), 3513-3517 (2004).
6. F. I. Bohrer, E. Covington, C. Kurdak and E. T. Zellers, Anal. Chem. **83** (10), 3687-3695 (2011).
7. W. H. Steinecker, K. Sun Kyu, F. I. Bohrer, L. Farina, C. Kurdak and E. T. Zellers, IEEE Sens. J. **11** (2), 469-480 (2011).
8. E. L. Covington, R. W. Turner, C. Kurdak, M. P. Rowe, X. Chao and E. T. Zellers, Proceedings of the IEEE Sensors Conference, 102-105 (2008).
9. M. Brust, M. Walker, D. Bethell, D. J. Schiffrin and R. Whyman, J. Chem. Soc.-Chem. Commun. (7), 801-802 (1994).

Chapter 5

Thermoelectricity in Arrays of Thiolate Coated Au Nanoparticles

5.1 Introduction

The transport properties of gold nanoparticles have been shown to be dominated by tunneling[1-3]. Whether the tunneling is through the highest occupied molecular orbital (HOMO) or lowest unoccupied molecular orbital (LUMO) has not been determined and cannot be determined through conventional current-voltage measurements[3]. Studies have shown that electron and hole tunneling can be distinguished through thermoelectric measurements of molecular junctions[4, 5]. We developed a novel technique for measuring the thermoelectric voltage of an MPN film. Using this technique, we measured the thermoelectric voltage of three MPN films and the method of transport was determined. Noise thermometry and thermal scanning probe measurements were performed in order to calculate the thermopower of the films.

5.2 Thermoelectricity

Thermoelectricity is the induced voltage from a temperature differential across a material. It is usually expressed in terms of S, the Seebeck coefficient, which is defined in

terms of the induced thermoelectric voltage, ΔV, produced for an applied temperature gradient, ΔT.

$$S = -{}^{\Delta V}/_{\Delta T} \tag{5.1}$$

The Seebeck coefficient is also referred to as the thermopower. Thermoelectricity is also used to describe the temperature gradient induced from an applied voltage. Unlike Joule heating, which is irreversible and always positive, the thermoelectric effect can lead to heating or cooling depending on the direction of current flow or temperature gradient[6].

The sign of the thermoelectric voltage can also reveal the transport mechanism in a material. This is analogous to the hot point probe measurement used to determine whether semiconductors are p-type or n-type. In a hot point probe measurement, one lead of a voltmeter is attached to a heating source. The heat will cause either electrons (n-type) or holes (p-type) to move away from the lead and causing a voltage difference. The sign of the voltage change will indicate the type of semiconductor. For thermoelectric measurements, the sign of the thermoelectric voltage reveals information about the location of the Fermi energy with respect to the nearest molecular orbital[5]. When the Fermi energy is closer to the LUMO, the thermoelectric voltage is positive and electrons are tunneling. When the Fermi energy is closer to the HOMO, the thermoelectric voltage is negative and holes are tunneling.

The thermoelectric effect has been used to study the transport properties of molecules[4, 5, 7, 8]. Unlike current-voltage (I-V) measurements, thermoelectric measurements can reveal the transport mechanism without detailed knowledge of the

contacts. This is done by determining the location of the Fermi energy with respect to the highest occupied molecular level (HOMO) or lowest unoccupied molecular level (LUMO). This is detailed by Paulsson and Datta in a paper where the thermoelectric current and voltage is estimated for a phenyldithiol (PDT) molecule[5]. Consider a left and right reservoir with Fermi-Dirac distribution functions of f_L and f_R, respectively. The electrical transport can be presented in terms of the transmission, $\mathcal{T}$(E), by the Landauer formula:

$$I = \frac{2e}{h}\int_{-\infty}^{\infty} \mathcal{T}(E)[f_L(E) - f_R(E)]dE. \tag{5.2}$$

In the presence of a temperature difference, a thermoelectric current will arise at zero bias voltage and can be represented with the Sommerfield expansion,

$$I = -\frac{e^2}{\pi h}\mathcal{T}(E_F)V + \frac{e}{\pi h}\frac{\pi^2 k_B^2 T^2}{3}\frac{\partial \mathcal{T}(E)}{\partial E}\bigg|_{E_F} \Delta T, \tag{5.3}$$

where T is the average temperature of the contacts. Since the thermoelectric current is small enough to be represented as a linear circuit, the conductance can be written as,

$$G = \frac{e^2}{\pi h}\,\mathcal{T}(E). \tag{5.4}$$

Combining Equation 2 and Equation 3 gives,

$$V|_{I=0} = \frac{\pi^2 k_B^2 T}{3e}\frac{\partial \ln \mathcal{T}(E)}{\partial E}\bigg|_{E_F} \Delta T. \tag{5.5}$$

Equation 5 shows that the thermoelectric voltage is dependent on the slope of the transmission at E_F. From Figure 5.1, one can see that the slope of the transmission at E_F changes in relation to the proximity to the HOMO or LUMO; therefore, the sign of the

thermoelectric voltage can determine the location of E_F with respect to the molecular levels.

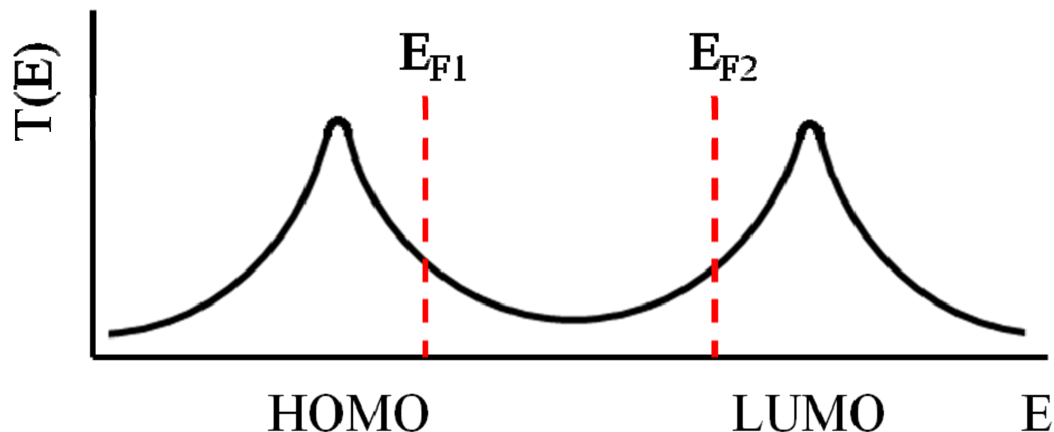

Figure 5.1 Plot of the transmission, $\mathcal{T}(E)$ as a function of energy. The slope of $\mathcal{T}(E)$ depends on the location relative to the HOMO or LUMO. The location of the Fermi energy, E_F, is closer to the HOMO, like E_{F1}, then holes tunnel through the HOMO. If the E_F is closer to the LUMO, like E_{F2}, then electrons tunneling through the LUMO.

This method has been used to measure the Seebeck coefficients of molecular junctions using a scanning tunneling microscope (STM) [4]. By trapping molecule between a gold substrate and a gold STM tip with a temperature difference, the Seebeck coefficient of benzenedithiol (BDT), dibenzenedithiol (DBDT), and tribenzenedithiol (TBDT) were calculated. All had positive coefficients indicating p-type tunneling. The Seebeck coefficient was also found to be independent of the number of molecules between the substrate and STM tip. A positive linear relationship was also found between the thermopower and the molecular length. Note that is opposite from the electrical resistance which decreases with molecular length due to reduction in the tunneling probability.

5.3 Thermopower Measurements of MPN Films

Measuring the thermopower of bulk materials is done by applying a large temperature gradient over the material and measuring the induced thermoelectric voltage. This has not, and cannot, be done to MPN films due to their highly resistive nature. To measure the thermoelectric voltage of a MPN film, we developed a new technique. We deposited an MPN film between two closely spaced electrodes. By heating one electrode with a low frequency AC current, a temperature difference was established across the film. The induced thermoelectric voltage was measured across the electrodes. This sign of the voltage distinguished electron and hole tunneling. Noise thermometry was performed to determine the exact temperature from an applied voltage. We performed thermal probe measurements to determine the temperature gradient across the film, and then the Seebeck coefficient was calculated. This technique is presented for MPN films but can be used for other high resistance materials. This technique is not applicable for low resistance materials, because the two electrodes will become shorted. Traditional thermopower measurements should be used for such materials.

5.3.1 Fabrication

To study the thermoelectric properties of the nanoparticle films, we fabricated gold wires by electron beam lithography. The wires were 400 μm long with width and spacing of either 500 nm or 1000 nm and thickness of 250 Å. An optical and SEM image of the wires is shown in Figure 5.2. The wires contain multiple contact pads, because they will be used for both heating and electrical characterization. Each wire has contact pads

at each end. Two additional contact pads are located 50 μm from the outside pads. A typical wire had a four terminal resistance of 890 Ω.

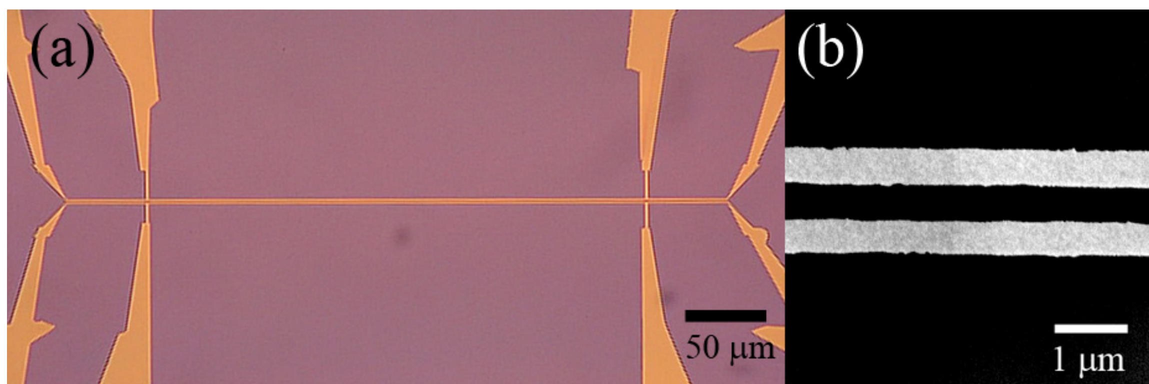

Figure 5.2 (a) Optical image of two 400 mm long parallel gold wires with width and spacing of 500 nm. (b) A SEM image of the wires.

The wires were coated with a nanoparticle film with a micro-dispensing system. In this study, 1-octanethiol (C8) and mercapto-diphenylacetylene (DPA) nanoparticle were used. Due to the coffee stain pattern of the deposited film[9], the edge of the droplet was aimed for the region between the wires. This ensured that the thickest portion of the film would lie between the wires. Because the films were highly resistive, we performed electron induced crosslinking to reduce the resistance of the films and make them more easily measurable. Figure 3.1 shows how the resistance of a chemiresistor decreases with increasing electron beam dose.

5.3.2 Noise Thermometry

In order to determine the induced temperature difference in the film, we performed noise thermometry on the uncoated gold electrodes. Noise thermometry is the determination of temperature by the measurement of the thermal noise. This noise is

proportional to the temperature and can be used as a primary thermometer. Since it is a primary method of measuring temperature, it does not have to be calibrated. The thermal noise, also known Johnson-Nyquist noise, is defined as

$$\overline{V_{rms}}^2 = 4k_B RT\Delta f \tag{5.6}$$

where V_{rms} is the root mean square (rms) voltage, k_B is the Boltzmann constant, T is the temperature in degrees Kelvin, R is the resistance, and f is frequency[10].

In this study, the Johnson noise was measured using a spectrum analyzer to capture the power spectral density function, $S_V(f)$.

$$S_V(f) = \frac{V_{rms}^2}{\Delta f} = 4k_B RT \tag{5.7}$$

To determine the change in temperature, $S_V(f)$ was measured at different voltages. Since the resistance of the wire is known, $S_V(f)$ can be used to calculate the temperature difference.

$$\Delta S_V = 4k_B R\Delta T \tag{5.8}$$

Noise thermometry is a primary thermometer and therefore needs no calibration.

Figure 5.3 shows a schematic of the experimental set-up. A DC current was applied across one wire via the outer contact pads. The inner contact pads were used to measure $S_V(f)$ by being connected to the A and B input of a current sensitive analyzer. The output (A-B) was then measured by a spectrum analyzer to measure $S_V(f)$.

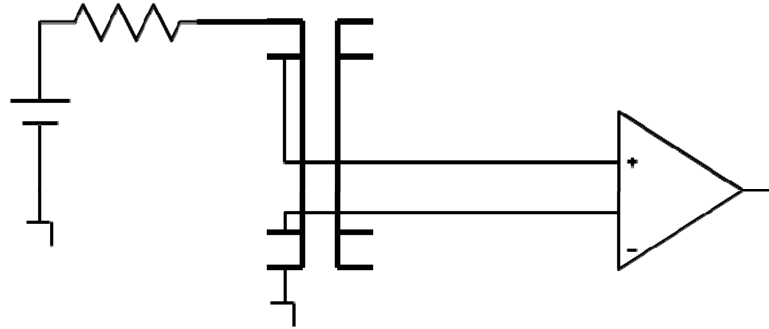

Figure 5.3 Schematic of the experimental set-up for noise thermometry measurements. A battery is used to apply a voltage across the outer contact pads. The inner contact pads are used to measure the noise power spectral density function with a spectrum analyzer. The resistor was 3 kΩ.

Measurements were taken at several applied voltages ranging from 0 V to 18 V with a 3 kΩ resistor. As seen in Figure 5.4, $S_V(f)$ = 3.78×10^{-17} V^2/Hz at 0 mA, $S_V(f)$ = 3.82×10^{-17} V^2/Hz at 3.5 mA and $S_V(f)$ = 3.89×10^{-17} at 4.5 mA. The frequency dependence of $S_V(f)$ can be attributed to the noise of the amplifier.

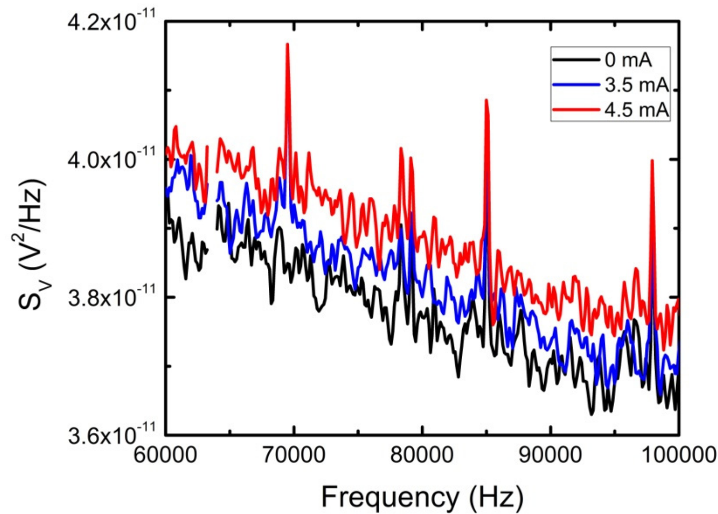

Figure 5.4 $S_V(f)$ at 0, 3.5 and 4.5 mA. The slight frequency dependence of $S_V(f)$ is due to amplifier noise as is it present even at 0 mA.

Figure 5.5 shows $S_V(f)$ versus the square of the current. Currents ranged from 0 to 4.5 mA. Because of the voltage drop across the 3 kΩ resistor, a correction factor is needed to calculate $S_V(f)$. With this correction factor, Equation 5.8 becomes

$$\Delta S_V(f) = [(R_1 + R_2)/R_2]^2 \, 4k_B R \Delta T \tag{5.9}$$

where R_1 is the resistance of the gold wire and R_2 is the resistor shown in Figure 1.3. Using Equation 5.9, gives a change in temperature of 40 K from 0 to 4.5 mA.

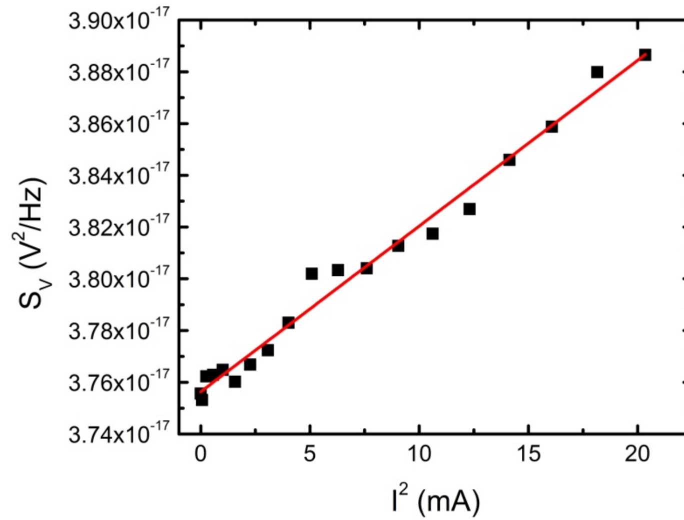

Figure 5.5 Noise power spectral density function, $S_V(f)$, versus current squared for a 1 μm thick, 400 μm long gold wire. From the slope of this graph, the temperature can be calculated from a given current. At 4.5 mA, the increase in temperature is 40 K.

Although the temperature of the heated line can be determine by noise thermometry, the temperature gradient across the film was still unknown. To determine the change in temperature across the film, we scanned the wires with a thermal probe. By scanning the thermal probe perpendicular to the wire, it is possible to determine the

temperature profile created by the heated wire. From this, the temperature of the unheated wire can be calculated and used to determine ΔT across the nanoparticle film.

Figure 5.5(a) shows an image of the thermal scan of the gold wire. The heated area is clearly visible as the bright white region of the image. In Figure 5.5(b), the temperature profile is shown for 0 V to 3.5 V. In each scan, the width of the heated area is approximately 2 μm. Since the unheated wire is 1.5 μm away from the heated wire, it is directly outside of the heated region.

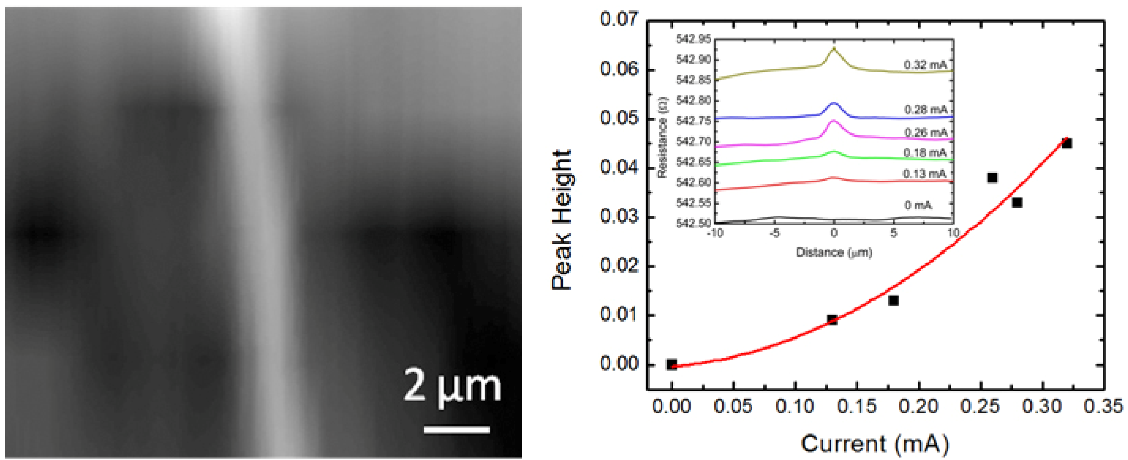

Figure 5.6 (a) Thermal probe scan of the approximately 2 μm area heated by applying a current across a 1 μm wide gold electrode. The white area is the heated region. (b) (inset) The change in resistance of the thermal probe as a function of distance from the center of the electrode (at 0 μm). From this, we can determine ΔT across the nanoparticle film. The second wire, located at 1.5 μm is outside of the heated region. The peak heat and current scales quadratically.

5.3.3 Thermoelectric Voltage

Once thermal probes scans verified that there was a temperature differential across the film, the induced thermoelectric voltage could be measured to determine the

type of tunneling. This was done by applying an AC voltage across one wire to induce a temperature difference. The induced voltage was then measured between the heated and unheated wire with a lock-in amplifier as shown in Figure 5.6.

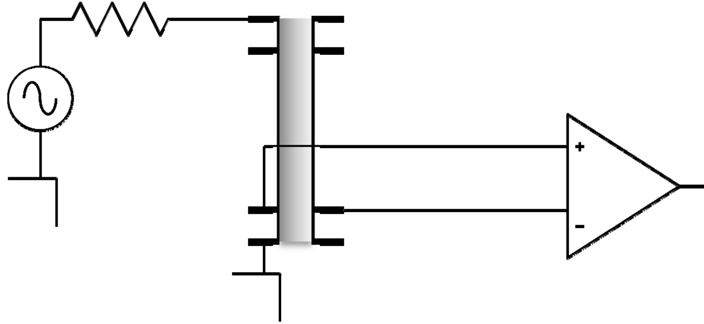

Figure 5.7 Schematic of the experimental set-up used to measure the induced voltage across a nanoparticle film. The dark bars represent the gold electrodes with four contact pads per side while the grey region represents the area coated with a nanoparticle film (not drawn to scale). The far left wire was excited with an AC current to create a temperature difference, and the induced voltage was measured between the wires.

As shown in Figure 5.7, an AC current was used to heat one electrode causing a temperature difference across the nanoparticle film. The applied current has the form of:

$$I = I_0 \cos \omega t. \tag{5.9}$$

Because the heat produced is proportional to the square of the current, the induced temperature across the film will be proportional to

$$\Delta T \propto {I_0}^2 \cos^2 \omega t \tag{5.10}$$

causing the temperature to be modulated by even factors of ω. To determine the induced voltage, independent of the voltage induced by the 1ω component generated by the

inherent resistance, only the second harmonic, $V_{2\omega}$, was measured. The sign of the induced voltage determines the transport mechanism; therefore, the validity of the sign measured through the lock-in amplifier was verified by using a rectifying circuit. The lock-in amplifier measured a negative out of phase voltage, and the data has been modified to take this into account.

In this study, one C8 film and two DPA films were measured. Because the films were highly resistive, they were crosslinked to decrease their resistance. The C8 film was crosslinked with an electron beam dose of 20 mC/cm^2. The DPA films were crosslinked with electron beam doses of 40 mC/cm^2 and 100 mC/cm^2. After crosslinking, the resistance across the wires was 0.8 MΩ for the C8 film, 16 MΩ for the DPA film crosslinked by 40 mC/cm^2, and 9 MΩ for the DPA film crosslinked by 100 mC/cm^2. Figure 5.8 shows the second harmonic of the voltage versus current for the three films.

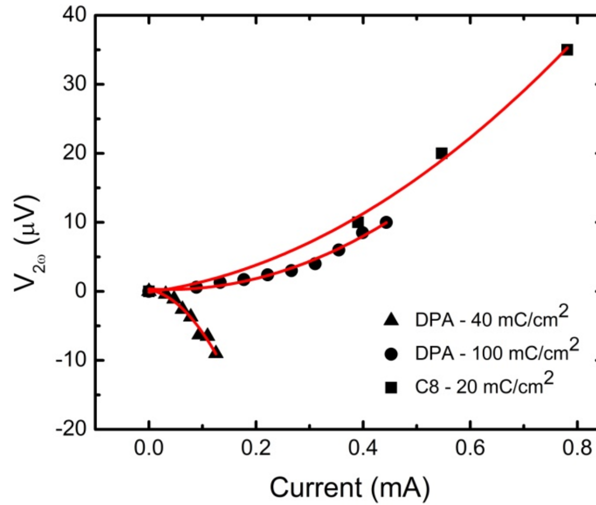

Figure 5.8 The second harmonic of the voltage, $V_{2\omega}$, as a function of applied current for three different nanoparticle films. All films were electron beam crosslinked. Positive $V_{2\omega}$ indicates electron tunneling in the C8 film and 100 mC/cm^2 crosslinked DPA film. The 40 mC/cm^2 has a negative sign indicating hole tunneling.

The C8 film had a positive $V_{2\omega}$ indicating that the Fermi energy is closer to the LUMO; therefore, the transport is attributed to the tunneling of holes. This is consistent with experimental results on alkanethiol molecules [11]. DPA had a negative $V_{2\omega}$ with a crosslinking dose 40 mC/cm^2 and a positive $V_{2\omega}$ with a dose of 100 mC/cm^2. This could indicate that extensive crosslinking could change the method of transport within the nanoparticle film.

Using Equation 5.1, the Seebeck coefficients can be calculated. In order to calculate the Seebeck coefficients from $V_{2\omega}$, the corresponding $T_{2\omega}$ must be calculated. Since an AC current was applied, a correction factor of $1/\pi$ is needed to calculate $T_{2\omega}$ from the temperature determined from noise thermometry. The Seebeck coefficient for C8 is 92 μV/K. For DPA, the Seebeck coefficients are 916 μV/K and 82 μV/K for films crosslinked to 40 mC/cm^2 and 100 mC/cm^2, respectively.

5.4 Conclusions

We developed a new technique for determining the method of transport for a nanoparticle film is presented. Two closely spaced electrodes can be used to characterize a film by heating one wire and creating a temperature difference across the film. The temperature difference induces a thermoelectric voltage that can be used to determine the location of the Fermi energy with respect to the HOMO or LUMO. Since the voltage is dependent on the slope of the transmission, measuring the induced voltage can determine the whether the Fermi energy is closer to the HOMO or LUMO. Proximity to the HOMO

indicates the transport is due to hole tunneling. Proximity to the LUMO indicates transport through electron tunneling.

To induce a temperature difference across the film, the film is deposited between two closely space wire fabricated by electron beam lithography. By fabricating multiple contact pads on the wires, they can be used to for both heating and characterization. Noise thermometry is performed on the wires to determine the temperature of the heated wire. A thermal probe is then used to determine the temperature profile and determine the temperature of the second wire. The second wire was found to be spaced sufficiently away from the heated wire and was not within the heated region.

To measure the induced voltage, an AC current is used to heat one wire. From the applied current, a temperature modulated by 2ω is generated. The voltage difference across the two wires is then measured. To ensure that the voltage measured is caused by the thermoelectric effect and not the inherent resistance, only the second harmonic of the voltage is measured. The sign of the induced voltage will indicate the transport mechanism. A C8 film was measured as having electron tunneling, while two DPA films exhibited both electron and hole tunneling depending on the dose of the electron crosslinking. In future measurements, a new wire design can be implemented to prevent the need for extensive crosslinking. By using a meandering wire, the total length of the wire could be increased by a factor of 10 making the resistance of the MPN film more easily measurable.

5.5 References

1. Ç. Kurdak, J. Kim, L. A. Farina, K. M. Lewis, X. Bai, M. P. Rowe and A. J. Matzger, Turk. J. Phys. **27**, 419-426 (2003).
2. M. G. Ancona, W. Kruppa, R. W. Rendell, A. W. Snow, D. Park and J. B. Boos, Phys. Rev. B **64** (3) (2001).
3. W. Y. Wang, T. Lee and M. A. Reed, Rep. Prog. Phys. **68** (3), 523-544 (2005).
4. P. Reddy, S.-Y. Jang, R. A. Segalman and A. Majumdar, Science **315** (5818), 1568-1571 (2007).
5. M. Paulsson and S. Datta, Phys. Rev. B **67** (24), 241403 (2003).
6. D. K. C. MacDonald, *Thermoelectricity: an introduction to the principles*. (Wiley, New York, 1962).
7. K. Müller, J. Chem. Phys. **129** (4), 044708 (2008).
8. Y.-S. Liu and Y.-C. Chen, Phys. Rev. B **79** (19), 193101 (2009).
9. R. D. Deegan, O. Bakajin, T. F. Dupont, G. Huber, S. R. Nagel and T. A. Witten, Phys. Rev. E **62** (1), 756 (2000).
10. J. B. Johnson, Phys. Rev. **32** (1), 97-109 (1928).
11. Y. Qi, O. Yaffe, E. Tirosh, A. Vilan, D. Cahen and A. Kahn, Chem. Phys. Lett. **511** (4-6), 344-347 (2011).

Chapter 6

Sensor System Integration

6.1 Introduction

The goal of this collaborative project has been to create a fully integrated μGC system for the trace detection of complex vapor mixtures. To do so, the sensor array will be interface with other μGC components, such as the μGC columns and readout electronics. To improve the detection limit, the sensor array needs to be packaged into a chamber with a low dead volume. The MPN films are coated before packaging making it a non-trivial task to fabricate a sealed, low-volume chamber without disturbing the sensor array. The package must also allow for interfacing between the sensor array and readout electronics.

In this chapter, the challenges associated with fabricating a monolithic sensor system, with the sensor array fabricated on the surface of the readout electronics chip, is discussed. We successfully fabricated a sensor array on a 2.2×2.2 mm^2 readout chip. Vapor testing was performed to determine the array's functionality[1]. The chip was then packaged and interfaced to a GC system for vapor testing[2].

6.2 Integrated Sensor System

Integrating the sensor arrays into a μGC system includes the development of electronic instrumentation to read the sensor's responses. The electronic instrumentation can also be used to improve the μGC performance by tracking the drift in baseline resistance. The baseline resistance can then be cancelled out to provide a higher resolution response. The readout circuitry can also include low pass filtering to decrease the noise. Our collaborators at Michigan State University (MSU), led by Dr. Andrew Mason, have been developing a readout circuitry chip for the chemiresistor array[3, 4]. In order to further scale down the μGC system components, we decided to fabricated the chemiresistor array directly on the surface of the readout chip to create a monolithic sensor system[1]. Creating a monolithic sensor system can also reduce noise by eliminating noise from wires between the sensor array and readout electronics.

In the first generation of the readout chip, shown in Figure 6.1, the sensor array was meant to be fabricated across a large region of the chip's surface. In the zoomed in region of Figure 6.3, the readout circuitry is clearly visible beneath the surface of the chip. We fabricated the IDEs via electron beam lithography as well as the contact pads to the large circular contact pads that connect the IDEs to the embedded circuitry. Unfortunately, the first attempt of sensor and readout chip integration was unsuccessful due to the roughness of the chip's surface.

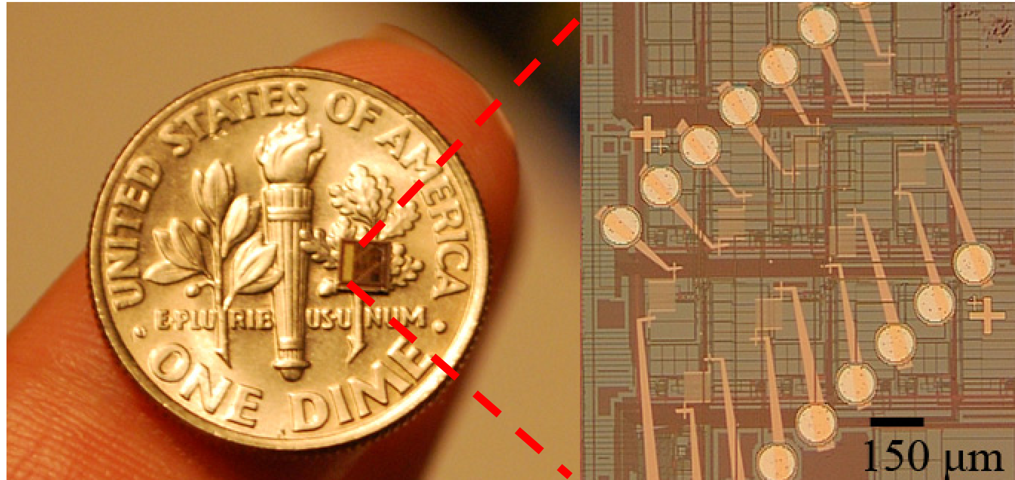

Figure 6.1 The 2.2×2.2 mm^2 read-out chip with an eight sensor array fabricated on the surface of the chip. The large circles are contact pads that connect the sensors to the embedded electronics.

The metal lines in the embedded circuitry caused large variations in the topography of the chip. As seen in Figure 6.2, the metal lines under the surface caused discontinuities in the IDEs. In Figure 6.2(a), an optical image shows two large metal lines that are clearly seen under the surface of the chip. In Figure 6.2(b), a SEM images show the discontinuities in the IDEs caused by the height difference caused by the metal lines.

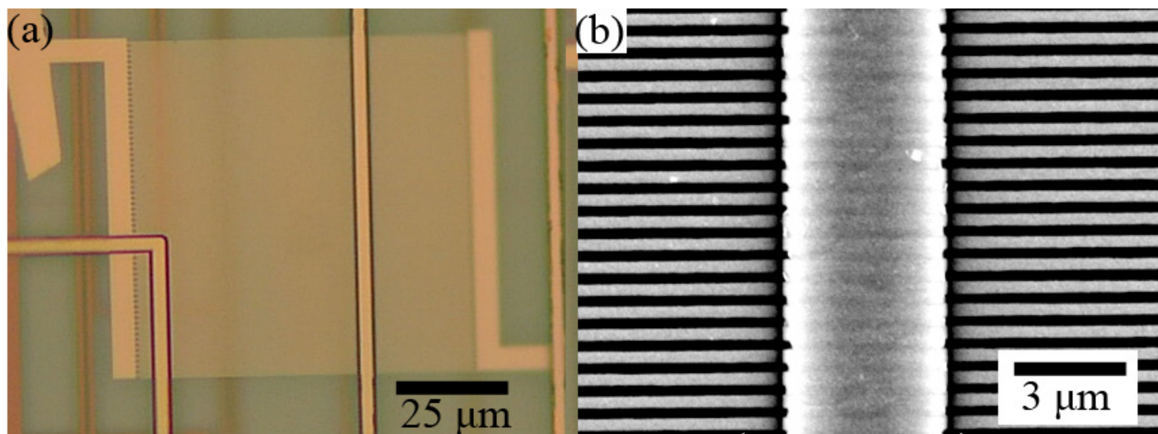

Figure 6.2 (a) IDEs fabricated on read-out chip in an area with an uneven surface due to embedded metal lines. (b) SEM image of the discontinuities of the IDEs due to the metal lines under the chip's surface.

In order to rectify this problem, several solutions were proposed. An isolated region on the chip could be specified for sensor array fabrication, and no embedded circuitry would be allowed directly under this area. Another solution would be to fabricate a metal plateau between the circuitry and prevent the abrupt changes in topography due to the metal lines. Another solution would be to planarize the chip's surface afterward using chemical mechanical polishing. In order to address another issue that arises from using electron beam lithography, a metal plateau was fabricated beneath the area designated from the sensor array.

In addition to overcoming issues with surface topography, the metal plateau was also fabricated to shield the embedded circuitry from electron beam exposure. Figure 6.3 shows the sensor region, inside the red square, with a metal plateau beneath the surface. It has been reported that transistors exposed to an electron beam experience a shift in threshold voltage and leakage of current. This is caused by the trapping of electron-hole pairs within the gate oxide which causes a shift in the transistor threshold voltage [5, 6]. Post exposure annealing has been shown to alleviate the damage[5]. In a chip with test transistors with and without a metal shield, the metal plateau was not found to shield the electronics from the high energy electrons. Shielded transistors were still found to have a shift in their threshold voltage. Annealing at 200 °C for eight hours was found to reduce but not completely eliminated the shift. It was discovered that in order to protect the embedded circuitry, the area exposed by the electron beam would need to be removed by a lateral distance of 120 µm or more[1].

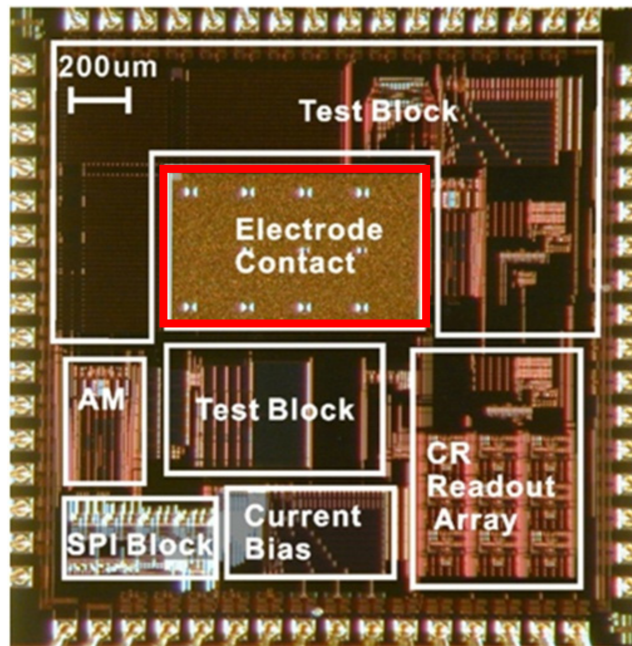

Figure 6.3 The 2.2×2.2 mm^2 read-out chip, designed by our collaborators at MSU, with a metal region plateau the sensor region (surrounded by red square). The chemiresistor (CR) readout electronics are located at the bottom right region of the chip to limit the embedded electronics exposure to high energy electrons during electron beam lithography.

While the metal plateau was not successful in protecting the embedded circuitry from damage from the electron beam, it was successful in creating a planar site for IDE fabrication. In order to prevent electron beam damage, the circuitry was removed from the sensor region, as shown in Figure 6.3. The readout circuitry was moved the bottom right of the chip and does not overlap with the sensor fabrication region.

As shown in Figure 6.4, we fabricated an eight sensor array of 75×75 μm^2 IDEs, with electrode width and spacing of 300 nm, on the surface of the chip. Although the surface was flat enough for IDE fabrication, the contact pads to the embedded circuitry were recessed from the surface by approximately 2 μm. Since the thickness of the electron beam resist is less than 2 μm, it would be impossible to fabricate the contact pads

at the same time. For a typical liftoff process, the resist layer needs to be 2-3 times thicker than the desired metal thickness in order to ensure a disconnect between the metal within the lithography template and that on the surface of the resist. In order to make contact to the recessed pads, additional contact pads were added to the chip with photolithography as shown in Figure 6.5(a).

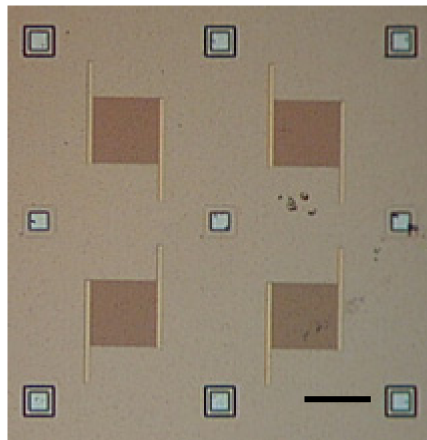

Figure 6.4 Interdigitated electrodes with area of $75 \times 75\ \mu m^2$ fabricated on the surface of the readout chip. Scale bar indicates 75 μm.

Another method for fabricating contact pads from the IDEs to the readout chip contact pads is to use focused ion beam (FIB) induced deposition. This is done by scanning the ion beam in a pattern where the contact pad is desired. A nozzle is position near the surface of the substrate that ejects a gas containing the desired deposition material. For this application, platinum was used. The platinum gas is absorbed on the surface of the sample. When the ion beam is scanned over the area, the platinum gas is broken down in volatile and non-volatile components leaving only a layer of platinum on

the substrate. We connect four chemiresistors by platinum contacts as shown in Figure 6.5(b).

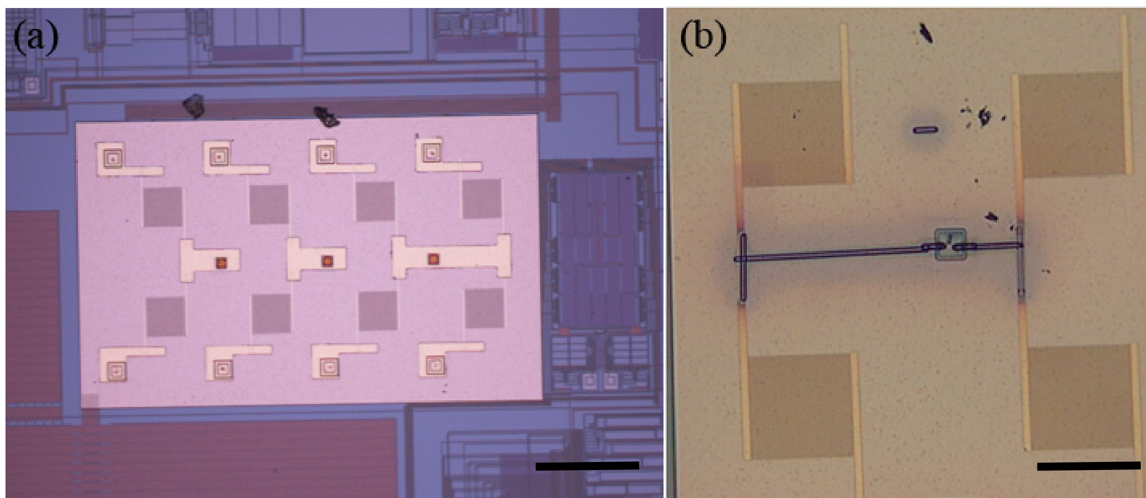

Figure 6.5 (a) Eight sensor array on the readout with contact pads added by photolithography. Scale bar indicated 200 μm. (b) 4 sensor on another array with contact pads added by focused ion beam platinum deposition. Scale bar indicated 75 μm.

Once the IDEs and contact pads were fabricated, we deposited the MPN films with a microdispensing system. The IDEs were spaced by 200 μm; therefore, it would be possible to coat each sensor with a unique MPN film. Since it has been determine that thicker films lead to lower noise properties[7], we swept the coffee stain pattern across the surface of the IDEs to ensure that the majority of the MPNs were on the active region of the IDEs. Using this technique, we coated the array with both 1-octanethiol (C8) and 1-mercapto-6-phenoxyhexane (OPH). The coated array is shown in Figure 6.6. The top row was coated with a C8 film while the bottom row is coated with an OPH film.

Figure 6.6 Sensor array coated with micro-dispensing system. Top row of sensor are coated with C8 while bottom row is coated with OPH. The scale bar indicates 75 µm.

Once the array was fabricated, the chip was returned to our collaborators at MSU for testing. To determine whether the array was functional, it was sent for vapor testing in the Zellers lab where it was exposed to 2-butanone, nitromethane and toluene. The chip was tested in a vapor chamber and was exposed to the analytes at different concentrations for two minute intervals. A C8 sensor's response, after baseline resistance cancellation, to three concentrations of toluene is shown in Figure 6.7. The sensor was found to have a reversible vapor response that increased with increasing vapor concentration.

The array was exposed to 2-butanone, nitromethane and toluene to test the linearity of response. Figure 6.8 shows the vapor calibration curves for a C8 coated sensor to the three vapors along with the linear fits. The R^2 values for 2-butanone, nitromethane and toluene were found to be 0.993, 0.996, and 0.993 respectively indicating that the vapor responses are linear with concentration.

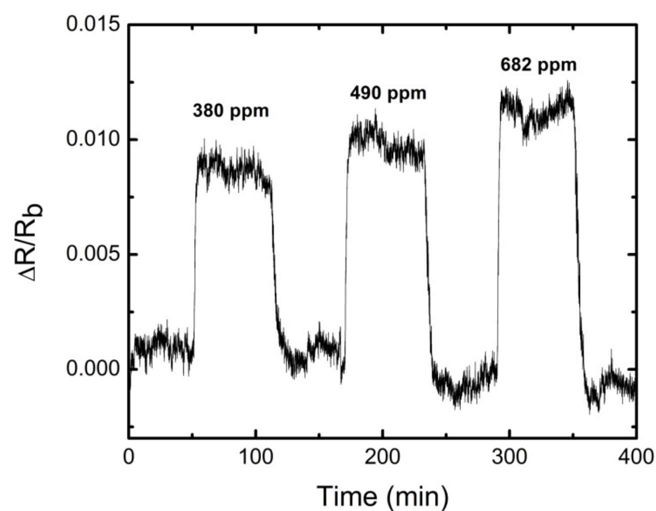

Figure 6.7 Response curves of a C8 coated sensor to toluene at 380, 490, and 682 ppm after baseline resistance cancellation.

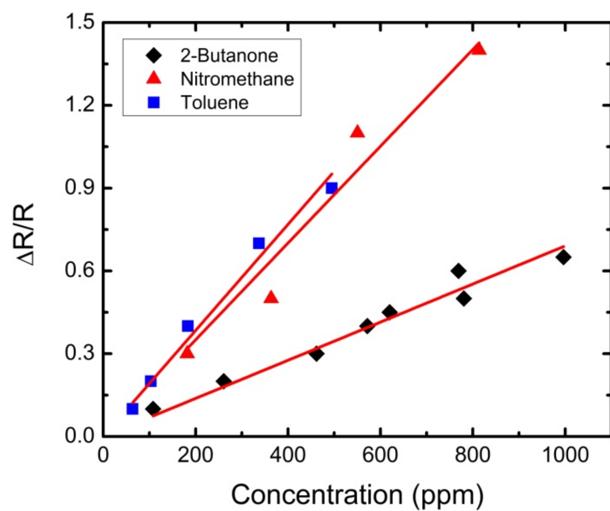

Figure 6.8 Concentrations curves of a C8 coated sensor to 2-butanone, nitromethane, and toluene.

6.3 Microfluidic Packaging

In the previous section, the monolithic sensor array was vapor tested using a test chamber. While this can be used to assess the functionality of the sensor array, the ultimate goal is to interface the sensor system with a μGC system. This involves enclosing the sensor array in a low volume chamber. A method for enclosing a sensor chip with a microfluidic package was developed by our collaborators, led by Dr. Wen Li, at MSU[2]. This is done to improve sensor performance by reducing external influences, such as turbulent air flow, and provide a protective barrier for the array. It will also shield the array to exposure of additional and unwanted chemical species during vapor testing as well as improve the probability of the target analytes reaching the sensor array.

Enclosing the sensor array is a not a trivial task due to the MPN film layer. Because the films must be deposited before packaging, the packing process must not involve the use of solvents that could rinse away the MPN film. The packaging materials must also be made of a nonabsorbent material to prevent an interaction with the vapor mixture. The package must include an inlet and outlet for the capillary tubing that interconnects with the GC column as well as a recessed head space above the sensor array that allows for the flow of the vapor mixture. The entire fabrication must also be completed at low or room temperature to prevent degradation of the MPN film.

Another challenge of packing the system is the small size of the sensor chip. To create a stable platform for the sensor chip and input/output capillary tubes, they mounted the readout chip into an extension carrier. A silicon piece was etched with a recess to accommodate the sensor ship and inlet/outlet capillary tubes. A schematic of the

extension carrier is shown in Figure 1.9. To enclose the sensor array with a low volume chamber, a glass lid was etched with a channel to allow the flow of the vapors through the system. All of the components were sealed with a nonabsorbent epoxy.

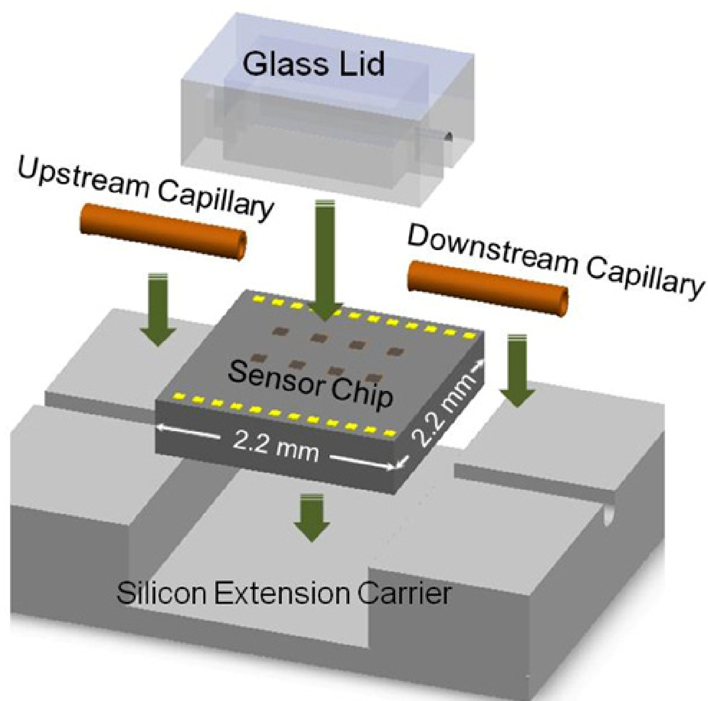

Figure 6.9 Schematic view of total device assembly designed Dr. Wen Li's research group.

The chip is assembled by first gluing the sensor chip into the extension carrier with the sensor array in line with the etched trenches for the inlet and outlet capillaries. The extension carrier is then secured into a header and the sensor chip is wirebonded. The capillary tubes are then inserted, and epoxy is applied around their perimeter to prevent leaks. Once the epoxy has cured, a layer of epoxy is but on the glass lid and it is placed

over the chip. An example a complete package is shown in Figure 6.10. Helium was passed through the system for leak testing, and additional epoxy was applied as needed.

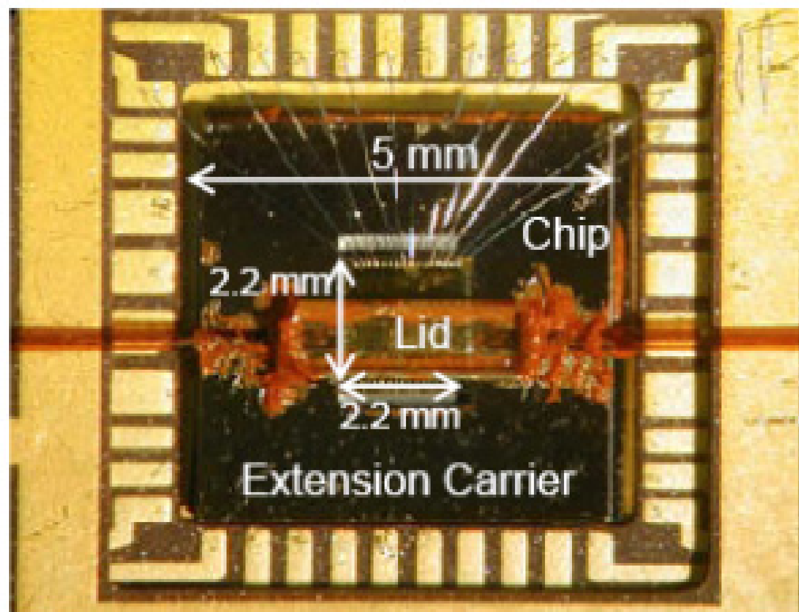

Figure 6.10 Assembled packaged sensor chip wirebonded to a 40-pin DIP header. The capillary tubing and glass lid are attached with a nonabsorbent epoxy.

To verify that the assembly did not compromise the integrity of the sensor array, the array was exposed to a vapor mixture of acetone, ethanol, n-heptane, and toluene. Samples of these vapors were injected via a gas sampling loop through the capillary column of a bench-scale GC (Agilent 7890A) at a flow rate of 1.2 mL/min. The voltage of the chemiresistors was monitored and recorded on a laptop computer. The results for a single sensor are shown in Figure 6.11. Five exposures were recorded and were found to be reproducible.

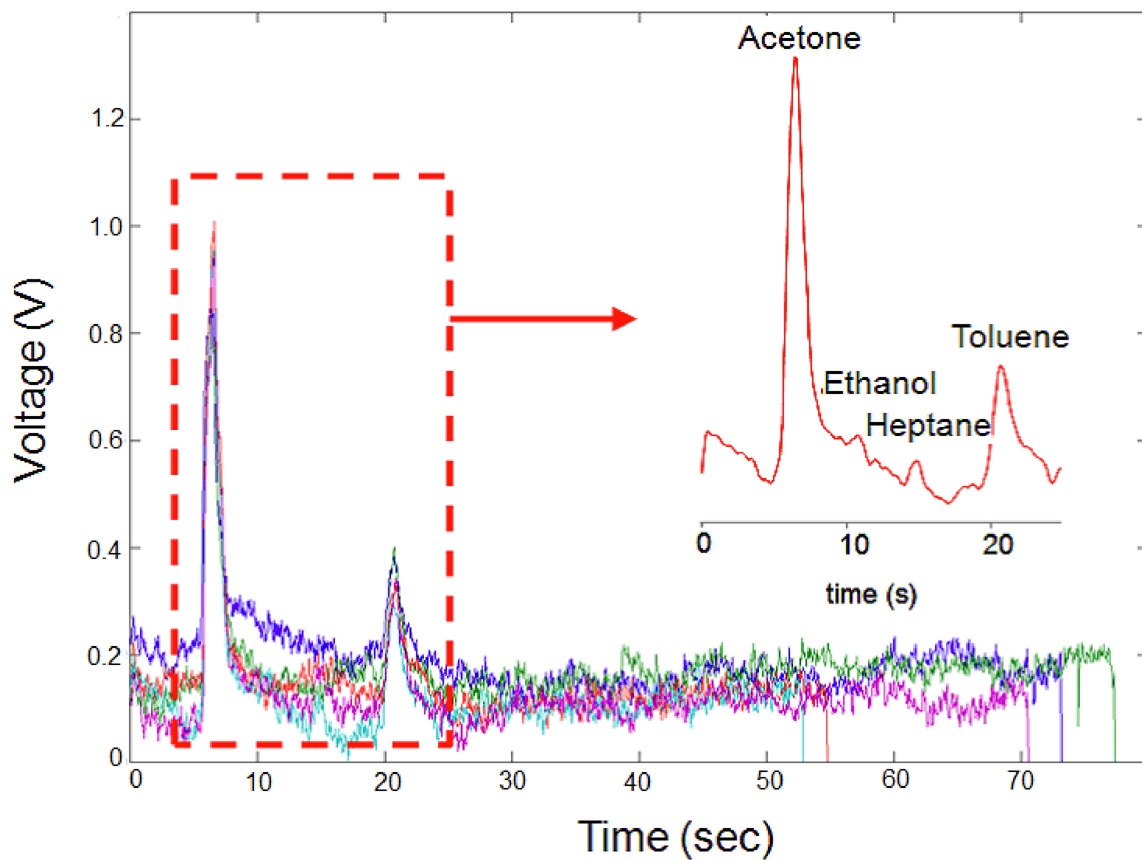

Figure 6.11 Five chromatograms from a single chemiresistors on the packaged sensor chip. As shown in the inset, the components of the vapor mixture are distinguishable.

6.4 Conclusions

An integrated sensor system was created where the sensor array was fabricated on the surface of the readout chip. In early attempts of creating a monolithic system, the roughness of the chip's surface impeded the fabrication of the IDEs on the surface of the chip. To alleviate this problem, a metal plateau was fabricated directly under the surface of the sensor region to ensure a planar surface. Exposure to a high energy electron beam was also found to damage transistors within the readout chips electronics. Annealing was found to reduce but not completely reverse shifts in the threshold voltage. The current

generation of readout chips was fabricated with the readout circuitry isolated from the sensor fabrication area in order to reduce the exposure of the electronics to the high energy electron beam.

By separating the readout electronics from the sensor fabrication area and ensuring that the sensor fabrication area is planar, a monolithic sensor system on a $2.2 \times 2.2\ mm^2$ chip can was fabricated. We successfully fabricated an eight sensor array on the surface of the readout chip. We coated the array with two types of MPN films using a microdispensing system. Vapor testing performed by our collaborators showed the sensor array to have reversible response to 2-butanone, nitromethane and toluene vapors that scaled linearly with concentration.

6.5 References

1. X. Mu, E. Covington, D. Rairigh, Ç. Kurdak, E. T. Zellers and A. Mason, submitted (2011).
2. N. Ward, X. Mu, G. Serrano, E. Covington, Ç. Kurdak, E. T. Zellers, A. Mason and W. Li, submitted (2011).
3. D. Rairigh, A. Mason, M. P. Rowe and E. T. Zellers, Proc. of the IEEE International Symposium on Circuits and Systems, 2002-2005, (2008).
4. D. J. Rairigh, G. A. Warnell, C. Xu, E. T. Zellers and A. J. Mason, IEEE Trans. Biomed. Circuits Syst. **3** (5), 267-276 (2009).
5. K. J. Wang, F. C. Tseng, W. L. Chen, G. R. Shen, W. W. Wang and K. Lee, Proc. of the IEEE International Conference on Electron Devices and Solid-State Circuits, 293-295 (2007).
6. F. Campabadal, S. Ghatnekar-Nilsson, G. Rius, E. Figueras and J. Esteve, Proc. of Spanish Conference on Electron Devices, 213-216, (2005).
7. E. L. Covington, R. W. Turner, C. Kurdak, M. P. Rowe, X. Chao and E. T. Zellers, Proc. of the IEEE Sensors Conference, 102-105 (2008).

Chapter 7

Future Work for Sensor Optimization

7.1 Introduction

For the fabrication of a μGC system, all components of the system will need to be scaled down. Chemiresistors can be easily miniaturized, and techniques to do so using electron beam lithography and electron beam induced crosslinking were presented in Chapter 3. However, making the smallest array possible is not always beneficial. We claim that for a given μGC system, there is an optimal sensor size. Optimizing the sensor size to the μGC system should also improve the limit of detection. While the noise properties of chemiresistors scale inversely with sensor area[1, 2], the minimum detectable amount of analyte is be proportional to the area; therefore, there is a tradeoff in improving the limit of detection with respect to the sensor's size. Sensor optimization also includes tailoring its properties for a given μGC system. The radius of the GC column, size of the sensor chamber, and properties of the detected analyte must also be considered when designing the sensor array.

A schematic of a sensor within a chamber is shown in Figure 7.1. In order to create a model for optimizing the size of the sensors, the components of the μGC system have been greatly simplified. A chemiresistor of width L_1 and length L_2 is shown in a

chamber with height h. The capillary inlet has a radius of r. The IDEs are covered with a nanoparticle film of thickness t. All of the parameters shown can vary greatly from system to system. The inlet and outlet capillaries come in a variety of diameters. The dimensions of the IDEs can be tailored to any dimensions through photo- or electron beam lithography. Using the micro-fluidic packaging process presented in Chapter 6, even the chamber height can be chosen. If a μGC system has already been designed with a given capillary radius and chamber height, then the sensor array can designed to optimize the limit of detection.

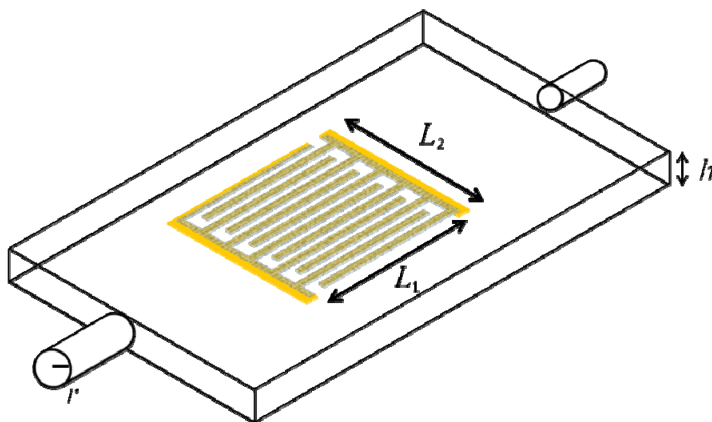

Figure 7.1 A schematic of a sensor array with width and length of L_1 and L_2 enclosed in a chamber of height h. The inlet capillary tube has radius r.

We determined a simple expression for tailoring the sensor size for a given GC configuration. We also fabricated a test sensor array with a variable chamber volume are also shown. Vapor testing has not verified the postulated optimal sensor size, but the framework for future experiments is outlined. Optimizing sensor size will be critical in improving the limit of detection of target analytes.

7.2 Optimizing Sensor Size

Since chemiresistors are concentration dependent sensors, the amount of analyte absorbed into the nanoparticle film is dependent on the partition coefficient of the analyte, K, which is ratio of the concentrations of the analyte in the sorbent, C_s, to the concentration in air, C_a.

$$K = {}^{C_s}\!/\!{}_{C_a} \tag{7.1}$$

Vapor response is dependent on the partition coefficient of the analyte, and their relationship is detailed by Steinecker, *et al.*[3].

For a thin MPN film, the baseline resistance, R, of the films is dependent on the electrode spacing, S, film resistivity, ρ, number of electrodes, n, overlap length of adjacent electrodes, L, and film thickness, t.

$$R = \rho S / (2n - 1)Lt \tag{7.2}$$

Equation 7.2 shows that a thicker MPN film will lead to a lower resistance. A more accurate calculation of film resistance was shown in Equation 1.12. This was also shown in Chapter 2, where thicker nanoparticle films were found to have lower resistance and a lower noise prefactor than thinner films. For optimal performance, the film should be sufficiently thick to cover the IDEs. Because the electric field, as shown in Chapter 1, decreases substantially past the electrode height, there is no benefit to having a film much thicker than the electrode height. An MPN that is too thick will only hurt the sensor response by impeding analyte integration into the film and slowing the response time.

The sensor's response is proportional to the partition coefficient which is also proportional to the volume in the chamber above the sensor. As shown in Equation 7.1, the concentration of an analyte in the sensor chamber will be C_a, which is the ratio of the amount of analyte, N_a, over the chamber volume, V_a.

$$K = C_s/C_a = {(N_s/V_s)}\big/{(N_a/V_a)} \tag{7.3}$$

The sensor chamber volume should be chosen with respect to the partition coefficient of the analyte. While the width and length of the chamber will be defined by the area of the sensors, the height can be easily controlled by fabricating a lid with an etched recess. This height, h, should be chosen to be proportional to the partition coefficient and the thickness of the MPN film.

$$h \approx Kt \tag{7.4}$$

If the height is too large, the chances of the analyte reaching the sensor will be decreased. If the height is too small, magnitude of the response will be compromised due to the sensor depleting the analyte in the headspace and altering the vapor concentration.

As a vapor passes through a GC column, the compounds spread and the concentration takes the form of

$$C(z) = C_0 e^{-z_2/2\lambda_0^2} \tag{7.5}$$

where C_0 is the initial concentration and λ_0 is the spatial extend of the vapor in the column. The volume at the outlet of the column, of radius r, will be $\pi r^2 \lambda_0$. Ideally, this volume will match the volume of the area above the sensor array, hL_1L_2, where L_1 and L_2

are the length and width of the sensor. Combining this with Equation 7.4, the optimal sensor area can be found.

$$L_1 L_2 = \pi r^2 \lambda / h = \pi r^2 \lambda / Kt \quad (7.6)$$

If the volume above the sensor does not match the vapor output of the column, then λ will scale as

$$\lambda = (\pi r^2 / awh) \lambda_0 \quad (7.7)$$

where w is the width of the sensor chamber. For a given r, w, and h, there is an optimal sensor length. By integrating the concentration profile over the length of the sensor array, the optimal size can be determined using Equation 7.8.

$$\langle C \rangle = \frac{1}{L} \int_{-L/2}^{L/2} C_0 e^{-z_2/2\lambda^2} dz \quad (7.8)$$

Figure 7.2 shows the normalized concentration over the sensor array with various r values. For larger values of r, going to smaller sensor size does not improve performance because the concentration does not vary greatly with sensor size. When the size of the column radius decreases, the effect on sensor size becomes more pronounced; therefore, it is important to scale down both the column radius and sensor length accordingly.

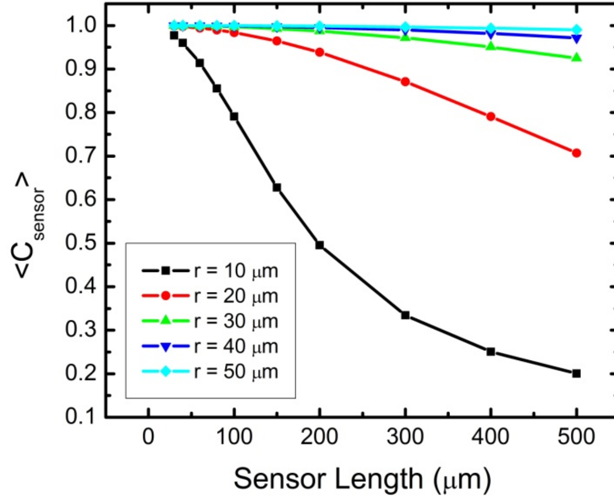

Figure 7.2 The normalized concentration, C_{sens}, for different GC columns of radius, r. As r is decreased, the need for smaller sensor arrays becomes more pronounced. This was calculated for a sensor chamber with a 600 μm width and 50 μm height.

Previous studies have shown that the intrinsic noise of the sensor arrays scales inversely with sensor area[4, 5]; therefore, to minimize the noise, the area of the sensor and the film thickness should be maximized. Since the limit of detection is proportional to the noise, the minimum concentration, C_{min}, detectable by the sensor will therefore scale as

$$C_{min} = 1/\sqrt{V_{sensor}} = 1/\sqrt{tL_1L_2} \tag{7.9}$$

The total amount of analyte, N_{min}, which can be detected by the sensor is therefore

$$N_{min} = C_{min}\pi r^2\lambda = \pi r^2\lambda/\sqrt{tL_1L_2}. \tag{7.10}$$

Substituting the denominator for Equation 7.6 gives

$$N_{min} = KtL_1L_2/\sqrt{tL_1L_2} = K\sqrt{tL_1L_2}. \tag{7.11}$$

The amount of analyte that a sensor can detect is proportional to the volume of the sensor as shown in Equation 7.11.

7.2.2 Fabrication of a Test Sensor Array

To verify the model for optimizing the sensor size, a scaling study on sensor performance versus sensor size must be performed. To do so, the optimum sensor size for a given μGC system must be calculated. A sensor array will be fabricated for integration into the μGC system that includes sensors of both the calculated optimal area and a wide range of other sizes. Vapor testing will be performed, and the performance of each sensor will be compared to determine the model's validity.

The properties of chemiresistors can be easily modified by changing either the electron beam lithography template or MPN film properties. In order to determine the best sensor configuration for a given GC column, we fabricated a multi-sensor array. Sensors ranging from 30×30 μm^2 to 500×500 μm^2 were fabricated on one chip so they could be simultaneously tested. The test chips were fabricated at the wafer level to include features for easy integration into a GC system. First, large metal contact pads were fabricated so that the IDEs could be easily connected to a carrier chip by either wire bonding or soldering. Grooves were etched into the surface for inlet and outlet capillary tubes for vapor testing. Glass lids were etched with recess of various sizes to control the sensor chamber height. The fabrication process for the glass lids and sensor chip are outline in Appendix C and D, respectively. A complete sensor chip is shown in Figure 7.3. The capillary tubes were glued into the chip as well as the glass lid with a 100 μm

etched region above the sensor array. An optical image of the sensor array, with sensors ranging in length from 30 μm to 500 μm, is also shown.

After the glass lid and capillary tubes had been glued to the sensor chip, the sensor's resistance became immeasurably high; therefore, they were unable to be tested. This could be due to the glue incorporating into the film and causing the films to be nonconductive. In future chips, the properties of the sensors will be checked throughout the integration process to determine the cause of failure.

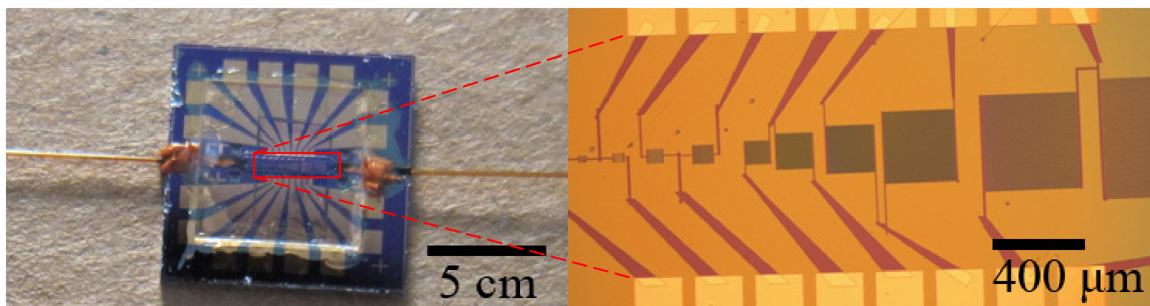

Figure 7.3 Chip with glass lid with a 100 μm etched recess above the sensor array and inlet and outlet capillary tubes. The red box indicates the area of the sensor area show to the right.

When a successful sensor package is complete, it will be interfaced with a GC system for vapor testing. Vapor sensitivities for different sized sensors will be compared. The calculated optimal sensor size will be compared to experimental results to verify the optimization model. Note that using this system, GC columns of different inner radii can be tested. The sensor chamber volume can also be easily changed by fabricating lids etched to different depths.

7.3 Conclusions

The miniaturization of the components of a μGC system will not be hindered by the fabrication of the chemiresistor array. Fabrication of micro-scale chemiresistor arrays can be easily done through electron beam lithography. In order to pattern an array of chemiresistors with different MPN films, a technique using electron beam induced crosslinking was presented. Using this technique, we fabricated a chemiresistor array with an area of less than 600 μm^2 making it the smallest chemiresistor array reported to date.

However, fabricating the smallest array possible should not be the goal for chemiresistors arrays intended for integration into a μGC system. The sensing performance of a μGC system may not be improved by such small sensors and may even be hindered by their small size. To improve the limit of detection of a μGC system, the sensor array must be designed with respect to the GC column radius, chamber height, and partition coefficient of the target analyte. While the noise properties are improved by increasing the size of the sensor, the amount of detectable analyte is increased by decreasing sensor size. Therefore, the optimal size of sensor must be calculated for a given μGC system. For large GC column, the effect of sensor size on performance is minimal. As the radius of the column decreases, the effect of the size of the sensor becomes more pronounced. The optimal sensor area was found to be proportional to the column radius and spatial extend of the analyte in the column and inversely proportional to the sensor array's chamber height.

In addition to optimizing the size of the sensor, improving the long term stability of the sensors must also be achieved. While sensors were shown to maintain sensitivity to toluene over several weeks at elevated temperatures, their drift in baseline resistance continues to plague their long term stability. If this drift is truly caused by the loss of the nanoparticle's ligand coating, then various synthesis techniques, such as the use of a tri-thiol bond, may need to be employed to ensure the integrity of the ligand coating.

7.4 References

1. M. G. Ancona, A. W. Snow, E. E. Foos, W. Kruppa and R. Bass, IEEE Sens. J. **6** (6), 1403-1414 (2006).
2. C. Kurdak, J. Kim, A. Kuo, J. J. Lucido, L. A. Farina, X. Bai, M. P. Rowe and A. J. Matzger, Appl. Phys. Lett. **86** (7), 073506 (2005).
3. W. H. Steinecker, M. P. Rowe and E. T. Zellers, Anal. Chem. **79** (13), 4977-4986 (2007).
4. W. Kruppa, M. G. Ancona, R. W. Rendell, A. W. Snow, E. E. Foos and R. Bass, Appl. Phys. Lett. **88** (5) (2006).
5. E. L. Covington, R. W. Turner, C. Kurdak, M. P. Rowe, X. Chao and E. T. Zellers, Proc. of the IEEE Sensors Conference, 102-105 (2008).

Appendix A

Electron Beam Lithography Sample Preparation

1. Rinse the sample with acetone then 2-propanol (IPA).
2. Inspect under microscope to determine if the surface is clean.
    a. Repeat step one if needed. Sonicate the sample in desired solvent to remove stubborn contaminants from the surface.
    b. Oxygen plasma etching can also be used to clean the surface if needed.
3. Dry with nitrogen gun
4. Bake the sample for 5 minutes on 150°C hotplate to remove any residual solvent from the surface.
5. (Optional) Spin HDMS for 30s at 4000 rpm. This step may be omitted for small samples, because it may cause non-uniformity in the photoresist
6. Spin MicroChem PMMA 950 K
    a. Use A2 PMMA for 700 Å resist thickness.
    b. Use A4 PMMA for 2000 Å resist thickness.

7. Bake in an oven for 30 minutes at 170°C.

8. Store in a sample holder. Make sure to keep the sample holder level during transportation to keep the surface of the samples clean.

9. Perform electron beam lithography.

10. Develop for 30 seconds using a 1:3 mixture of methyl isobutyl ketone (MIBK) and IPA.

    a. Developer should be prepared in advance and be at room temperature for best results.

11. Rinse in IPA for one minute.

12. Dry with nitrogen gun.

13. Inspect under microscope.

Appendix B

Photolithography Sample Preparation for Chemiresistor Contact Pads

1. Rinse the sample with acetone then 2-propanol (IPA).
2. Inspect under microscope to determine if the surface is clean.
   a. Repeat step one if needed. Sonicate the sample in desired solvent to remove stubborn contaminants from the surface.
   b. Oxygen plasma etching can also be used to clean the surface if needed.
3. Dry with nitrogen gun
4. Bake the sample for 5 minutes on 150°C hotplate to remove any residual solvent from the surface.
5. (Optional) Spin HDMS for 30s at 4000 rpm. This step may be omitted for small samples, because it may cause non-uniformity in the photoresist
6. Spin Microposit S1813 photoresist
   a. See manufacturer's data sheet for spin curves to select desired film thickness.
7. Bake for 60 seconds on a 115°C hotplate.

8. Desired exposure is 150 mJ/cm^2.

    a. For the MJB tools, this will be approximately 5 seconds, although I've consistently used 7 will good results.

9. Develop for one minute in MF-319.

10. Rinse in IPA for one minute.

11. Inspect under microscope.

12. If needed, continue to develop in 10 second increments until desired level of development is achieved.

13. Oxygen plasma etch before metal evaporation to remove residual photoresist from the pattern.

Appendix C

Process for Etching Glass Lids

1. Acquire 500 μm thick Pyrex wafers.
2. Piranha clean the wafers before processing.
3. Pretreat the wafers with a 5 minute dip in buffered oxide etch (BHF) to reduce the undercut in the HF etching step.
    a. Rinse in deionized (DI) water
    b. Spin/Rinse/Dry (SRD)
4. Evaporate Cr/Au 300Å/2000Å
5. Photolithography Instructions
    a. Drybake: 15 min @110°C in oven
    b. Spin: 9260 @ 1k
    c. Sit for 10 min for stabilization
    d. Softbake: 30min @90°C in oven
    e. Exposure: 85s on MA6

f. Develop: AZ400k/DI_water (1:3); 3min

g. Rinse in DI-water, SRD

h. Hard bake: 15min @110°C in oven

i. Inspect under microscope

6. Etch the Cr/Au layer to expose the Pyrex wafer for etching.

   a. Au etch: 65sec (etch rate: 3000 Å/min)

   b. Rinse in DI water

   c. Cr etch: 15sec (etch rate: 2500 Å/min)

   d. Rinse in DI-water, SRD

7. Etch recess in the Pyrex wafer.

   a. HF: 4min

   b. Rinse in DI water, SRD

   c. Inspect under microscope and measure with Dektak.

8. Strip the photoresist.

   a. Hot PRS2000 15 min

   b. Rinse in DI water and SRD.

   c. Inspect under microscope.

9. Remove Au/Cr.

    a. Au etch: 65sec (etch rate: 3000 Å/min)

    b. Rinse in DI water

    c. Cr etch: 20sec (etch rate: 2500 Å/min)

    d. Rinse in DI water and SRD.

10. Dice the Pyrex wafer

    a. Pretreat the surface with photoresist to protect during the dicing process.

Appendix D

Process for Etching Capillary Inlet/Outlet Grooves

1. Wafers should already be patterned with the metal contact pads.
2. Clean the wafers with acetone and IPA.
3. Dry the wafers for 15 min at 110°C in oven
4. Spin Microposit S1813 photoresist at 4000 rpm.
5. Softbake: the resist for 1 minute at 110°C on a hotplate.
6. Expose for 6 seconds on MA6 using the desired mask.
7. Develop with MF 319 for one minute.
8. Rinse in DI water and spin-rinse-dry (SRD).
9. Inspect the pattern.
10. Hardbake for 30min at 110°C in an oven.
11. Remove the oxide on the wafer in the inlet/outlet region.
    a. Immerse in buffered oxide etch (BHF) for 23 minutes and 10 seconds.
    b. Rinse in DI water and SRD.

c. Inspect with Nanospec to ensure removal.

12. Remove photoresist with Hot PRS2000 for 15 minutes.

    a. Rinse in DI water and SRD.

    b. Inspect under microscope.

13. Drybake the wafers for 15 minutes at 110°C in an oven.

14. Spin AZ 9260 at 1500 rpm.

    a. Sit for 10 min for stabilization.

    b. Softbake for 2.5minutes at 110°C on a hotplate.

15. Exposure with the inlet/outlet mask for 55s on MA6.

16. Develop with AZ400k/DI water (1:3) for 3minutes.

    a. Rinse in DI-water and SRD.

    b. Inspect under microscope.

17. Before etching, mount the wafers on carrier wafers.

    a. Spin carrier wafers: 1827 at 3000 rpm

    b. Clean the edge with wipe paper.

    c. Mount process wafers with the flat aligned.

    d. Hardbake for 20 minutes at 110°C in an oven.

18. Etch the inlet and outlet grooves.
    a. Desired depth is 380 µm.
    b. STS Etch with Fluidic recipe (~5 µm /min).
    c. Etch time 1 hour and 22 minutes.
    d. Use Zygo to measure the depth.
19. Separate the wafers with hot PRS2000
20. Rinse in DI water and SRD.
21. Dice the wafers.
    a. Protect the surface of the wafer with photoresist for dicing.
    b. After dicing, remove resist with acetone and IPA.
    c. Rinse with DI water.